1-1-2014

Measuring Brain Iron In Healthy Controls And Accessing Venous Abnormalities In Parkinson's Disease Using Mri

Manju Liu
Wayne State University,

MEASURING BRAIN IRON IN HEALTHY CONTROLS AND ASSESSING VENOUS ABNORMALITIES IN PARKINSON'S DISEASE USING MRI

by

MANJU LIU

DISSERTATION

Submitted to the Graduate School

of Wayne State University,

Detroit, Michigan

in partial fulfillment of the requirements

for the degree of

DOCTOR OF PHILOSOPHY

2014

MAJOR: BIOMEDICAL ENGINEERING

Approved by:

_____

Advisor Date

_____

_____

_____

_____

DEDICATION

This dissertation is dedicated to my parents:

Jianwu Liu

Guizhi Xi

ACKNOWLEDGMENTS

I would like to thank three important groups of people, without whom this dissertation would not have been possible: my committee, my wonderful lab-mates, and my family.

First of all, I would like to express my sincere thanks and deepest appreciation to my supervisor, Dr. E. Mark Haacke for his enduring inspiration, patient, guidance, support and encouragement all through my study in the past six years. I'm so blessed to have a supervisor who is one of the most important scientists in this field and also cares about his students. I cannot thank him enough for what he has done for me.

I would like to thank the members of my dissertation committee - not only for their time and extreme patience but also for all the valuable comments and suggestions that they provided for me during my research. To Dr. Jaladhar Neelavalli, I thank for the wonderful MRI courses he offered. He is always there available to answer questions. I learned a great deal from his courses and enjoyed them all. Thanks to Dr. Weiping Ren for his clearly explaining physiology during the courses. His expertise on physiology helped my understanding about the iron metabolism in human brain. Thanks to Dr. Zhifeng Kou, his support, attention to detail, hard work, and scholarship have set an example I hope to match someday. To Dr. Indrin Chetty, I thank for all his advice, also for his flexibility in scheduling, gentle encouragement and relaxed demeanor made for a good working relationship and the impetus for me to finish.

To my lab-mates, thanks for the fun and support. To Dr. Weili Zheng, Yongquan Ye, Saifeng Liu, Yanwei Miao, Wei Feng and Charbel Habib, for their supports and guidance to my projects. Whenever I encountered problems, they are always the right people to consult to bring new ideas. I also want to thank many others in the lab, Rachel Martis Laze, Jing Jiang, Yi Zhong, Ying

Wang, Sagar Buch, Jin Tang, Meng Li, Yang Xuan, Norman Cheng, Ching-Yi Hsieh, Emil Eugen Pacurar, Yimin Shen, Jessy Mouannes-Srour, Jiani Hu, Judith Farah, Lisa Brownschidle, Paul Kokeny, Tilak Gattu, Pavan Jella, Uday Krishnamurthy, Zahid Latif, and Yashwanth Katkuri for their support and friendship.

Finally, the most important, I want to thank my parents, Jianwu Liu and Guizhi Xi, my husband, Ning Wen, my mother-in-law, Yuanqin Huang, my uncle, Jianju Liu and my lovely children, Jacob Wen and Anna Wen. Thank you all for your constant support and endless love through the ups and downs of my academic career. It has been bumpy at times, but your confidence in me has enhanced my ability to get through it all and succeed in the end.

TABLE OF CONTENTS

LIST OF TABLES

LIST OF FIGURES

ABBREVIATION LIST

3D CE MRAV: 3D time-resolved contrast-enhanced arteriovenography

ADHD: Attention Deficit Hyperactivity Disorder

BBB: Blood-Brain Barrier

CN: Caudate Nucleus

CSF: CerebroSpinal Fluid

DSI: Direct Saturation Imaging

EJV: External Jugular Veins

EMF: electromotive force

F_d/F_{sd}: the ratio between the dominant and sub-dominant IJVs

FDRI: Field Dependent Relaxation Rate Increase

FOV: Field of View

FQ: Flow Quantification

FQ: Flow Quantification

F_{sd}/TA: normalized sub-dominant IJV flow

GE: General Electric

GM: Gray Matter

GP: Globus Pallidus

GRE: Gradient Recalled Echo

HP: High Pass

ICPMS: Inductively Coupled Plasma Mass Spectrometry

IJV: Internal Jugular Vein

IPD: Idiopathic Parkinson's Disease

LfR/Lf: Lactoferrin Receptor / Lactoferrin

LIJV/tA: normalized left IJV flow

MFC: Magnetic Field Correlation

MFC: Magnetic Field Correlation

MinIP: Minimum Intensity Projection

MIP: Maximum Intensity Projection

MRA: MR Angiography

MRA: MR Angiography

MRI: Magnetic Resonance Imaging

MS: Multiple Sclerosis

MTf/sMTf: GPI-anchored Melanotransferrin / soluble Melanotransferrin

PC: Phase Contrast

PT: Pulvinar Thalamus

PTA: Percutaneous Transluminal Angioplasty

PUT: Putamen

PVH: PeriVentricular Hyperintensities

QSM: Quantitative Susceptibility Mapping

RF: radio frequency

RI: low iron content region

RII: high iron content region

RN: Red Nucleus

ROC: Receiver Operator Characteristic

ROI: Regions Of Interest

SD: Standard Deviations

SN: Substantia Nigra

SPIN: Signal Processing in NMR

SPU: Siemens Phase Unit

SSS: Superior Sagittal Sinus

SWI: Susceptibility Weighted Imaging

T: Tesla

T1: Spin Lattice Relaxation Time

T2: Spin-Spin Relaxation Time

tA: total Arterial flow

TE: Echo Time

Tf/TfR: Transferrin / Transferrin Receptor

THA: Thalamus

tIJV/tA: normalized total IJV flow

TOF: Time of Flight

TR: Repetition Time

UKPDSBB: United Kingdom PD Society Brain Bank Criteria

Venc: Velocity Encoding

WM: White Matter

WMH: White Matter Hyper Intensity

XRF: X-Ray Fluorescence

Chapter One Introduction

1.1 Background and Project Motivation

Iron has long been recognized to play a key role in brain functions such as oxygen transport, neurotransmitter synthesis, electron transfer, and myelin production [1, 2]. Despite the positive implications, when in a free ferrous form, iron is known to be toxic and can lead to free radical production. There has been a growing interest in studying the role of iron in neurodegenerative diseases such as multiple sclerosis, Parkinson's disease, Alzheimer's disease and other conditions including aging [1-6]. In healthy people, iron deposition in gray matter and white matter structures evolves both temporally and spatially. It has been documented that iron content in different brain gray-matter nuclei accumulates at different rates at different ages [7, 8]. It is important to have the knowledge of quantitative characterization of brain iron change during brain development and aging. This will allow us to gain more insights into the potential abnormalities such as iron over-accumulation or iron deficit that involve in the pathophysiologic process of various neurodegenerative diseases. Evaluating brain iron changes in normal brains *in vivo* provides a reference for monitoring iron changes in patients both cross-sectionally and longitudinally.

In the last few years, there has been an increasing interest in the role of veins in neurodegenerative diseases, [9, 10]. More attention has been paid to the extracranial veins such as the internal jugular veins (IJVs) and the azygous veins as being potential sources of venous hypertension especially in multiple sclerosis (MS) [11, 12]. The obstructed veins are thought to cause venous insufficiency. The use of MR angiography (MRA) and flow quantification (FQ) for the study of the vasculature in patients with Parkinson's disease is a novel concept spurred, in part, by our recent work in MS patients [13].

Idiopathic Parkinson's disease (IPD) is the second most common neurodegenerative disease and the etiology of IPD remains unknown [14]. There are two interesting parallels between IPD and MS to consider: both show reduced perfusion [15, 16], and both have regions of high iron content in the basal ganglia [17, 18]. The parallels between the two diseases, the suggestion that venous insufficiency causes damage to the vessel wall and leads to local extravasation of the blood and subsequent increases in local iron content, and the presence of cerebrovascular disease in roughly 39% of patients with IPD [19] led us to realize the importance to study the venous vascular characters of IPD patients. This will have the potential to open new doors in studying the vascular etiology of IPD.

Moreover, it has been shown that there is an increased presence of white matter hyper intensity (WMH) in IPD patients [20]. The suggested causes for these deficits include ischemia and venous insufficiency from periventricular venular collagenosis [21-23]. One group found that the severity of WMH at baseline was the best predictor of PD progression [24]. This also motivates us to study the correlation between WMH and venous abnormalities in IPD.

1.2 Project Aims:

In this dissertation, phase and quantitative susceptibility mapping (QSM) will be used for measuring iron deposition in normal brain grey matter GM) nuclei to review the age effects, and the correlation between susceptibility and *in vivo* iron concentration will be studied.

The head and neck major veins' anatomy and blood flow in Parkinson's patients will be studied and compared with normal controls. White matter hyper intensity volume will be quantified for Parkinson's patients and compared with normal subjects.

Therefore, the specific aims and hypotheses of this thesis are:

Specific Aim 1: To establish the baseline of putative iron content in the basal ganglia, mid-brain and the thalamus as a function of age in healthy human brains using phase and ΔR2* on the basis of susceptibility weighted imaging (SWI).

Hypothesis 1a: Phase and ΔR2* in the brain grey matter nuclei increase as a function of age.

Hypothesis 1b: The size of the high iron deposition region increases as a function of age in the brain grey matter nuclei.

Specific Aim 2: To establish the baseline of iron deposition in the basal ganglia, mid-brain and the thalamus as a function of age in healthy human brains using QSM derived from SWI phase, and find the conversion factor between magnetic susceptibility and *in vivo* iron concentration.

Hypothesis 2a: Magnetic susceptibility in the grey matter nuclei increases as a function of age.

Hypothesis 2b: Linear correlation exists between susceptibility and *in vivo* iron deposition.

Specific Aim 3: To investigate the presence of structural and flow abnormalities in the dural sinuses and extracranial draining veins in IPD patients and study the correlation between venous abnormalities with WMH volume.

Hypothesis 3a: There is a higher prevalence of abnormal venous anatomy and flow on the left side of the brain and neck in IPD patients.

Hypothesis 3b: WMH volume in patients with IPD is higher than in normal controls.

Hypothesis 3c: Venous abnormalities correlate with WMH volume.

Chapter Two Basic concepts of gradient echo imaging, phase, and quantitative susceptibility mapping

Chapter overview

Gradient echo imaging (GRE) is one of the most important MRI sequence types. Rapidly collecting high resolution MR imaging with low radio frequency (rf) power deposition becomes possible with gradient echo-based MR imaging techniques [25]. In MRI, phase represents the spatial magnetic field variations, and the magnetic susceptibility maps can be extracted from phase image. Both the phase and magnetic susceptibility can be used for measuring iron owing to iron's paramagnetic character.

In this chapter, we will briefly introduce the basic aspects of gradient echo imaging that are relevant to susceptibility weighted imaging (SWI). We will also touch on the principles of susceptibility, phase and how to do quantitative susceptibility mapping from SWI phase images.

2.1 Gradient echo imaging

Larmor Frequency:

When placing a particle in a magnetic field, if the nuclear spin of that particle is not zero (in multiples of ±1/2), the spin will precess around the external magnetic field axis. The precession frequency is the Larmor frequency, which is defined as (we assume a right handed system) [25]

$$\vec{\omega} = -\gamma \cdot \vec{B} \tag{2.1}$$

where ω is the precession angular frequency, γ is the gyromagnetic ratio of the element, and $\vec{B}$ is the actual field experienced by that particle.

Proton (hydrogen ^{1}H) is the key element in the human body that produces nuclear magnetic resonance signals owing to its non-zero net spin (1/2) and large biological abundance (around 63% of the body weight [26]). Each type of element has its own gyromagnetic ratio. The gyromagnetic ratio of the proton is 2.675×10^8 rad/s/T.

Magnetization Vector:

For a spin isochromat (a given small enough volume (V) whose external field is constant, so the spins in V experience the same phase) with a large number of protons, by summing up all the magnetic monument vectors and dividing by V, we get the magnetization vector (magnetic moment per volume) [27]. The sum of the magnetization vectors is called net magnetization ($\vec{M}$). ;

When not taking the proton interactions into account, the Bloch equation is:

$$\frac{d\vec{M}}{dt} = \gamma\vec{M} \times B_0\hat{z} \tag{2.2}$$

where B_0 is the strength of the applied magnetic field along z direction (longitudinal).

The magnetization can be decomposed into the longitudinal and transverse components:

$$\frac{dM_z}{dt} = 0 \tag{2.3}$$

$$\frac{d\vec{M}_\perp}{dt} = \gamma\vec{M}_\perp \times B_0\hat{z} \tag{2.4}$$

Once the magnetization has a transverse component, it will rotate about B_0, and this can be detected. An electromotive force (emf) is created in coil through with the spin's magnetic flux sweeps, a consequence of Faraday's law. The time-dependent form of this current carries the information that is eventually transformed into an image of the sample [27].

T1 Process:

In the external magnetic field, when doing nothing, the net magnetization (M_0) lies along the same direction as the main field. So the longitudinal magnetization M_z is equal to M_0 and the transverse magnetization M_{xy} is zero. After tipping the original net magnetization away from the main magnetic field by using a radio frequency (rf) pulse, the longitudinal magnetization (M_z) will gradually recover to the beginning state. The time which is used to describe this type of longitudinal magnetization recovery is called the spin lattice relaxation time (T1), which can be determined experimentally [27].

When taking the spin-lattice interaction into account, equation (2.3) becomes:

$$\frac{dM_z}{dt} = \frac{1}{T1}\,(M_0 - M_z) \tag{2.5}$$

By solving the differential equation (2.5), after the application of an rf pulse, the longitudinal magnetization can be calculated by:

$$M_z(t) = M_z(0)e^{-t/T1} + M_0(1 - e^{-t/T1}) \tag{2.6}$$

T2 process:

As mentioned in the "Larmor Frequency' section, the transverse magnetization (M_{xy}) rotates about the main magnetic field z at the Larmor frequency. Due to the interactions between the protons with their environment, spins at different locations may experience a slightly different magnetic field which is the combinations of the main field and the local field [27]. This leads those isochromats to rotate at different rates. As a result, the transverse magnetization starts to dephase and the phase difference increases as time goes. Since the net magnetization is the vector sum of each individual magnetization, during the dephasing process the transverse magnetization decreases. The time constant which is used to describe the transverse dephasing property (returning to transverse magnetization equilibrium, $M_{xy} = 0$) is called the spin-spin relaxation time (T2).

Therefore, the transverse component of the Bloch equation (2.4) should add another term for T2 decay:

$$\frac{d\vec{M}_{\perp}}{dt} = \gamma \vec{M}_{\perp} \times B_0 \hat{z} - \frac{1}{T2}\vec{M}_{\perp} \tag{2.7}$$

The solution for this differential equation is:

$$\vec{M}_{\perp}(t) = \vec{M}_{\perp}(0)e^{-t/T2} \tag{2.8}$$

Both of the T1 and T2 processes occur at the same time. T2 is always less than or equal to T1.

There are basically two sources leading to the transverse magnetization decay. One is from the molecular interactions which is described by T2, and the other is from the variations in B_0, which

is described by T2'. The combined time constant is T2*. The relation between those time constants is:

$$\frac{1}{T2^*} = \frac{1}{T2} + \frac{1}{T2'} \tag{2.9}$$

The inversion of the relaxation times (T2, T2', T2*) are call relaxation rates (R2=1/T2, R2'=1/T2', R2*=1/T2*). So,

$$R2^* = R2 + R2' \tag{2.10}$$

The rule of thumb is that the magnetization loss due to T2' can be recovered in Spin Echo sequence but not in Gradient Recalled Echo sequence (GRE), while the magnetization loss due to T2 can't be recovered no matter what sequence is applied.

Fourier transform MRI:

With the neglect of relaxation effects and demodulating frequency of ω_0, the MRI signal is

$$s(t) = \iiint dx\, dy\, dz\, \rho(x, y, z,) e^{i\phi_G(x,y,z,t)} \tag{2.11}$$

where $\rho(x, y, z)$ is the effective spin density, $\phi_G(x, y, z, t)$ is the accumulated phase determined by the three orthogonal linear gradient fields $G_x(t)$, $G_y(t)$, and $G_z(t)$.

$$\phi(\vec{r}, t) = -\gamma \cdot \Delta B(\vec{r}) \cdot t = -\gamma \cdot G(\vec{r}, t)\vec{r} \cdot t \tag{2.12}$$

$$\phi_G(x, y, z, t) = -\gamma[\int_0^t dt' G_x(t')x + \int_0^t dt' G_y(t')y + \int_0^t dt' G_z(t')z] \tag{2.13}$$

with $= \gamma/2\pi$, we define

$$k_x(t) = \gamma \int_0^t dt' G_x(t'), \quad k_y(t) = \gamma \int_0^t dt' G_y(t'), \quad k_z(t) = \gamma \int_0^t dt' G_z(t') \tag{2.14}$$

Equation (2.11) becomes

$$s(k_x, k_y, k_z) = \iiint dx\, dy\, dz\, \rho(x, y, z) e^{-2\pi i(k_x x + k_y y + k_z z)} \tag{2.15}$$

Therefore, by nature, the MRI signal is the Fourier transform of the effective spin density. The MRI data are collected in k-space. Each k-space point is a complex number collected with real and imaginary channels. Then by preforming the inverse Fourier transform to the complex k-space, the effective spin density distribution and phase can be reconstructed.

GRE sequence diagram:

After applying the excitation rf pulse, the transverse magnetization starts to dephase. There are basically two ways to refocus the spins where an echo is formed. One way is to employ a π-pulse, which is called spin echo; and the other way is to apply a dephasing gradient followed by a rephasing gradient with the same amplitude and duration, which is called gradient echo.

Gradient echo imaging is one of the most important and frequently used sequences in modern MRI. With the GRE technique, it becomes possible to collect MRI data rapidly with high spatial resolution and low rf power deposition [25].

Figure 2.1 shows a typically 3D single-echo GRE sequence diagram. The corresponding k-space trajectory for an example slice is shown in Figure 2.2. The data are being sampled (filling the k-space) when the ADC is on.

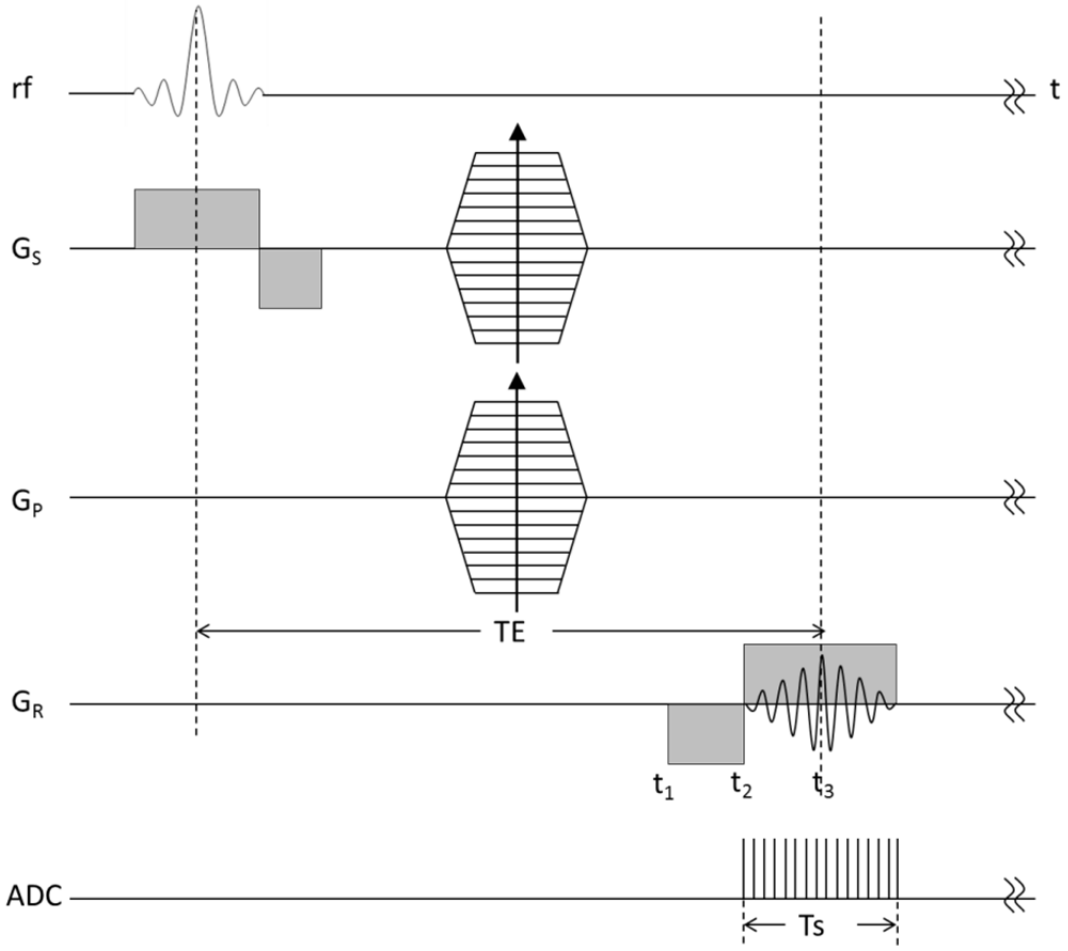

Figure 2.1: 3D GRE pulse sequence diagram. rf = radio frequency, G_s= slab select gradient, G_p= phase encoding gradient, G_R= readout gradient, ADC = analog to digital converter, TE = echo time, T_s=sampling time. $t_2 - t_1 = t_3 - t_2 = T_s/2$.

In Figure 2.2, assuming the maximum amplitude of the phase encoding gradient G_p is $G_{p,max}$, the increment of G_p between two continuous TRs is ΔG_p, the duration of each G_p is τ_p, at $t = t_2$, according to Eq. (2.14), k_y and k_x of the first data point collected in k-space is

$$k_y = -\gamma G_{p,max} \cdot \tau_p = -k_{y,max} \tag{2.16}$$

$$k_x = -\gamma G_R \cdot (t_2 - t_1) = -k_{x,max} \tag{2.17}$$

k_x of other data points during T_s is

$$k_x(t) = -\gamma G_R \cdot (t_2 - t_1) + \gamma G_R \cdot (t - t_2) \quad t \geq t_2 \tag{2.18}$$

At $t = t_3$, we have $t_2 - t_1 = t_3 - t_2 = T_s/2$, so according to Eq. (2.18) $k_x(t_3) = 0$, where a gradient echo is formed. The time duration from the rf excitation to t_3 is defined as echo time (TE). The time duration between two successive rf pulses is called repetition time (TR). In the example case shown in Figure 2.1, one k-space line is filled in each TR. During T_s, N_x points are sampled symmetrically about $k_x = 0$. By varying G_p and G_s, the whole 3D k-space will be filled.

Steady-state incoherent gradient echo imaging:

The sequence introduced in Figure 2.1 is a simplified GRE sequence. Practically, prior to the application of the next rf pulse, the transverse magnetization left from the previous excitation should be handled. We will consider only the spoiled gradient echo sequence in which the remnant transverse magnetization is dephased at the end of each excitation cycle. This approach leads to a lack of coherence in the transverse magnetization, and the longitudinal component is the only coherence for the next excitation [28]. There are several methods to achieve spoiling, such as by using variable high amplitude gradients (gradient spoiling), and/or by shifting the rf pulse phase (usually the rotation angle is set to 117°) from one excitation to the next (rf spoiling) [25].

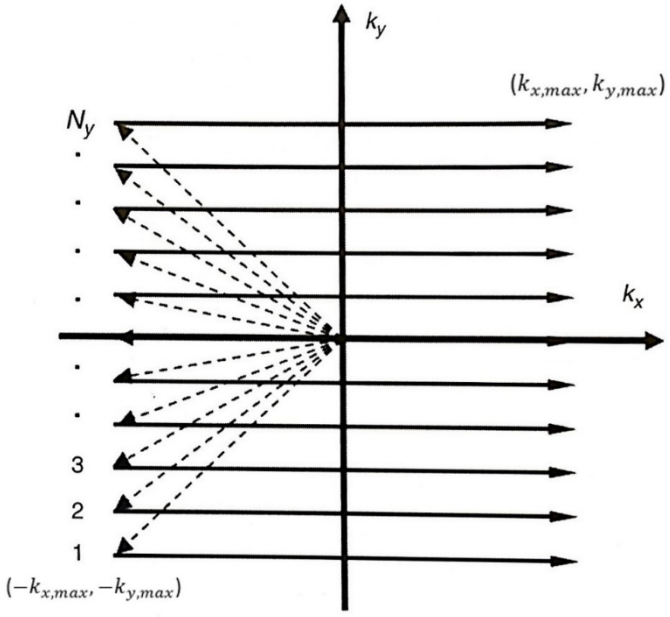

Figure 2.2: The corresponding k-space filling mechanism for a simple GRE sequence as shown in Figure 2.1.

Magnetization equilibrium can be reached by repeating the application of rf pulses. For steady-state incoherent gradient echo imaging, the voxel signal can be written as [27]:

$$\hat{\rho}(\theta, TE, TR) = \rho_0 \sin(\theta) \frac{1 - E_1}{1 - \cos(\theta) E_1} E_2 \qquad (2.19)$$

where ρ_0 is the spin density of a given voxel, $E_1 = e^{-TR/T1}$, and $E_2 = e^{-TE/T2*}$.

Sequence diagram of Susceptibility Weighted Imaging (SWI):

SWI is a type of 3D steady-state incoherent gradient echo imaging. Besides that, in order to reduce the phase effect from blood flow, flow compensation gradients in the three encoding directions are applied [25]. The single echo SWI sequence diagram is shown in Figure 2.3.

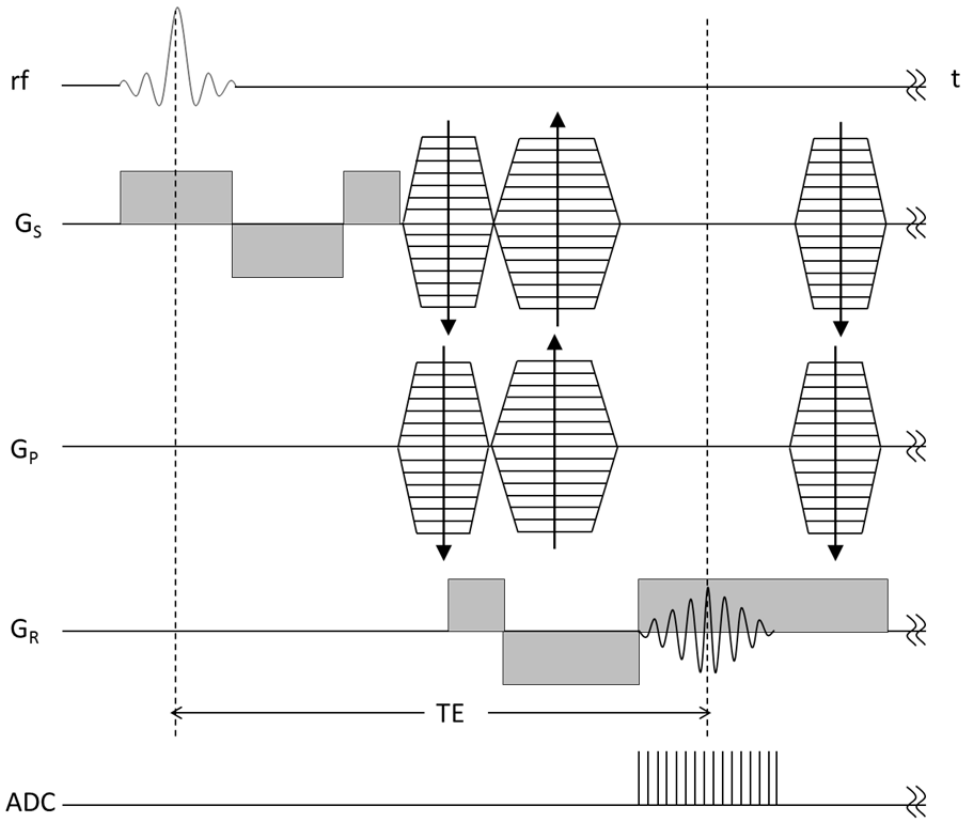

Figure 2.3: Single echo SWI sequence diagram. Flow compensation is in all three directions. G_s = slab selection/partition encoding gradient, G_p = phase encoding gradient, G_R = readout gradient.

2.2 Magnetic Susceptibility and Phase

Magnetic field and its perturbation due to substances inside the field

When an external magnetic field passes through a substance, different substances will show different macroscopic behaviors. Basically, the substance will get magnetized and the field inside and outside will be perturbed. Magnetic susceptibility (χ) is the tissue property which describes how the material is magnetized when exposed under a magnetic field and how the magnetic field is changed by the material. Based on the induced magnetization, materials are categorized into diamagnetic, paramagnetic and ferromagnetic materials [29]. The magnetic moment of a diamagnetic material aligns anti-parallel to the main magnetic field (negative χ); the magnetic moment of a paramagnetic material aligns parallel to the main field (positive χ); and ferromagnetic material creates its own magnetic field even without an external field (positive constant magnetization $\overrightarrow{M}$) [29].

Since the human body is mainly made of water by weight, susceptibility of water is used as a reference which is approximately -9 parts per million (ppm) relative to vacuum. In this thesis, when we say something being 'diamagnetic' or 'paramagnetic' actually means being more diamagnetic or more paramagnetic than water. Iron is strongly paramagnetic, as a result it can be easily detected with MRI.

A uniform magnetic field can be defined by

$$\vec{B}_0 = \mu_0 \vec{H} \tag{2.20}$$

When an object is placed in this external uniform field, the magnetic field inside the material will become

$$\vec{B} = \mu_0 \left(\vec{H} + \vec{M} \right) \tag{2.21}$$

where $\vec{B}$ is the magnetic field in Tesla, $\vec{H}$ is called magnetic field strength in Ampere/meter (A/m), $\vec{M}$ is the magnetization either permanent or induced, $\vec{M}$ and $\vec{H}$ have the same unit, and μ_0 is the absolute permeability of the free space ($4\pi \times 10^7$ Tm/A).

The induced magnetization $\vec{M}$ relates to $\vec{H}$ by the magnetic susceptibility χ:

$$\vec{M} = \chi \vec{H} \tag{2.22}$$

So by combing Eq. (2.21) and Eq. (2.22), the magnetic field inside the substance can be written as ($\chi \ll 1$):

$$\vec{B} = \mu_0(1+\chi)\vec{H} \quad \text{or} \quad \vec{B} = \left(\frac{1+\chi}{\chi}\right)\mu_0\vec{M} \approx \mu_0\vec{M}/\chi \tag{2.23}$$

The magnetic field outside the substance will also be perturbed due to the induced magnetization. The solution of the perturbed field depends on the induced magnetization and the shape and volume of the object [25].

The magnetic field inside and outside a uniform sphere and an infinitely long cylinder has been derived analytically, which are shown in Table 2.1 [25].

Table 2.1: Expressions for field inside and outside a uniform sphere and an infinitely long cylinder [25]

	Internal Field	**External Field**
Sphere	B_0	$B_0 + \frac{\chi B_0}{3} \cdot \frac{a^3}{\lvert\vec{r}\rvert^3} \cdot (3\,cos^2\,\theta - 1)$
Cylinder	$B_0 + \frac{\chi B_0}{6} \cdot (3\,cos^2\,\theta - 1)$	$B_0 + \frac{\chi B_0}{2} \cdot \frac{a^2}{\lvert\vec{r}\rvert^2} \cdot \sin^2\theta\, cos2\phi$

In this table, B_0 is the external uniform magnetic field applied along the z-direction. θ is the angle between the position vector $\vec{r}$ and the main magnetic field for the sphere case, or between the long axis of the cylinder and the main field for the cylinder case. ϕ is the polar angle substanded by $\vec{r}$ on the plan perpendicular to the long axis of the cylinder. $\vec{r}$ is the position vector. a is the radius of the sphere or the cylinder.

Phase

In MRI, phase is used to encode the special information. In the rotating frame, no phase accumulation is seen. Phase from the encoding gradients is removed during signal modulation. Thus, phase value at a given point in an MR image is sensitive to the local magnetic field perturbation ($\Delta B(\vec{r})$) relative to the main field [25]:

$$\varphi(\vec{r}) = \Delta\omega(\vec{r}) \cdot TE = -\gamma \cdot \Delta B(\vec{r}) \cdot TE \tag{2.24}$$

where TE is the echo time where the signal is acquired.

The phase image contains all the field information, macroscopic and microscopic. The macroscopic fields come from the geometry of the big objects such as brain, air-tissue interface around the sinus in the brain, and inhomogeneities in the main magnetic field. The microscopic

fields are the ones we are usually interested in, the local susceptibility distribution [30]. Phase can be summarized as:

$$\varphi = -\gamma \cdot \left(\Delta B_{main\ field} + \Delta B_{cs} + \Delta B_{global\ geometry} + \Delta B_{local\ susceptibility}\right) \cdot TE \quad (2.25)$$

where ΔB_{cs} represents the field variance due to chemical shift, which is different from the local susceptibility effect. The local magnetic field variance generated from susceptibility difference also depends on the geometry of the object, however, the chemical shift effect only depends on the material type [31].

Phase aliasing

Phase images are reconstructed from the complex signals acquired through the real and imaginary channels. The complex signal can be written as:

$$S = S_{Real} + i\, S_{im} = |S| \cdot cos\varphi \cdot \hat{x} + |S| \cdot sin\varphi \cdot \hat{y} \quad (2.26)$$

which can also be written as:

$$S = |S| \cdot e^{i\varphi(\vec{r},t)} \quad (2.27)$$

where $|S| = \sqrt{S_{Real}^2 + S_{im}^2}$ is the magnitude and $\varphi(\vec{r}, t) = \tan^{-1}(\frac{S_{im}}{S_{Real}})$ is the phase (as shown in Figure 2.4).

However, as shown in Figure 2.4, phase values can only be correctly returned if they are between $-\pi$ to π. If the phase value lies outside this interval, it will be wrapped back. For example, a phase of $-450°$ will wrap back to $-90°$ This process is called phase aliasing. The true phase can be described as:

$$\phi_{ture}(\vec{r}) = \phi_{measured}(\vec{r}) + 2\pi \cdot n(\vec{r}) \tag{2.28}$$

where $n(\vec{r})$ are integers. In order to obtain the actual information about $\Delta B(\vec{r})$, $n(\vec{r})$ needs to be determined to unwrap the measured phase.

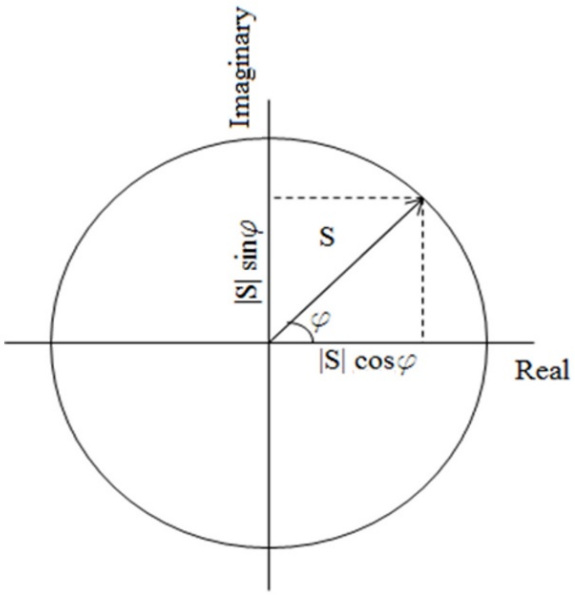

Figure 2.4: Complex representation of a signal vector S in the Real-Imaginary plane. |S| represents the magnitude and φ is the phase.

Homodyne High Pass filter

According to Eq. (2.25), since our interest for iron quantification is the field change due to tissue susceptibility, other terms relating to the global field inhomogeneity should be removed. Due to the fact that the background field is relatively low spatial frequency in nature, it can be removed by applying a high-pass filter. Homodyne high pass filter is a robust and efficient method for background removal, which is widely used in SWI [32].

When doing the homodyne high-pass filtering, low-pass filtered k-space data is created first by applying a Hanning window to the central part of the k-space, and then reconstructing this low special frequency k-space data to the image domain ($\hat{\rho}_{\mathrm{lp}}$). And then the original complex data ($\hat{\rho}$) is divided by the low-pass filtered data to generate the complex high-pass filtered image ($\hat{\rho}_{\mathrm{hp}}$). The pipeline of the homodyne high pass filter processing is shown in Figure 2.5 [29]. The high pass filtered phase image is generated by:

$$\phi_{hp} = arg\left(\hat{\rho}_{hp}\right) = arg(\hat{\rho}/\hat{\rho}_{lp}) \tag{2.29}$$

where the division is pixel-wised operation.

The advantages of homodyne high pass filter include that no phase unwrapping is needed; it's a very quick process, only about 10 seconds are need for processing a data set of 512×512×64; it's robust; it provides good contrast and high SNR. However, the homodyne high pass filter also causes phase signal loss, especially for structures with relatively large sizes such as the globus pallidus, putamen, thalamus and so forth. This will lead to an underestimation of the tissue susceptibility which will further lead to errors for iron prediction [29].

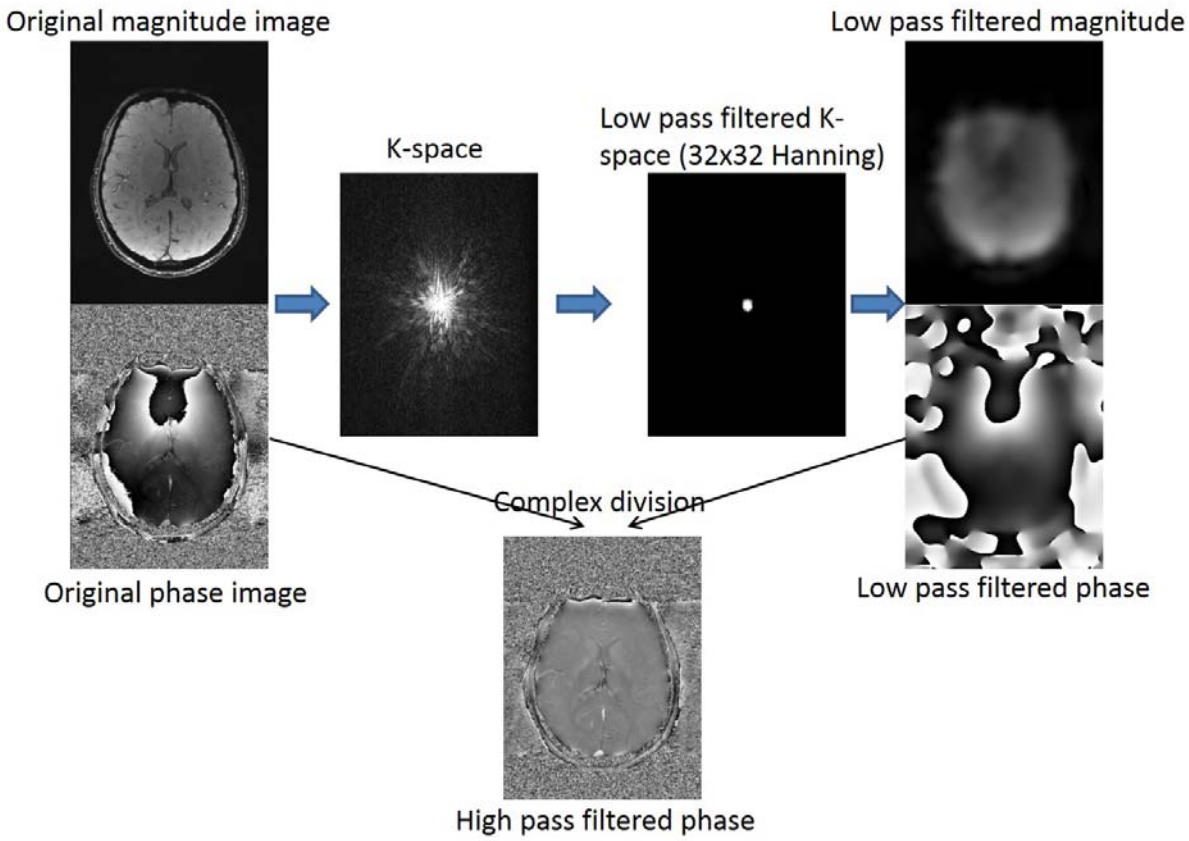

Figure 2.5: The illustration of the step flow to do homodyne high pass filter [29].

QSM reconstruction

Induced magnetization $\vec{M}$ creates dipolar field around it. The z-component of the field variation can be written as [29]:

$$\Delta B_z(\bar{r}) = \frac{\mu_0}{4\pi}\int_{v'} d^3\bar{r}' \left\{\frac{3M_z(\bar{r}') \cdot (\bar{z}-\bar{z}')^2}{|\bar{r}-\bar{r}'|^5} - \frac{M_z(\bar{r}')}{|\bar{r}-\bar{r}'|^3}\right\} \tag{2.30}$$

which can be written as a convolution [29, 33]:

$$\Delta B_z(\vec{r}) = \mu_0 M_z(\vec{r}) * G(\vec{r}) \tag{2.31}$$

where $G(\vec{r})$ is the 3D Green's function:

$$G(\vec{r}) = \frac{1}{4\pi} \cdot \frac{3cos^2\theta - 1}{r^3} \tag{2.32}$$

From Eq. (2.23) and (2.31), the following equation can be generated which is used to predict the induced magnetic field distribution from the magnetic susceptibility distribution:

$$\Delta B_z(\vec{r}) = \mu_0 M_z(\vec{r}) * G(\vec{r}) \approx B_0 \chi(\vec{r}) * G(\vec{r}) \tag{2.33}$$

The convolution can be expressed in the Fourier domain, and the field variations will become:

$$\Delta B_z(\vec{r}) = B_0 \cdot FT^{-1}\{FT[\chi(\vec{r})] \cdot FT[G(\vec{r})]\} \tag{2.34}$$

The Fourier transform of the Green's function is:

$$G(\vec{k}) = FT[G(\vec{r})] = \begin{cases} \frac{1}{3} - \frac{k_z^2}{k_x^2 + k_y^2 + k_z^2}, & when\ \vec{k} \neq 0 \\ 0, & when\ \vec{k} = 0 \end{cases} \tag{2.35}$$

Calculating the induced magnetic field distribution by the combination of Eq. (2.33), (2.34) and (2.35) is call "Forward Calculation".

Since $\Delta B_z(\vec{r})$ information can be extracted from phase images ($\varphi(\vec{r})$), $\chi(\vec{r})$ can be calculated from the inverse calculation (rearrange Eq. 2.34):

$$\chi(\vec{r}) = \frac{FT^{-1}[G^{-1}(\vec{k}) \cdot \varphi(\vec{k})]}{\gamma \cdot B_0 \cdot TE} \tag{2.36}$$

Figure 2.6 shows the general steps of creating QSM maps.

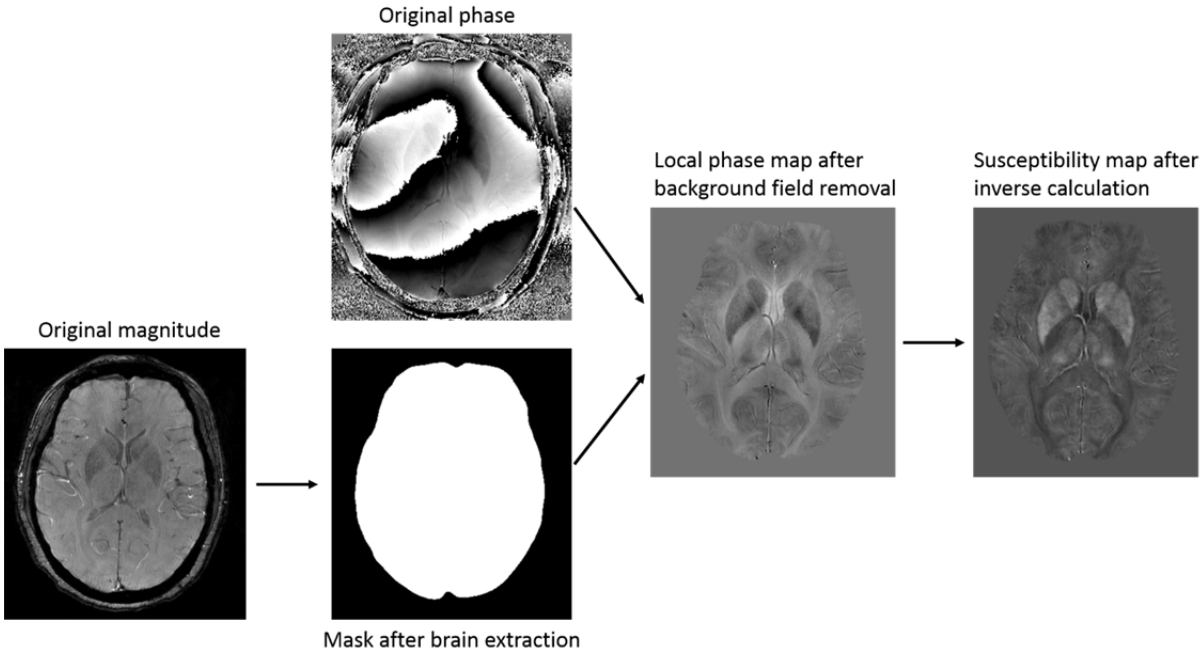

Figure 2.6: Image processing procedures to generate susceptibility maps [29]. Phase unwrapping is not necessary for all the algorithms before background field removal. For example, when homodyne high pass filter is used to remove the background field, phase images don't need to be unwrapped before applying the filter. Phase unwrapping can be done with or without brain binary mask images, but with the masks, the processing speed can be improved.

As we can see in Eq. (2.36), $G^{-1}(\vec{k})$ goes to infinity when $G(\vec{k})$ is equal or close to zero, which leads to an ill-posed problem. This happens at the points on or near two conical surfaces in k-space at the magic angles of $54.7°$ and $125.3°$ from the B_0 direction [34]. This problem causes streaking artifact and high noise levels in QSM. This poor reconstruction behavior could be solved through either truncated k-space division [35, 36] or other optimization methods [29, 34, 37].

In this chapter, we have introduced the basic aspects of gradient echo imaging that relevant to susceptibility imaging, principles of phase imaging, phase image post processing and the link between the magnetic susceptibility and phase information. Iron is the most abundant and a

crucial metal element in human body [38]. It is a strong paramagnetic material. The presence of iron can influence the magnitude and phase signals. As a result, iron can be visualized and measured by MRI techniques. In the next chapter, we will review iron quantification methods.

Chapter Three Brain iron and iron quantification

Iron is the most abundant metal element within the brain [38]. People are becoming more interested in understanding the roles of iron in brain normal functions and its association with neurodegenerative diseases. It has been known that iron is involved in a variety of processes which are vital for letting our brain function normally such as gene expression, neuronal development, enzymatic reactions, dopamine, heme, iron-sulfur cluster synthesis, electron transport and so forth [39]. Also, normal aging and the potential pathophysiology of many neurological disorders are thought to have correlation with excessive iron accumulation or iron deficiency [38]. For example, the iron elevation in the brain has been investigated extensively to understand its link to neurodegenerative diseases including Alzheimer's disease [40], Parkinson's disease [41], multiple sclerosis [18] and so forth. Iron deficiency has been reported to be associated with developmental delays [42], attention deficit hyperactivity disorder (ADHD) [43], restless legs syndrome [44] and neurodegeneration [45].

Approximately, 3 to 5 grams of iron is stored in healthy people [46]. There are basically two categories of iron in the human body: heme iron which is in hemoglobin (two thirds of the total iron) and non-heme iron (one third) [8]. Transferrin, ferritin and hemosiderin are three important types of non-heme iron proteins. The function of transferrin is to carry iron from the blood to the whole body and brain tissues. It can bind two iron atoms and its molecular weight is 79.6 kg/mol. Ferritin is a soluble protein which stores excess iron atoms to maintain the homeostatic levels of iron. Ferritin has a large spherical protein coat. There can be up to 4500 iron atoms in a 24-unit ferritin molecule and the molecular weight is 474 kg/mol. Another form of iron storage protein is hemosiderin, which is water insoluble and is considered coming from denatured ferritin and

other material. It can be found in white blood cells and studies reported that relatively large amount of hemosiderin is present in diseased brains [47].

3.1 Basic brain iron physiology

Normal Iron transport in human brain

Due to the presence of brain endothelium (blood-brain barrier or BBB), iron metabolism in the brain is separated from other parts of the body. Although the mechanism of how iron crosses BBB has not been completely understood, several pathways have been suggested. Those pathways include transferrin / transferrin receptor (Tf/TfR), lactoferrin receptor / lactoferrin (LfR/Lf) and GPI-anchored melanotransferrin / soluble melanotransferrin (MTf/sMTf) pathways [48]. A pathway for the transport of non-transferrin-bound iron across the BBB cells also exists [49]. Another suggestion is that ferroportin 1 (FP1)/hephaestin (Hp) and/or hephaestin-independent (FP1/CP) iron export systems might also plays roles in Fe^{2+} transport across abluminal membrane of the BBB [48, 50].

Iron induced oxidative stress

Excessive iron deposition can be neurotoxic due to the possibility of generating induced free radicals which contribute to the oxidative reactions [51]. Brain cells consume oxygen to catabolize carbon- and hydrogen-rich molecules into energy. During this process, hydrogen peroxide (H_2O_2) is formed. Hydrogen peroxide can go across cell membranes freely. When hydrogen peroxide reacts with ferrous (Fe^{2+}), the famous Fenton reaction happens (Fenton, 1893). The ferric (Fe^{3+}) iron and highly reactive hydroxyl radicals are formed [51].

$$Fe^{2+} + H_2O_2 \rightarrow Fe^{3+} + HO^- + \cdot OH$$

These free radicals (· HO) will interact with polyunsaturated fatty acid (RH) and take an electron from RH to produce another type of free radicals (R ·).

$$RH + \cdot HO \rightarrow R \cdot + H_2O$$

The organic free radicals (R ·) may also react with oxygen to form organic oxygen radicals ($RO_2 \cdot$)

$$R \cdot + O_2 \rightarrow RO_2 \cdot$$

Then the oxygen radical will steal an electron from another lipid (RH) (it can be another biological molecule) to form an organic hydroperoxide (ROOH) and another free radical (R ·), so the vicious cycle continues to damage the brain cells.

$$RO_2 \cdot + RH \rightarrow ROOH + R \cdot$$

The damage chain is lipid peroxidation which can destroy lipids. In brain, the cell membranes of neurons and many supporting cells are rich in polyunsaturated fatty acids, so they are easily damaged by lipid peroxidation and can even lead to cell death [51].

Due to the high correlation of certain diseases with the problematic iron regulation, researchers have been motivated to find robust and efficient methods to quantify iron *in vivo*, which will provide better understanding of the normal iron behaviors and prognosis of disease related to iron deficiency and overload.

3.2 MRI methods for Iron quantification

Since iron in the form of ferritin is strongly paramagnetic and there is sufficient amount of iron in the human brain, MRI signals (both magnitude and phase) can be related to iron concentrations. Using MRI, we can image iron in the form of ferritin, hemosiderin and deoxyhomoglobin. Moreover, tissue intrinsic parameters such as R2, R2*, magnetic susceptibility can be extracted from MR images for iron quantification. The motivation for quantifying iron is different for deoxhyhemoglobin, ferritin and hemosiderin. If we can quantify the levels of deoxyhemoglobin in veins, then we can estimate the oxygen saturation [35]. This is important in studying stroke, diseases with reduced perfusion such as multiple sclerosis (MS), and cerebral vascular reserve. Quantifying ferritin may play a role in diseases such as Parkinson's disease, Huntington's disease and a number of other diseases. Quantifying hemosiderin is important in studying microbleeds with a particular interest in stroke [52], dementia [53] and MS [54].

In this section, correlations between relaxation rates (R2, R2*, R2'), phase, magnetic susceptibility (QSM) and absolute iron content (both *in vivo* and *ex vivo*) will be summarized. In this thesis, the focus is on imaging iron in the form of ferritin.

R2 method

Local microscopic filed gradients (G) exist due to the presence of ferritin-loaded cells, which lead to the diffuse movement of hydrogen protons [55]. The signal loss from this kind of random movement won't be recovered in spin echo sequence due to the stochastic nature of the Brownian motion [55]. As a result, R2 values are affected by diffusion changes contributed from iron [27]:

$$R2_{total} = R2_0 + R2_{diff} \tag{3.1}$$

where $R2_0$ is the biological relaxation rate which is determined by proton density, field strength, temperature and so forth. $R2_{diff}$ is the relaxation from diffusion, which is defined as:

$$R2_{diff} = (\gamma^2 G^2 D/3) \cdot \tau^2 \tag{3.2}$$

where γ is the gyromagnetic ratio of proton, G is the local microscopic gradient, $D = \delta^2/(2\tau_d)$ which is related to the average step parameters (a spin moves step size of δ every τ_d second). Since the presence of iron affects the local microscopic gradient G, therefore, iron effects can be seen in R2.

R2 can be calculated by using multiple-echo spin echo sequence. Significant positive linear correlations between R2 values and iron concentrations have been revealed in several studies [55-58]. The correlation slopes reported by Langkammer et al and Mitsumori et al were 0.04 Hz per μg Fe/g wet tissue and 0.057 Hz per μg Fe/g wet tissue. In Langkammer et al's study, a 3T magnet was used for scanning, and iron concentration was determined by inductively coupled plasma mass spectrometry (ICPMS). In Mitsumori et al's study, a 4.7T magnet was used and *in vivo* iron concentration was estimated based on Hallgren & Sourander's published iron-age equations [7]. However, all the previous R2 studies measured $R2_{total}$, which includes the confounding term ($R2_0$) for iron quantification. Therefore, this technique had several limitations. First, because the diffusion effect from iron is subtle, $R2_{total}$ is not sensitive enough for measuring iron content. Second, there are also several other factors could have impact on $R2_{total}$ through $R2_0$ such as water content, tissue composition, disease condition, formalin fixation [59] and so forth. Also, R2 varies in magnetic field strength. All of those disadvantages suggest R2 correlates with iron content but it is not accurate enough to do iron quantification.

R2 and R2′ methods*

R2* includes all the effects that can cause dephasing, which is defined as：

$$R2^{*} = R2_{total} + R2' \tag{3.3}$$

R2′ is attributed to all the microscopic, mesoscopic and macroscopic scale field gradients that lead to static dephasing effects, which can be refocused in a spin echo sequence through the 180° rf pulse but not with a gradient echo sequence. For a spherical object embedded in a homogeneous tissue, R2′ can be written as [27]:

$$R2' = \frac{2\pi}{9\sqrt{3}}\eta\gamma\Delta\chi B_0 \tag{3.4}$$

where Δχ is the magnetic susceptibility between the sphere and the background, B_0 is the uniform background magnetic field, η is the volume fraction. This equation shows the linear behavior of R2′ on both volume fraction and change in susceptibility. For cylindrical objects, R2′ is also related to the angle.

The R2′ effect is much stronger than the iron induced diffusion effect embedded in R2. Therefore, both R2* and R2' are more sensitive to iron content than R2 [55, 60]. R2* maps can be generated from a multi-echo spoiled gradient echo sequence. R2* has been shown to be linearly correlated with iron concentration [55, 61, 62]. The previous published R2*-iron correlation slope is 0.27 Hz per μg Fe/g wet tissue according to an *ex vivo* study (3T, iron concentration was measured with ICPMS) [55], and 0.114 Hz per μg Fe/g wet tissue from an *in vivo* study (3T, iron content was estimated based on Hallgren & Sourander's published iron-age equations). A study from Yao et al [62] revealed positive linear correlations between R2* and

iron concentration in three field strengths for both *in vivo* and *in vitro* data. The absolute R2* values and the R2*-iron correlation slopes are different in each field strength with the highest in 7T and followed by 3T and 1.5T. They also showed that there is a nice correlation between iron with R2* change rate (with respect to field strength). However, the results found from *in vivo* and *in vitro* data were not consistent, which could be caused by formalin fixation.

Although R2* is much more sensitive to iron changes than R2, it still suffers the same limitations as R2 because the baseline ($R2_0$) term is also present in R2*. R2* is also affected by magnetic field strength and the object angle as discussed. $R2'$ offers the advantage of not depending on $R2_0$ to measure iron content. However, comparing $R2$ with R2* to extract $R2'$accurately is a difficult procedure and is prone to many errors [63, 64]. Another limitation of this technique comes from the signal loss due to the macroscopic susceptibility effects, which makes measuring R2* in the cerebral cortex and surrounding nasal sinuses difficult [65]. The artifacts due to susceptibility effects will be worse with long echo times and higher magnetic field strengths. Such artifacts can be reduced with a higher-order shimming and higher image resolution.

Phase

Another approach is using phase to estimate iron content [6, 66]. Phase values don't depend on intrinsic relaxation parameters but directly relate to the local magnetic field variations which lead to the spatial distribution of the proton precession frequency.

$$\varphi = \Delta\omega \cdot TE = -\gamma \cdot \Delta B(\vec{r}) \cdot TE \tag{3.5}$$

This method is very sensitive to small amounts of iron which induces changes of the magnetic susceptibility and hence should be more accurate than the noisy T2 and T2* methods.

However, other sources of phase shift also exist such as from magnetic field inhomogeneity at tissue-air interface and imperfect shimming [65]. These shifts are large enough to affect the entire phase image and have to be filtered. In addition, phase values can only be returned correctly if it's between $-\pi$ to π, any degree beyond the range will be wrapped back to this range. Thus, a proper algorithm is a critical step for phase processing. Moreover, another challenging fact of using phase as an indicator of iron concentration is that besides the object susceptibility, phase also depends on the geometry and orientation of the object [62]. As a result, it is more difficult to localize and quantify iron deposition independent of geometry.

Quantitative susceptibility mapping (QSM)

QSM is the most modern MRI approach for estimating iron content. The QSM maps are generated by using an inversion process on the phase images. The details of the theory and processing steps have been introduced in Chapter 2.2. In theory, QSM approach is independent of field strength, echo time, the relative orientation and the shape of the object [67]. The correlations between susceptibility value and iron concentration have been summarized in Zheng et al's recent published paper [67] (Table 3.1). Other than the correlation slopes listed in Table 3.1, Lim et al just published a slope (0.73 ppb/μg iron/g wet tissue) for their new *in vivo* study. However, the published *in vivo* susceptibility-iron correlations were determined from very limited samples. And the way they quoted iron concentrations from the postmortem study [7] were also questionable. The detailed discussion about this can be referred to Chapter 5.

Other MRI methods

The most popular ways of measuring iron with MRI have been reviewed. There are still some other methods proposed to assess iron accumulation such as magnetic field correlation (MFC)

[68] and direct saturation imaging (DSI) [69]. However, these are beyond the scope of this thesis, so the details of those methods won't be addressed here.

In the next chapter, a specific study of measuring putative iron using phase and $\Delta R2^*$ in healthy people will be presented.

Table 3.1: Correlation between susceptibility mapping and iron concentration [67].

Authors	Correlation slope *	Structures	Background removal	QSM method	Myelin correction	Field (Tesla)	Sample	Iron
Zheng et al. (2013)	1.28~1.33	N.A.	Quadratic fitting	Forward fitting	N.A.	3T	Ferritin	ICPMS
Zheng et al. (2013)	0.83	GP,PUT,CN	SHARP	TKD (SO)	No	3T	Cadaver brain	XRF
Haacke. (2012)	0.59	GP,PUT,CN	SHARP	TKD (SO)	No	3T	*In vivo* brains	H&S
Shmueli et al. (2009)	0.56	PUT,RN, SN	Polynomial fitting	TKD (SO)	No	7T	*In vivo* brain	H&S **
Wharton et al. (2010)	0.75/0.6	GP,SN, RN,PUT,CN,TH,GM	Simulated geometric effect+fitting	TKD (MO/TSO)	No	7T	*In vivo* brains	H&S
Langkammer et al. (2012)	0.89	GP,PUT, CN, TH	SHARP	HEIDI (SO)	No	3T	Non-fixed Cadaver brains	ICPMS
Schweser et al. (2011)	1.30	GP, SN, DN,PUT, CN, TH, WM,GM	SHARP	MO regularization	Yes	3T	*In vivo* brains	H&S
Schenck (1992)	1.32 (1.27*)	N.A.	N.A.	N.A.	N.A.	N.A.	N.A.	N.A.

*The unit of the slope is 1ppb/μgFe /g wet tissue (ρ=1.04g/ml at 36.5 ºC) for wet tissue; the unit for the ferritin solution is 1 ppb/μgFe/ml and the corresponding theoretical value is 1.27 ppb/ μgFe/ml.

**H&S: (Hallgren and Sourander, 1958); SO: single orientation; MO: multiple orientation; TKD: thresholded k-space division.

Chapter Four Correlation of putative iron content as represented by changes in phase and R2* with age in deep gray matter nuclei of healthy adults

Introduction

In this chapter, both phase and $\Delta R2^*$ methods for measuring iron in the brain will be considered. We will specifically discuss the concept of two-region analysis where a given area of the brain is broken up into low and high iron content areas. In the later section of this chapter, an application of this iron quantification method is presented for normal controls.

Iron has long been recognized to play a key role in brain function such as oxygen transport, neurotransmitter synthesis, electron transfer, and myelin production [1, 2]. Despite the positive implications when in a free ferrous form, iron is known to be toxic and lead to free radical production. Recently, there has been a renewed interest in the role of iron in neurodegenerative diseases such as multiple sclerosis, Parkinson's disease, Alzheimer's disease and other conditions including aging [1, 2, 47, 70, 71]. Due to the importance of iron in the human body, any iron misregulation can be a major factor and can be used as a marker for neuronal death and other pathological evidence in neurodegenerative diseases [72]. For instance, the disturbance of iron metabolism can occur at several levels: iron uptake and release, storage, intracellular metabolism, and regulation. However, the body has a number of ways to deal with this issue by storing excess iron in the form of ferritin or hemosiderin. Ferritin appears to be the normal form of iron storage while hemosiderin often appears when there has been bleeding and macrophages, and this fact can be used to help consolidate the iron form [70, 73, 74].

Using methods such as diaminobenzidine acid enhanced Perl's staining has revealed iron in many cell types of the central nervous system, such as neurons, microglia, oligodendroglia, astrocytes and in some myelin sheaths [75]. Iron is also found to be of higher concentration in gray matter (GM) than in white matter (WM) [76]. Deep gray matter structures accumulate ferritin at different rates at different ages [7, 75, 77]. It is believed and often quoted [7] that iron deposition increases quickly

with age and then levels off or increases more slowly. Furthermore, it has been shown that there are major iron deposits in the form of ferritin associated with the basal ganglia [78, 79]. The interest in iron has led to attempts to quantify iron *in vivo* in neurodegenerative diseases in order to understand their pathogenesis, monitor their progress and determine neuroprotective treatments.

Iron Quantification: previous approaches and SWI

A variety of methods have been proposed attempting to measure iron with magnetic resonance imaging (MRI), including: T2, T2*, T2' [60, 80], field dependent relaxation rate increase (FDRI) [81, 82], magnetic field correlation (MFC) [65] and susceptibility weighted imaging (SWI) [8]. Although R2 (or 1/T2) related methods using a spin echo sequence have been shown to be more sensitive to GM/WM differentiation than R2', it has not been able to show clear specificity for iron [80] in diseases such as Parkinsons because of confounding issues such as variable water content. On the other hand, R2' has been shown to yield a good correlation with iron load, as R2' was seen to increase for higher iron content structures. Individual T2 relaxation times showed more variation after 45 years of age [83]. In R2' and R2* methods, R2' and R2* increased in GM but decreased in WM as a function of age [84].

Recently, SWI [32, 85] has been used to measure or at least infer iron content in brain parenchyma [8, 32, 86]. A recent comparison study between SWI and others sequences [12] confirmed that SWI can be used as a tool to quantify iron deposition in the brain. Other studies [66, 87] have also tried to probe brain iron with SWI by investigating the pattern of mineralization in the deep gray matter as a function of age. To date, many researchers have looked at total iron content in specific regions of the brain such as basal ganglia and thalamus, but no one has yet focused on establishing either the regional changes of high iron content or how much iron content in this specific region changes as a function of age.

Iron quantification using gradient echo-based SWI data

In the following discussion, we focus on introducing the basic elements of iron quantification using SWI in seven deep grey matter nuclei: caudate nucleus (CN), globus pallidus (GP), putamen (PUT), pulvinar thalamus (PT), substantia nigra (SN), red nucleus (RN), and thalamus (THA). The regions of interest (ROIs) are outlined manually based on their anatomical locations and the boundaries shown in the high-pass filtered SWI phase images (Figure 4.1). These structures are measured bilaterally.

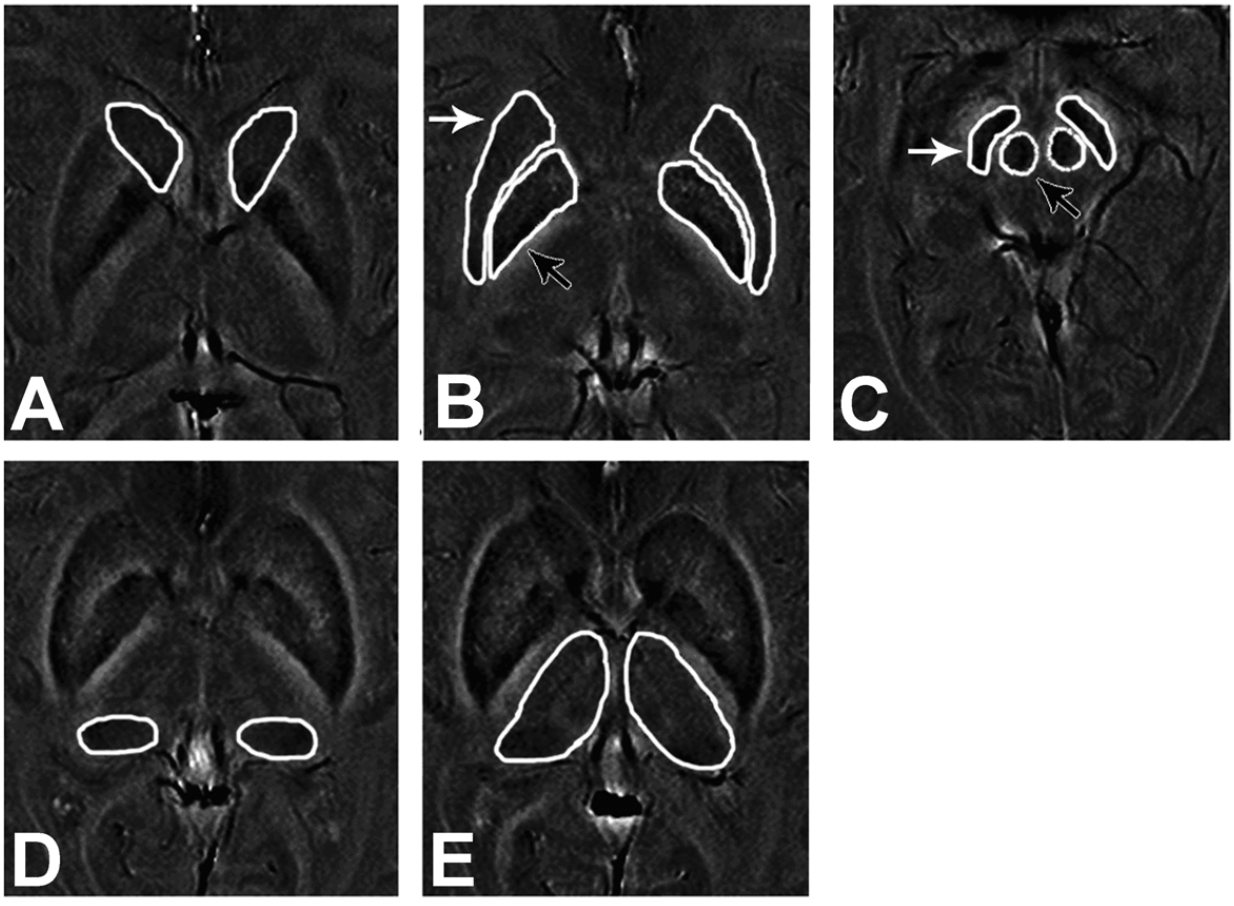

Figure 4.1: Example boundaries are shown for: A) caudate nucleus, B) globus pallidus (black arrow) and putamen (white arrow), C) red nucleus (black arrow) and substantia nigra (white arrow); D) pulvinar thalamus, and E) thalamus.

Drawing the ROIs:

One or more slices can be selected for analysis accordingly. The selected slices should show a well-defined border for the structures of interest. As a further condition, slices severely affected by sinus artifacts cannot be used. The bright boundaries outside the structures are also avoided because this large positive phase shift is most likely associated with the iron-induced dipolar field patterns in the tissue [88]. Checking the boundary in adjacent slices is also necessary for making sure that the traced boundary is right. If a single slice analysis is sufficient, then the selected slice should show the largest area and agree with the above requirements.

Structures are zoomed by a factor of four to make the boundaries easier to determine and avoid the iron-induced dipolar field. ROIs are drawn first on the phase images and then copied to the magnitude images, this guarantees that the boundaries are exactly the same in both magnitude and SWI filtered phase images.

Here are some criteria for slice selection of different structures if just a single slice is chosen for analyzing each structure. Separate slices are chosen for the CN, the GP and the PUT respectively. The slice for the PT is chosen to have the highest contrast on the phase images and to avoid the SN or RN structures and the major veins. The RN and SN are drawn on the same slice that shows the ring-like hyperintensity signal outside the RN , and shows no fusion of the SN and RN. For the thalamus, the slice that clearly shows the boundary without showing the RN or subthalamic nucleus is selected. Also, the internal capsule needs to be avoided while drawing the ROI around the thalamus. Boundaries drawn for these structures are shown in Figure 4.1.

Phase units and SWI processing using SPIN

The ability to quote iron, say, in micrograms of iron per gram tissue (μg Fe/g tissue), depends on associating a given phase value (preferably in radians) with an amount of iron. Each manufacturer stores phase values in different ranges and even the same manufacturer can use different phase

units from one version of software to another. For example, General Electric (GE) uses the range -3142 to 3142 to represent $-\pi$ to π radians. One the other hand, Siemens Phase Unit (SPU) is the scale used in Siemens MR Systems to represent phase information of the MR signal. This scale ranges from 0 to 4096 which is equivalent to $-\pi$ to π in radians.

For a right-handed system, 0 corresponds to $-\pi$, 2048 corresponds to 0, and 4096 corresponds to π. On the other hand, for a left-handed system, 0 is π and 4096 is $-\pi$. If the scanner uses SPU, observers need to know whether the scanner uses right or left hand system. One easy way to judge which system the scanner uses is to check the veins and grey matter in the phase images (without inversing). If they are hypo-intense (appear dark), then it is a right-handed system, whereas if they appear hyperintense (bright), it is a left-handed system. In principle, in order to compare with other systems, one should always convert the phase values into radians. (Another versions of Siemens software is now using -4096 to 4096 and similar transformations must be considered to properly record the phase in radians instead of these arbitrary units.)

After getting the magnitude and unfiltered phase images, SWI processing is done using SPIN (Signal Processing in NMR, Detroit, MI, USA). The function is under Process>MIP/SWI Processing>MIP with Phase Multiplications (SWI processing). Following the diagram, two sets of images will be obtained: the high pass filtered phase images (HP) and the Minimum Intensity Projection (MinIP) images. When the images are from a left-handed system, "positive" needs to be selected, whereas if the images are from a right-handed system, choose "negative". The high pass filter is used to remove the low-spatial-frequency inhomogeneities caused by background fields and air/tissue interfaces [89]. People usually use 64×64 or 32×32 as the filter size because these have minimal effects on contrast for most small structures [1, 2, 90]. To obtain the MinIP images, a phase mask f(x) is generated from the filtered phase image and used to create the fusion image, SWI(x), by multiplying the magnitude image $\rho(x)$ by the phase mask four times, that is: $SWI(x) = \rho(x)f^4(x)$ [31].

Two-region analysis:

Each structure can be seperated into two regions which contains high iron and low iron using appropriate thresholds. The reason we analyze both a low iron content region (RI) and a high iron content region (RII) is that an entire ROI analysis may reduce the sensitivity to more subtle changes in iron content (Figure 4.2). The images are usually zoomed by a factor of 4 in the areas of interest before starting preforming the two region analysis. To automatically separate these two regions, thresholds related to phase for different structures are used according to literature [90]. The thresholds are set using the measured mean value minus two times the standard deviation across an elderly population (age range 55 to 85 years) to be on the conservative side as outlined in a study by Haacke et al [90]. For pulvinar thalamus and thalamus which were not included in these papers, we analyzed twenty normal cases which were randomly chosen from the subjects to get the mean value and standard deviation. These phase thresholds mentioned above are from a right-handed system data. For left-handed system data, the thresholds need to be adjusted by subtracting from 4096 SPU. Threshold values are shown in Table 4.1.

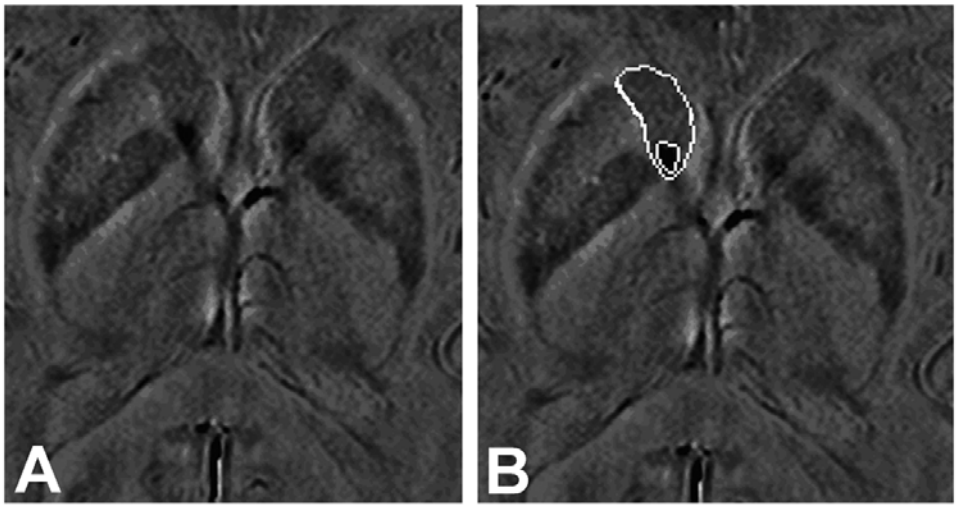

Figure 4.2: An example of a two-ROI analysis in the caudate nucleus. The low iron region is denoted as RI and the high iron region as RII. The thalamostriate region is shown in A) and again in B) with the smaller region being the high iron content region and the larger region being the total region (RI + RII). The mean of the total region is 1989 SFU, while mean of RII is 1741 SFU. This data is from a normal healthy volunteer.

Table 4.1: Threshold values for the regional separation

	CN	GP	PUT	PT	SN	RN	THA
Phase (rad, left-handed system)	0.190[a]	0.172[a]	0.330[a]	0.143[b]	0.356[a]	0.261[a]	0.049[b]
Phase (SPU) (left hand system)	2172[a]	2160[a]	2263[a]	2141[b]	2280[a]	2218[a]	2080[b]
Phase (SPU) (right hand system)	1924[a]	1936[a]	1833[a]	1955[b]	1816[a]	1878[a]	2016[b]
Magnitude (arbitrary unit)	117[b]	84[b]	112[b]	126[b]	90[b]	101[b]	118[b]

PUT: Putamen. CN: Caudate Nucleus. GP: Globus Pallidus. RN: Red Nucleus. PT: Pulvinar Thalamus. SN: Substantia Nigra. THA: Thalamus.
[a] Determined from [90]
[b] Determined from 20 normal cases randomly selected from the sample
SPU = Siemens phase unit
rad = radian

For a right handed system, phase is given by

$$\varphi = -\gamma \cdot \Delta B \cdot TE \tag{4.1}$$

The choice of echo time is usually determined based on setting the phase of a vein parallel to the main field being π [32]. This yields an echo time of 50ms at 1.5T for a hematocrit of 0.45 while practically, to avoid aliasing, a slightly shorter echo time is chosen, typically 40ms. This value also leads to a good R2* effect and phase effect for vessels perpendicular to the main field. Similarly, 20ms TE is used at 3T and 15ms at 4T and so forth, keeping the expected phase for a given susceptibility constant as the field strength increases. In this case, B_0TE is always $60T \cdot ms$ and the phase images will look the same, except for the SNR of course. When the data are not collected using such TEs, a factor (κ) can be used to "correct" either the measured phase or the thresholds where

$$\kappa = (40/TE)(1.5/ B_0) \tag{4.2}$$

As an example, consider a set of images collected at 1.5T with an echo time of 20ms instead of 40ms. In order to use the thresholds described above, one has to multiply the phase differences by a

factor of $\kappa = (40/TE)(1.5/B_0) = (40/20)(1.5/1.5) = 2$. On the other hand, for the regional analysis, one can also simply divide the threshold values by 2. An important point to remember is that after high pass filtering, the phase of the white matter often has near zero value (or around 2048 in SPU). This is because the WM dominates the low spatial frequency component of the image. To measure the amount of iron, one measures the phase change between the white matter and the region of interest or between the CSF and the region of interest. Although the latter is preferred since CSF contains no iron, we used WM as the baseline because it is generally easier to measure and usually appears as zero phase after filtering.

The conversion of phase from SPU to radian is $(\varphi-2048)\pi/2048$. The phase unit is also possible to be converted to parts per million (ppm) field deviation via $\delta = \Delta\varphi/(5.09\pi)$ [90]. To convert from SPU to μg Fe/g tissue, one can use

$$C_{Fe} = \Delta\varphi/180 \times 60\mu g/cc \times pixel\ number \times pixel\ volume \qquad (4.3)$$

Eq. (4.3) is derived by taking 180 SPU as equivalent to the effect of 60 μg Fe/g tissue [90]. However, based on the results on ΔR2* changes, it is suggested that a phase change of 180 SPU (0.276 rad) could represent as much as 240 μg Fe/g fresh tissue. If this number is used, and we assume a density of 1g/cm^3 for tissue, then the total iron would be calculated as follows:

$$C_{Fe} = \Delta\varphi/180 \times 240\mu g/cc \times pixel\ number \times pixel\ volume \qquad (4.4)$$

In later part of this chapter, we will be showing iron content density expressed in four different units for PUT, PT and SN (Figures 4.14 to 4.16).

ΔR2* and iron content

The magnitude differences are related directly to iron via changes in R2* or ΔR2* [80, 84, 91]. If a multi-echo SWI sequence is used, R2* could be calculated by taking the ratio of the magnitude signal from two echoes to give:

$$\frac{S_2}{S_1} = e^{-\Delta TE \cdot R2^*} \qquad (4.5)$$

We can find R2* that is proportional to the change of iron content from

$$-\frac{1}{\Delta TE}\ln(\frac{S_2}{S_1}) = R2*(Fe) \tag{4.6}$$

Since only a single echo data set was collected (as has been the case here), by taking the average magnitude signals of 10 patients with the lowest iron content as the baseline magnitude value (S_0), the iron content change relative to the lowest iron content patients can be calculated through the ratio of the individual's magnitude signal to the baseline magnitude, which yields:

$$\frac{S_1}{S_0} = e^{-TE\cdot\Delta R2^*} \tag{4.7}$$

where S_1 is the signal from a given patient at any age and S_0 is the baseline signal. Again, we can find ΔR2* that is proportional to the change of iron content from

$$-\frac{1}{\mathrm{TE}}\ln\left(\frac{S_1}{S_0}\right) = \Delta R2^*(Fe) \tag{4.8}$$

For the iron content predicted from magnitude signals, we suggest using 67/s for R2* or a corresponding ΔR2* of 1mg Fe/g tissue [8].

Iron quantification: R2* versus Phase

As discussed in the introduction, both R2* and phase have been used to study iron in the brain [66]. Several studies where these two approaches (T2* and phase methods) were used showed good agreement in some structures, but not such good agreement in other structures [60, 80, 92]. Which approach is better likely depends on the amount of iron present and possibly some further complications related to the mechanism of signal loss in T2* and the generation of phase for microscopic structures. The manifestation of each is really quite different.

For large amounts of iron where strong dephasing across a voxel occur, changes in iron content will cause signal loss and therefore a reduction in T2*. However, for smaller amounts of iron where phase dephasing effects across a voxel are small, there may be little noticeable effect on T2* even

in the presence of what could be physiologically a dangerously high level of iron. On the other hand, phase is known to be very sensitive to subtle changes in magnetic field or frequency shift and therefore is much more sensitive to iron in smaller concentrations. As the amount of iron increases, phase and magnitude information start to correlate more strongly showing an almost linear correlation. However, when the iron content is too large, phase aliasing occurs and the linear correlation with phase may disappear. This problem may be avoidable by using a multi-echo SWI sequence in the future and using the short echo data to unwrap the long echo data. From this discussion, the following conclusion can be drawn: T2* underestimates iron content when the amount of iron is small, whereas phase underestimates iron content if iron content is too high (Figure 4.3).

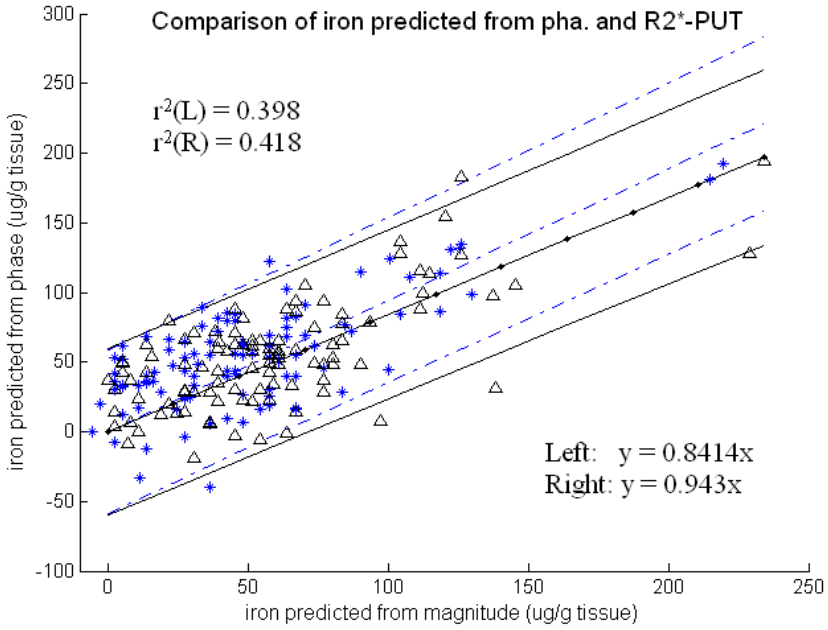

Figure 4.3: A plot of phase iron versus magnitude iron for a series of 100 normal subjects. The correlation is best when larger amount of iron is present. The values are plotted for Putamen in both left and right hemispheres.

Establishing a baseline for normal brain iron content as a function of age

To study iron as a function of age using SWI filtered phase and magnitude images, 100 healthy adults (20-69 years; mean = 43 years) were evaluated using a single gradient echo SWI sequence. The original magnitude and high pass filtered phase data (high pass filtered with a 64x64 homodyne filter) were used to evaluate iron content in the SN, RN, GP, PUT, CN, THA and PT. Each structure was broken into two parts: a high iron content region and a low iron content region.

For all structures except the GP, we found an increase in putative iron content with age both for the total region and for the high iron content region (Figure 4.4 - 4.12). In some cases, the rate of iron deposition increased after the age of 40 years as evidenced in Figure 4.13 and Tables 4.2 and Table 4.3. In the figures that follow, we consider first the different measures of iron that were made: the putative iron in the high iron content region, the average iron per voxel in the high iron content region, the normalized area of the high iron content region, and the average iron (iron density) in the total region. Figure 4.4 shows all four of these iron measures for both $\Delta R2^*$ and phase for one structure that best delineates the iron behavior in the putamen. Figures 4.5 and 4.6 show the putative iron in the high iron content region for both magnitude and phase for the rest of the structures. Figures 4.7 and 4.8 show the putative iron in the whole region for both magnitude and phase. Figures 4.9 and 4.10 show the average iron in the total structure for both magnitude and phase. Figures 4.11 and 4.12 show the normalized area of high iron content region as a function of age for both magnitude and phase. The normalized percent area of high iron content region relative to the total area was used to avoid the influence by the size change for a single structure between individuals. Quantitative results for iron as a function of age for all the structures in terms of the above eight measures are shown in Table 4.2.

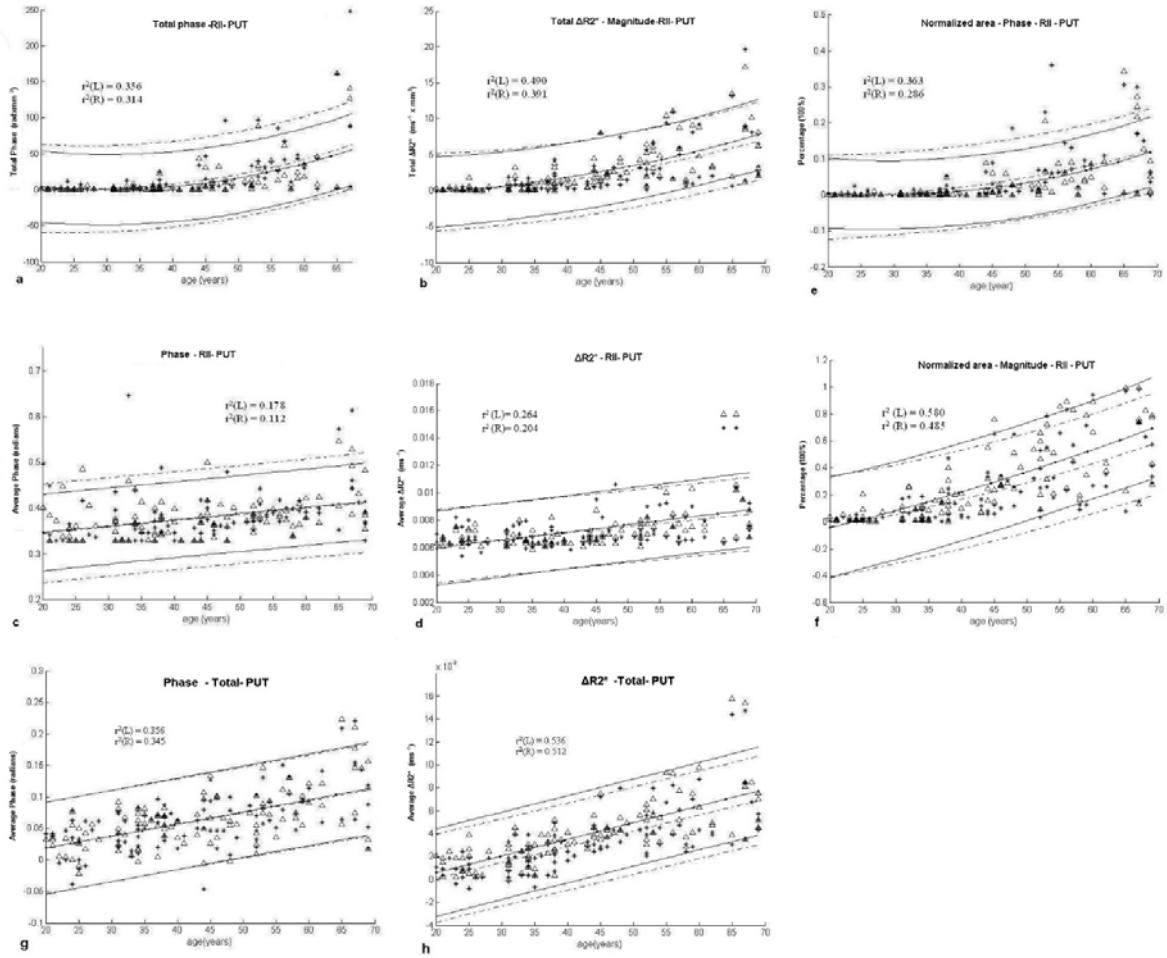

Figure 4.4: Putative iron measurement results as a function of age in Putamen. An increase in iron content - represented here by the increase in phase and ΔR2* - with age for total iron, average iron and the iron area are seen in the PUT. Stars and dashdot line are the values and fit of the right hemisphere. Triangles and solid line are the values and fit of the left hemisphere. r^2 is the coefficient of determination. r^2 is larger for the quadratic fit than just linear fit. L stands for the left hemisphere. R stands for the right hemisphere. Quadratic relationships can be found in plots a, b, e, and f representing the total iron in RII predicted from phase (a) and magnitude (b) and the area in high iron region (phase (e) and magnitude (f)). This effect is not seen in the total region iron for the whole structure (c, d, g, and h).

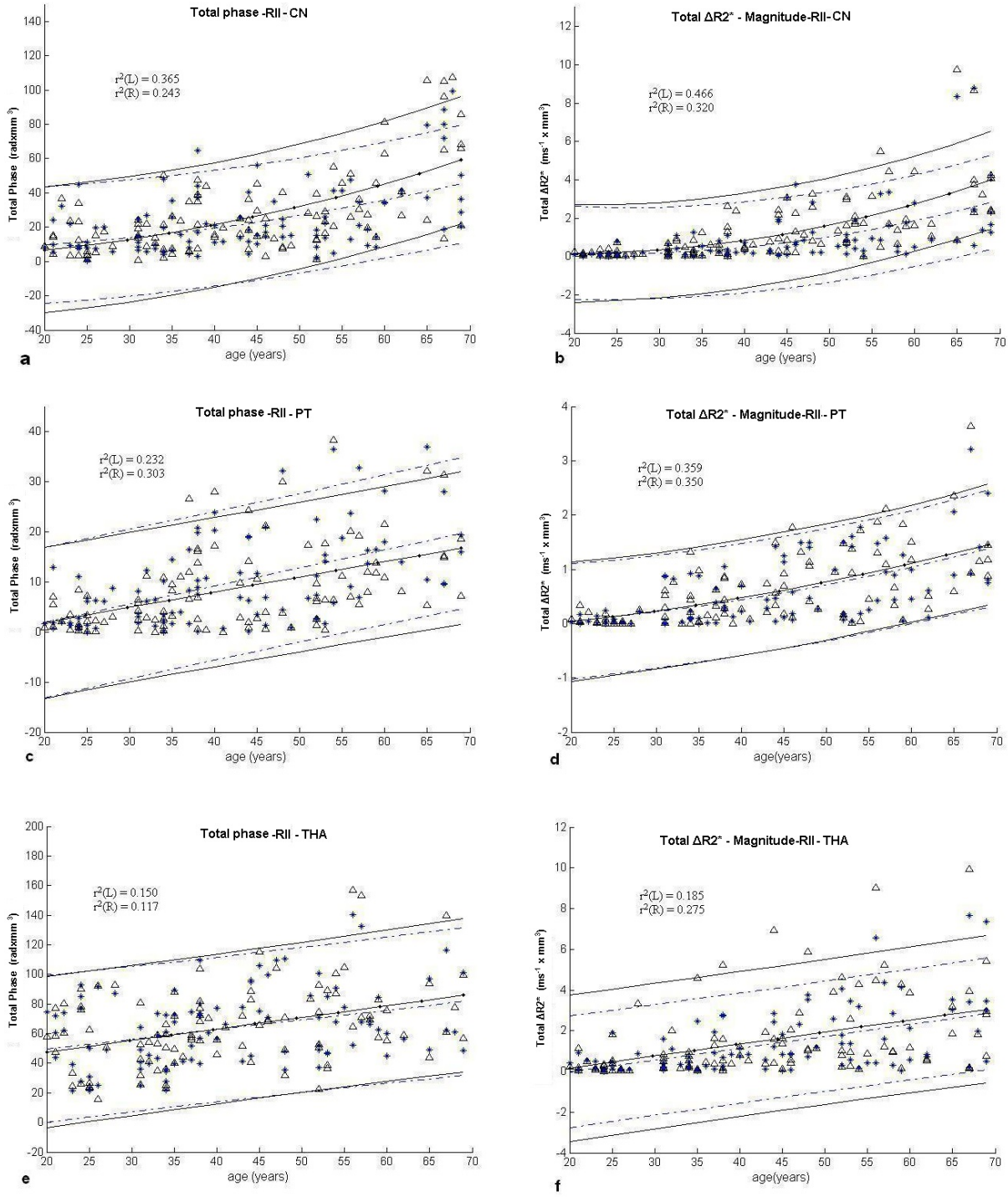

Figure 4.5: Putative iron content - represented here by $phase \times volume$ and $\Delta R2^* \times volume$ - in high iron content region in CN, PT, and THA where iron is seen to increase with age. Iron in CN and PT shows quadratic relationship with age. Stars and dashdot line are the values and fit of the right hemisphere. Triangles and solid line are the values and fit of the left hemisphere. r^2 is the coefficient of determination. L stands for the left hemisphere. R stands for the right hemisphere.

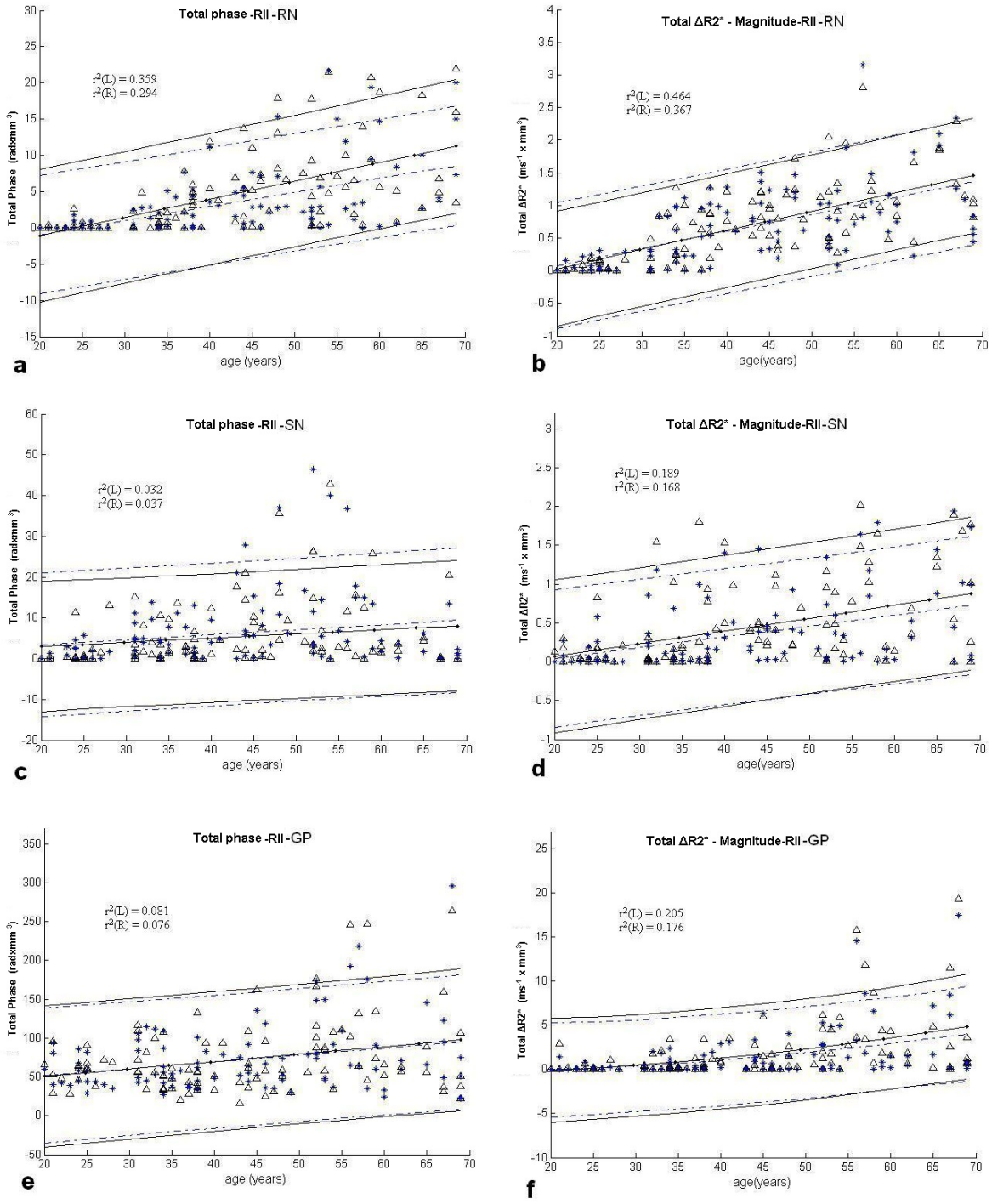

Figure 4.6: Putative iron content - represented here by $phase \times volume$ and $\Delta R2^* \times volume$ - in high iron content region in RN, SN, and GP. In all these structures, a significant increase with age is seen. For GP, iron predicted from magnitude shows quadratic relationship with age. Stars and dashdot line are the values and fit of the right hemisphere. Triangles and solid line are the values and fit of the left hemisphere. r^2 is the coefficient of determination. L stands for the left hemisphere. R stands for the right hemisphere.

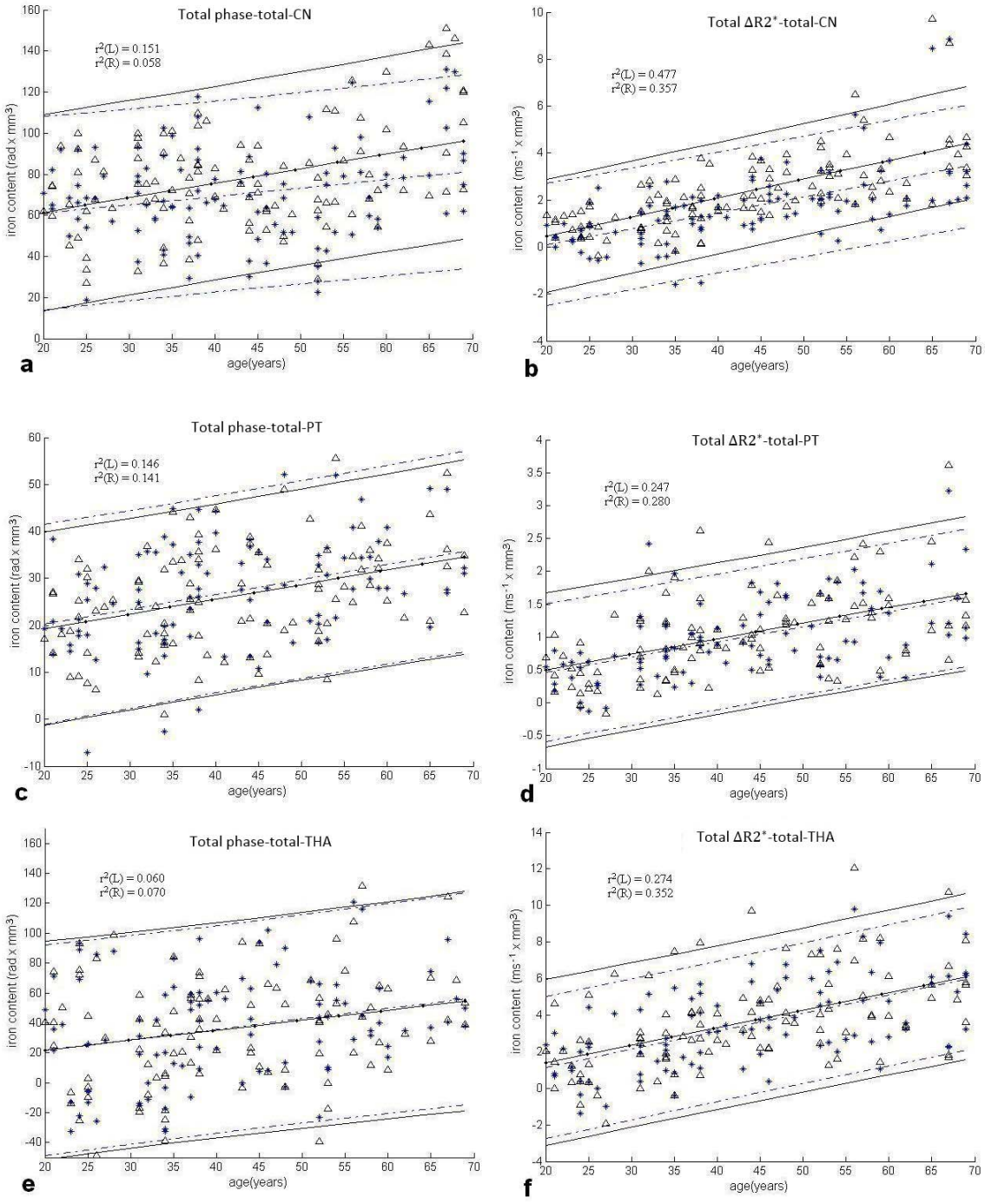

Figure 4.7: Putative iron content - represented here by $phase \times volume$ and $\Delta R2^* \times volume$ - in the whole region in CN, PT, and THA where iron is seen to increase with age. Putative iron in CN, PT, and THA shows linear relationship with age. Stars and dash-dot line are the values and fit of the right hemisphere. Triangles and solid line are the values and fit of the left hemisphere. r^2 is the coefficient of determination. L stands for the left hemisphere. R stands for the right hemisphere.

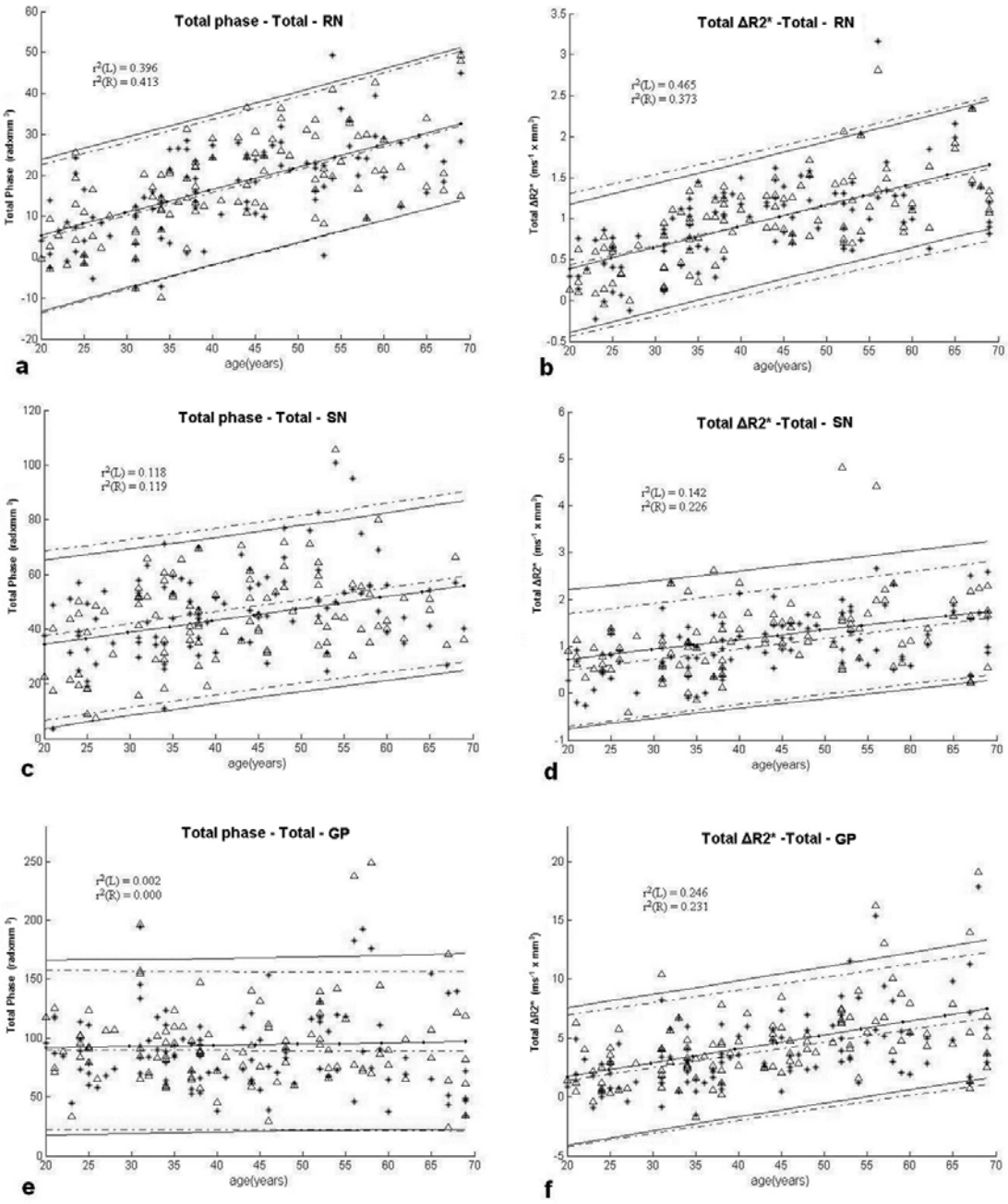

Figure 4.8: Putative iron content - represented here by $phase \times volume$ and $\Delta R2^* \times volume$ - in the whole region in RN, SN, and GP where iron is seen to increase with age except that in GP represented by phase. Putative iron in RN, SN, and GP shows linear relationship with age. Stars and dash-dot line are the values and fit of the right hemisphere. Triangles and solid line are the values and fit of the left hemisphere. r^2 is the coefficient of determination. L stands for the left hemisphere. R stands for the right hemisphere.

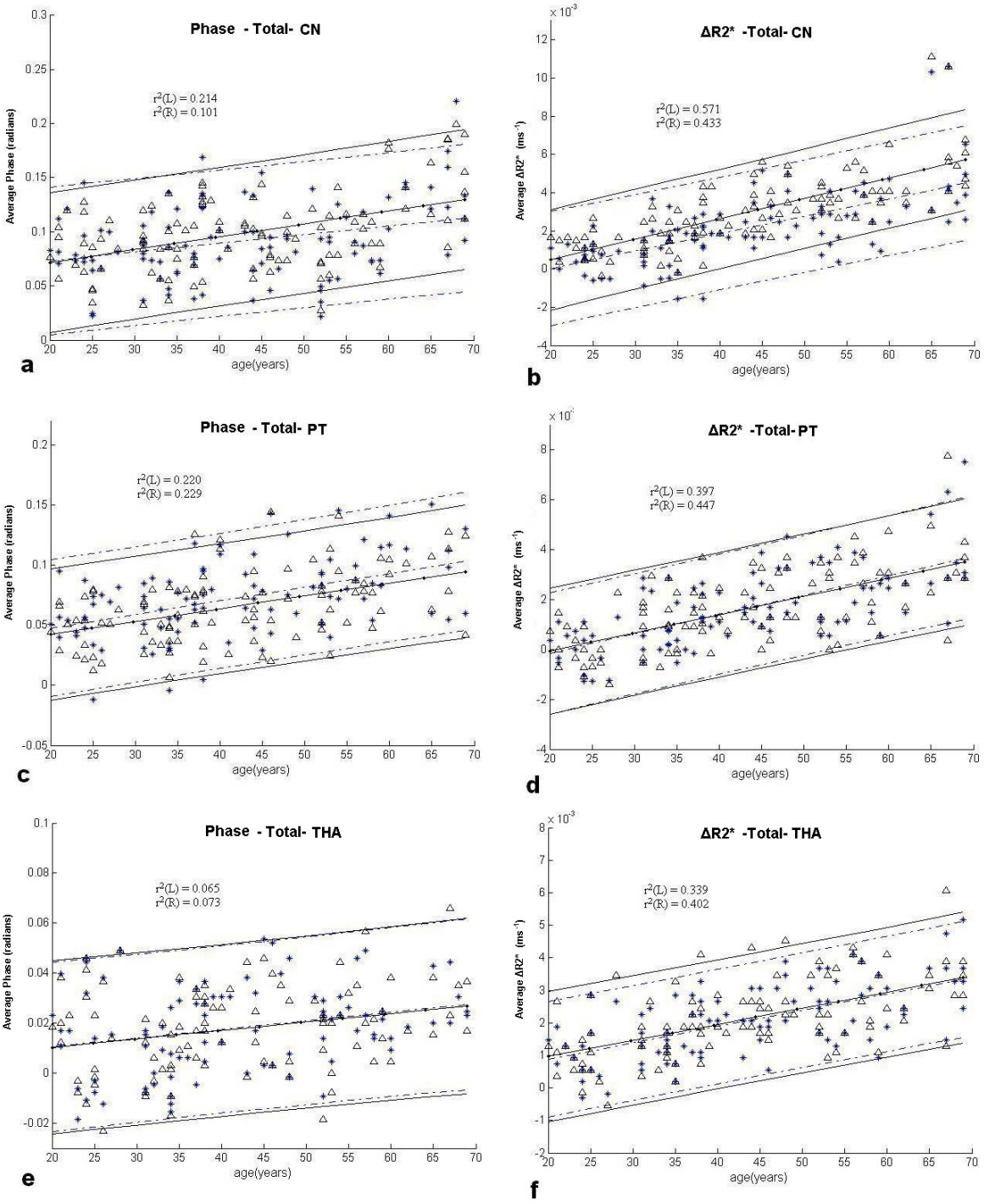

Figure 4.9: Average iron - represented here by average phase and ΔR2* - of the whole structure as a function of age in CN, PT and THA. Stars and dash-dot line are the values and fit of the right hemisphere. Triangles and solid line are the values and fit of the left hemisphere. r^2 is the coefficient of determination. L stands for the left hemisphere. R stands for the right hemisphere.

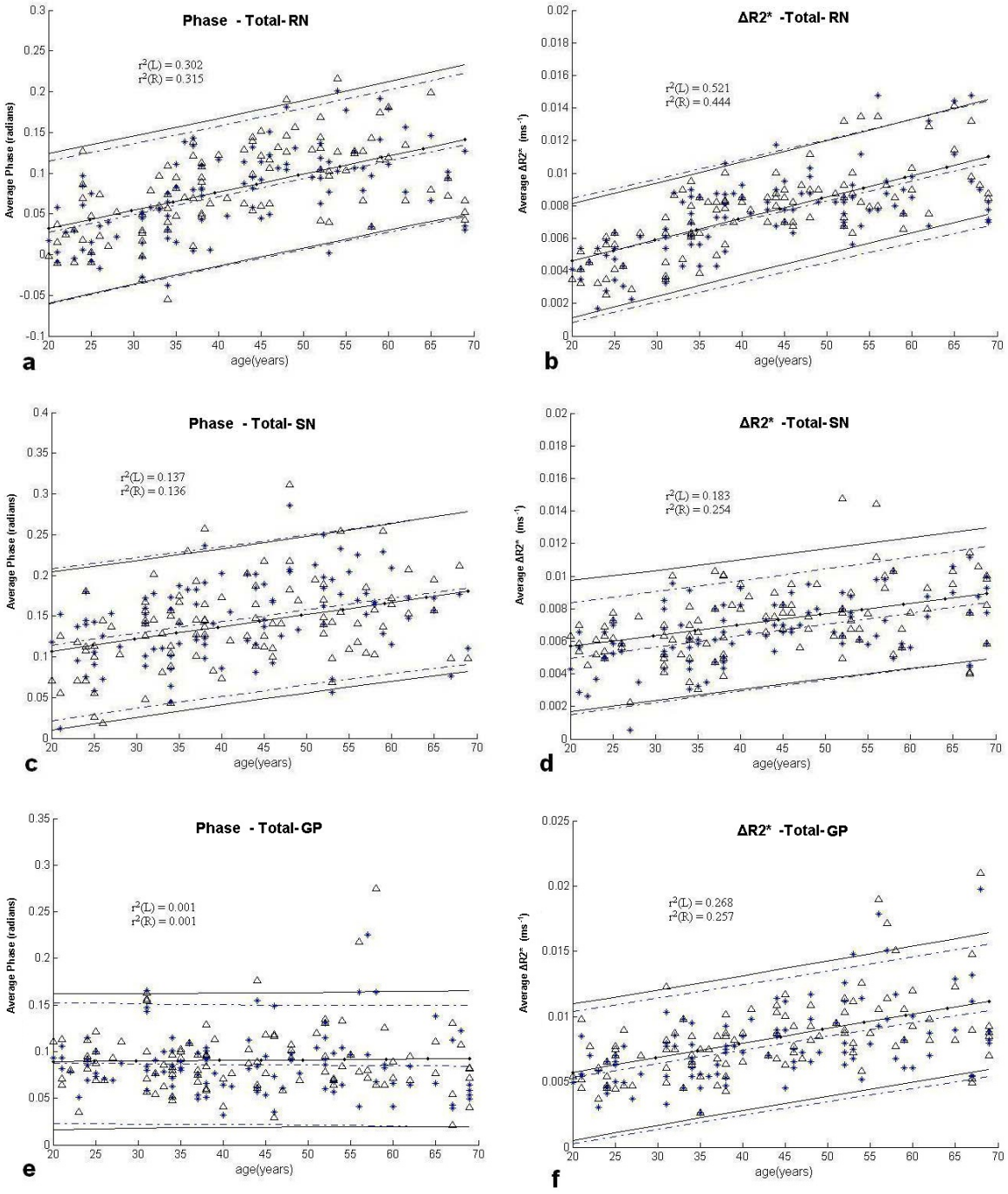

Figure 4.10: Average iron - represented here by average phase and ΔR2* - of the whole structure as a function of age in RN, SN and GP. Stars and dash-dot line are the values and fit of the right hemisphere. Triangles and solid line are the values and fit of the left hemisphere. r^2 is the coefficient of determination. L stands for the left hemisphere. R stands for the right hemisphere.

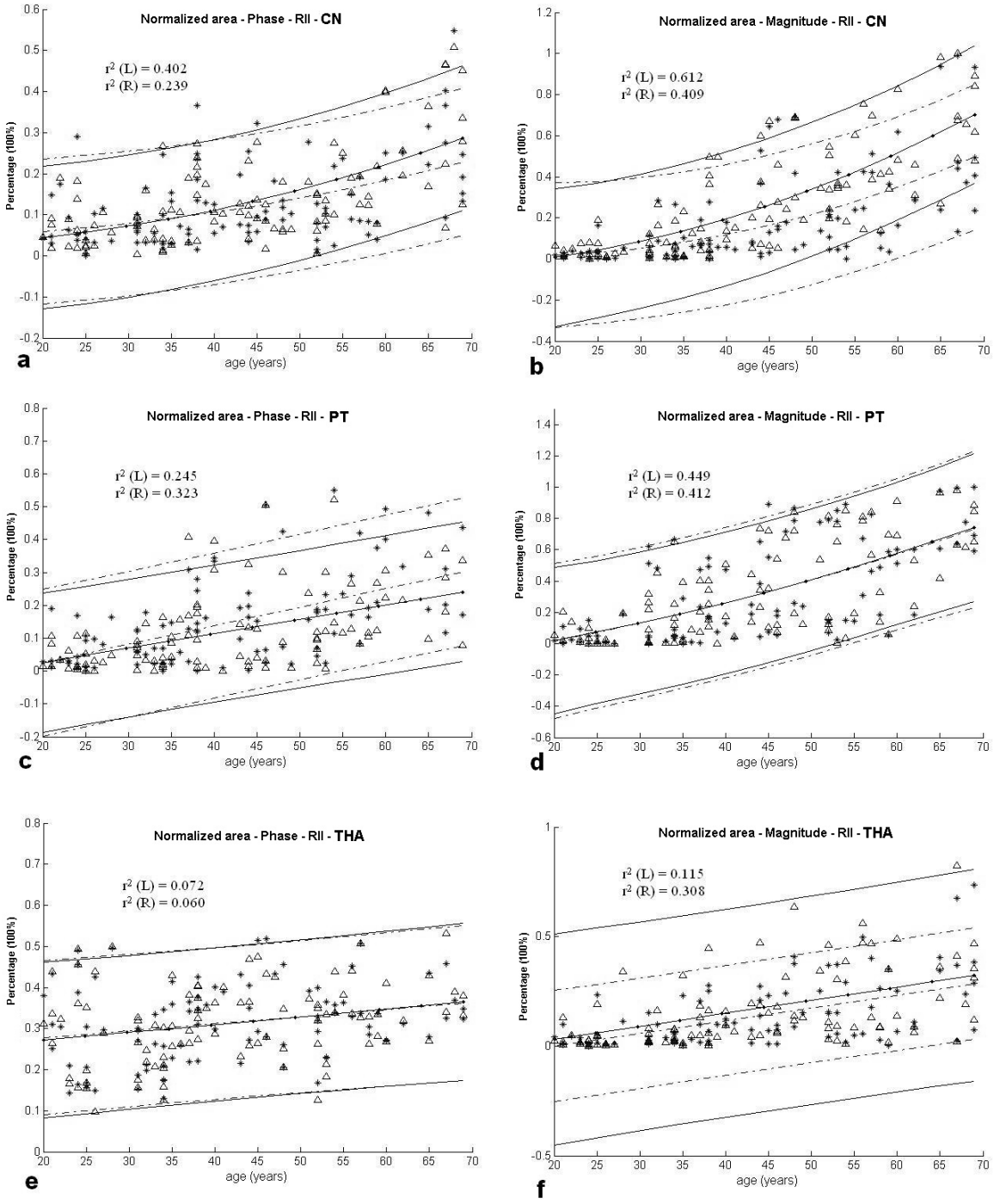

Figure 4.11. Normalized area of high iron content region as a function of age in CN, PT, and THA. High iron content area in CN and PT show strong quadratic relationship with age (increase). Stars and dashdot line are the values and fit of the right hemisphere. Triangles and solid line are the values and fit of the left hemisphere. r^2 is the coefficient of determination. L stands for the left hemisphere. R stands for the right hemisphere.

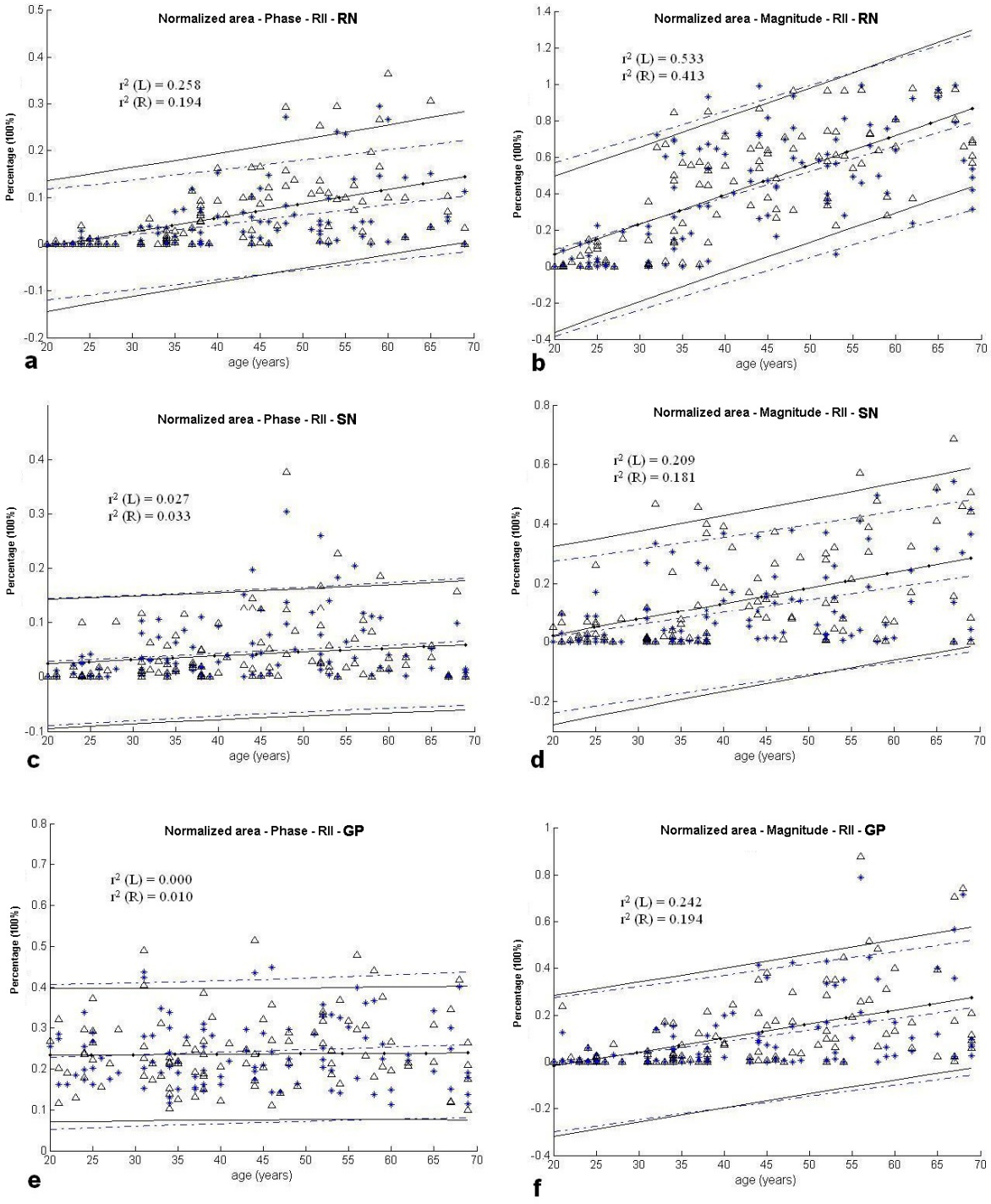

Figure 4.12: Normalized area of high iron content region as a function of age in RN, SN and GP. High iron content area in RN shows significant linear relationship with age. Stars and dashdot line are the values and fit of the right hemisphere. Triangles and solid line are the values and fit of the left hemisphere. r^2 is the coefficient of determination. L stands for the left hemisphere. R stands for the right hemisphere.

Table 4.2: Slopes of phase and magnitude iron measures as a function of age in the two hemispheres

	Age(yr.)	Iron-Phase-RII (rad×mm^3/yr.)			Iron-Phase-Total (rad×mm^3/yr.)			Average iron-Phase-Total (10^{-3} rad/yr.)			Average iron-Phase-RII (10^{-3} rad/yr.)		
		Slope			Slope			Slope			Slope		
		Left	Right	Total	Left	Right	Total	Left	Right	Total	Left	Right	Total
PUT	20-39	0.16±0.08	0.27±0.11	0.21±0.07	2.24±0.81	2.3±0.84	2.27±0.58	2.03±0.63	2.03±0.65	2.03±0.45	0.14±0.93	0.84±1.43	0.49±0.85
	40-69	2.07±0.52	2.21±0.63	2.14±0.41	2.80±0.76	3.00±0.82	2.90±0.56	2.65±0.67	2.60±0.67	2.63±0.47	2.63±0.67	2.65±0.75	2.64±0.50
CN	20-39	0.79±0.32	0.64±0.34	0.71±0.23	0.85±0.52	0.38±0.53	0.62±0.37	1.27±0.73	0.79±0.78	1.03±0.53	0.85±0.53	0.42±0.40	0.64±0.33
	40-69	2.00±0.33	1.35±0.29	1.68±0.22	1.72±0.37	1.19±0.37	1.46±0.27	2.37±0.50	1.77±0.54	2.07±0.37	1.92±0.41	1.56±0.51	1.74±0.33
GP	20-39	-0.21±0.66	-0.03±0.64	-0.12±0.45	-0.20±0.75	-0.38±0.68	-0.29±0.50	-0.07±0.69	-0.24±0.61	-0.16±0.46	-0.29±0.94	0.35±0.71	0.03±0.59
	40-69	1.16±0.91	1.03±0.86	1.10±0.62	0.36±0.68	0.08±0.62	0.22±0.46	-0.14±0.68	-0.10±0.61	-0.12±0.46	1.89±1.57	2.88±1.60	2.39±1.11
RN	20-69	0.25±0.03	0.19±0.03	0.22±0.02	0.55±0.07	0.56±0.07	0.56±0.05	2.23±0.34	2.19±0.33	2.21±0.24	0.97±0.18	0.84±0.16	0.91±0.12
PT	20-69	0.30±0.06	0.36±0.06	0.33±0.04	0.31±0.08	0.32±0.08	0.31±0.08	1.02±0.21	1.09±0.22	1.10±0.15	0.51±0.09	0.55±0.09	0.53±0.07
SN	20-69	0.10±0.06	0.12±0.06	0.11±0.04	0.19±0.12	0.20±0.12	0.19±0.08	1.50±0.39	1.43±0.37	1.46±0.27	0.31±0.21	0.52±0.21	0.41±0.15
THA	20-69	0.78±0.19	0.65±0.19	0.72±0.13	0.67±0.28	0.70±0.27	0.69±0.19	0.34±0.13	0.35±0.13	0.34±0.09	0.62±0.08	0.50±0.08	0.56±0.06

	Age(yr.)	Iron-Magnitude-RII (sec^{-1}×mm^3/yr.)			Iron-Magnitude-Total (sec^{-1}×mm^3/yr.)			Average iron-Magnitude-Total (10^{-3}ms^{-1}/yr.)			Area-Phase-RII (10^{-3} %/yr.)		
		Slope			Slope			Slope			Slope		
		Left	Right	Total	Left	Right	Total	Left	Right	Total	Left	Right	Total
PUT	20-39	0.06±0.02	0.06±0.02	0.06±0.01	0.11±0.04	0.13±0.04	0.12±0.03	0.10±0.03	0.10±0.03	0.10±0.02	0.33±0.17	0.56±0.22	0.45±0.14
	40-69	0.21±0.05	0.19±0.05	0.20±0.04	0.14±0.04	0.16±0.05	0.15±0.03	0.15±0.04	0.14±0.04	0.14±0.03	3.97±1.01	3.76±1.29	3.87±0.84
CN	20-39	0.04±0.01	0.02±0.01	0.03±0.01	0.06±0.02	0.03±0.02	0.04±0.02	0.07±0.03	0.06±0.03	0.06±0.02	4.21±1.72	3.51±1.95	3.86±1.28
	40-69	0.11±0.03	0.08±0.03	0.10±0.02	0.09±0.02	0.07±0.02	0.08±0.02	0.12±0.02	0.09±0.03	0.10±0.02	8.75±1.50	6.01±1.48	7.38±1.06
GP	20-39	0.02±0.02	0.02±0.02	0.02±0.01	0.07±0.06	0.06±0.05	0.07±0.04	0.07±0.05	0.07±0.04	0.07±0.03	-0.75±2.06	-0.45±1.90	-0.6±1.39
	40-69	0.13±0.06	0.10±0.05	0.11±0.04	0.10±0.05	0.07±0.05	0.09±0.04	0.07±0.05	0.07±0.05	0.07±0.03	-0.03±1.50	-0.65±1.38	-0.34±1.01
RN	20-69	0.03±0.00	0.03±0.00	0.03±0.00	0.03±0.01	0.02±0.00	0.02±0.00	0.13±0.01	0.12±0.01	0.13±0.01	3.02±0.52	2.14±0.44	2.58±0.34
PT	20-69	0.03±0.00	0.03±0.00	0.03±0.00	0.02±0.00	0.02±0.00	0.02±0.00	0.07±0.01	0.08±0.01	0.08±0.01	4.40±0.80	5.64±0.85	5.02±0.59
SN	20-69	0.02±0.00	0.01±0.00	0.02±0.00	0.02±0.01	0.02±0.00	0.02±0.00	0.07±0.01	0.07±0.01	0.07±0.01	0.71±0.42	0.76±0.42	0.73±0.30
THA	20-69	0.06±0.01	0.06±0.01	0.06±0.01	0.10±0.02	0.10±0.01	0.10±0.01	0.05±0.01	0.05±0.01	0.05±0.00	1.92±0.72	1.72±0.71	1.82±0.50

PUT: Putamen. CN: Caudate Nucleus. GP: Globus Pallidus. RN: Red Nucleus. PT: Pulvinar Thalamus. SN: Substantia Nigra. THA: Thalamus

For PUT, CN, PT, and GP, the measures related to the high iron content region showed an impressive quadratic relation with age (Figure 4.4a, 4.4b, 4.4e, 4.4f, 4.5a, 4.5b, 4.5d, 4.6f). Generally, the results seemed to be fairly flat in the first two decades (20–40 years), but the local iron content dramatically increased after 40 years of age. Increases occurred not only in the area of the iron deposition but also in the average iron content. Fitting the data to two separate curves for 20–40 years old and 40–70 years old shows more clearly the dichotomous iron behavior in these two age ranges (Figure 4.13). This rapid growth of iron build-up is not easily seen in the whole structure iron analysis where only a linear relationship with age is seen (Figure 4.4g and h and Figures 4.7–4.10).

The resultant iron deposition level changes depending on whether one examines the average iron deposition in the whole structure, iron in the high iron content region (RII), or average iron in RII. The order of the structures from the highest (scales as 1) to lowest (scale as 7) is shown in Table 4.3. All these changes may tell us something new and different about the iron deposition in each structure. Comparing structures for both hemispheres, we found some phase- and magnitude related measures of iron content showing significant differences between the two hemispheres. Most of the time, the left hemisphere contains more iron than the right hemisphere (Tables 4.4 and 4.5). Statistically, the PUT, CN, GP, and RN showed the largest effect. In addition, from Table 4.2, it appears that the slope of the linear fit of these measurements in the left hemisphere was always higher than that in the right hemisphere, except for the PT and the SN.

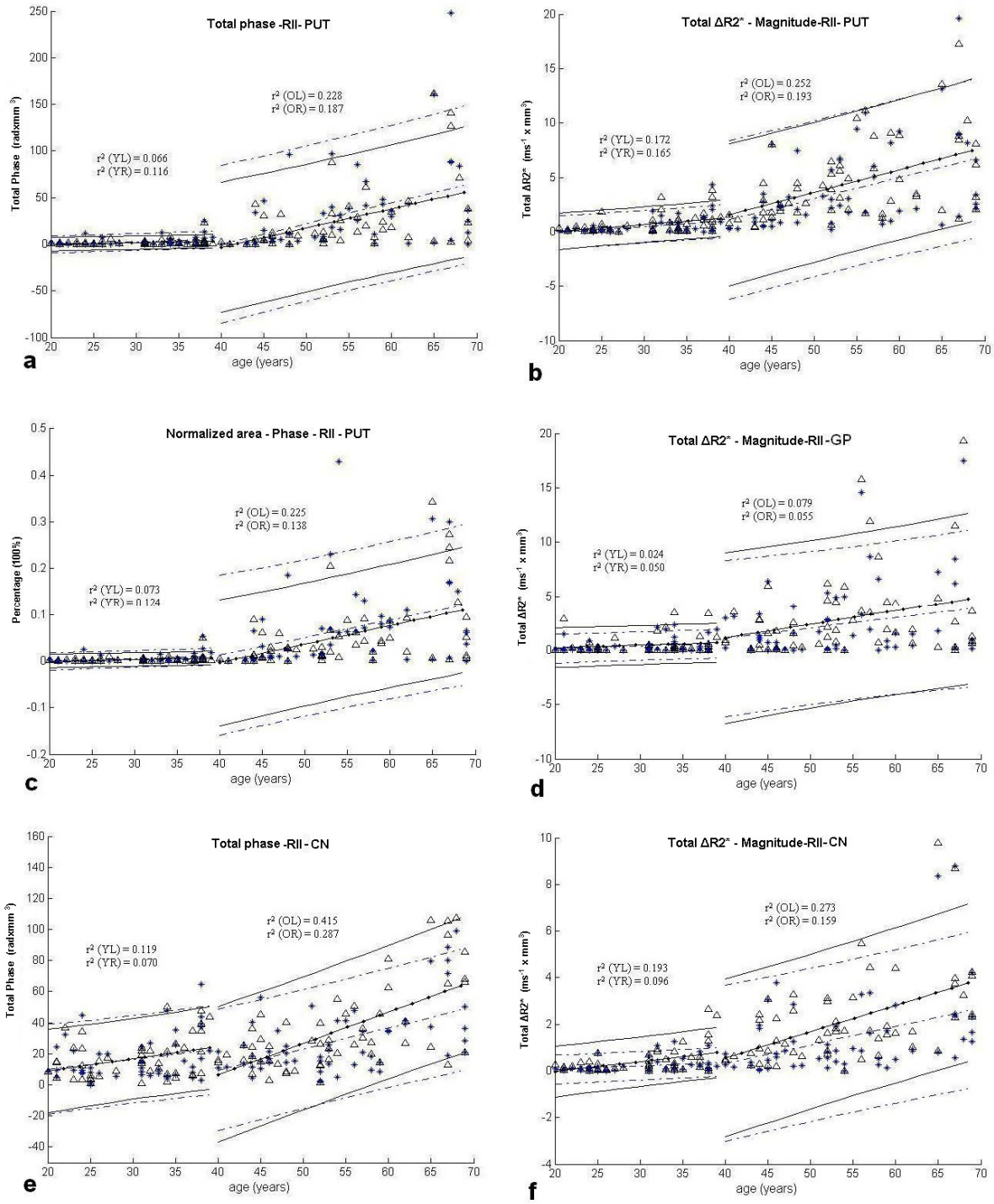

Figure 4.13: Putative iron content in two age intervals - younger and older than 40 years old subjects - giving a clear idea about iron deposition changes. Stars and dashdot line are the values and fit of the right hemisphere. Triangles and solid line are the values and fit of the left hemisphere. r^2 is the coefficient of determination. L stands for the left hemisphere. R stands for the right hemisphere.

Table 4.3: The orders of high to low iron deposition over time.

		PUT	RN	CN	PT	SN	GP	THA
Phase	Average iron (whole structure)	1	2	3	4	5	6	7
	Iron in RII	1	6	2	5	7	3	4
	Average iron in RII	1	4	3	6	7	2	5
Magnitude	Average iron (whole structure)	1	2	3	4	5	6	7
	Iron in RII	1	5	3	5	6	2	4
	Average iron in RII	3	2	4	5	6	1	7

Comparison between this study with some other studies

It is well known that iron deposition in the brain increases with age [7, 8, 66, 76, 93]. The work by Hallgren and Sourander has been considered the standard reference for brain iron quantification [7], which presents a wide belief that iron in the brain levels off after a certain age (30-40 years old) for many structures. For instance, many studies have shown that iron level is low in newborn brain and quickly increases during rapid brain growth which concurs with the peak of myelinogenesis [73] until the age of 20 to 30, and then it reaches stable levels [7, 94]. However, this was not seen in all brain structures. Hallgren's and Sourander's work showed that iron in the globus pallidus increased until the age of 30 years old. Their results also suggest that the iron increase in the putamen and the caudate nucleus is slow and reaches a maximum value around the age of 60 years old. On the other hand, the iron level in the thalamus reaches its peak at the age of 30 years old, and then appears to decline after that age. Recent studies used phase information to evaluate iron content in the brain [66, 88, 95]. For instance, Xu et al. [66] showed that iron uptake remained age dependent in the putamen, red nucleus and frontal white matter but not in the globus pallidus, substantia nigra and caudate nucleus where, after a rapid increase in the first two decades, iron reaches a plateau.

Putamen: Our results showed that iron content in the putamen remained age dependent throughout 5 decades and are in agreement with results of Xu et al [66]. This agrees with Hallgren's and Sourander's work which showed that iron in the putamen was age dependent and did not reach its maximum until the 6th decade, in agreement with a study by Aquino et al. [92] showing a slow rate of increase and a variability after the age of 50. We found that both the volume of affected tissue with high iron content and the average iron content per pixel increased with age, and in some cases the rate of iron deposition are dramatically changed after the age of 40 years old in the following structures: PUT, CN, GP and PT. This increase in iron may not be as rapid as that occurs in the first two decades of life, but nevertheless is present in most people (Figure 4.13a, b and c).

Red nucleus: Our results showed that iron content in the red nucleus remained age dependent throughout the 5 decades we studied and are in agreement with Xu et al.'s results [66]. However, Hallgren and Sourander's work showed a rapid increase in the first 2 decades (first 2 decades data were not available in our study), whereas no conclusions were drawn regarding iron in the red nucleus after the age of 20 due to technical difficulties.

Globus pallidus: In several studies [7, 78], iron in the globus pallidus was shown to increase rapidly and level off after the age of 30 years old, whereas our results as well as Xu et al.'s [66] show a linear decrease as a function of age. From Table 4.2 one can see that the iron concentration in RII grows very fast with age, but the iron concentration in the whole structure grows more slowly. As a result, we believe that the two region analysis is necessary for detecting more subtle brain iron changes.

Substantia nigra: None of these studies (including our study) showed significant changes in SN iron content as a function of age (Figure 4.16). However, the Hallgren and Sourander work showed a rapid increase in the first 2 decades and inconclusive results for older ages, and Aquino et al. [92] showed a rapid increase until the age of 15, and then the iron content reaches a plateau (note that our study did not cover the age range from 0 to 19 years old). No correlation with our study can be

drawn since the first two decades data were not available.

Caudate nucleus: According to Hallgren and Sourander, the iron in the caudate nucleus was seen to behave in a similar fashion to the putamen, showing a slow increase reaching a maximum value at age 60 years old. Xu et al [66]. showed that iron in the caudate nucleus increased slightly with age. Both results contrast with our results as we see increases in iron content with age using the two region-of-interest analysis. On the other hand, Aquino et al. [92] showed an almost flat iron content with age. For the CN, we have found that iron increased slowly in the early ages, but this rate rises dramatically after the age of 40 (Figure 4.5a, b).

Thalamus: According to Hallgren and Sourander, iron in the thalamus increased in the early stages, reached a maximum at the age of 30, and then it started declining. Xu et al. showed that iron in the thalamus is almost constant with respect to age. However, our results showed that iron in this structure increases linearly with age (Figure 4.9e, f).

Pulvinar thalamus: The pulvinar thalamus has not yet been analyzed for its iron content in the literature. Here, we show that the iron concentration in the PT increased linearly with age similar to the rest of the basal ganglia and main body of the thalamus (Figure 4.15). The PT is of particular interest in the study of multiple sclerosis where it appears as if major increases in iron content can occur for subjects under the age of 40 years old.

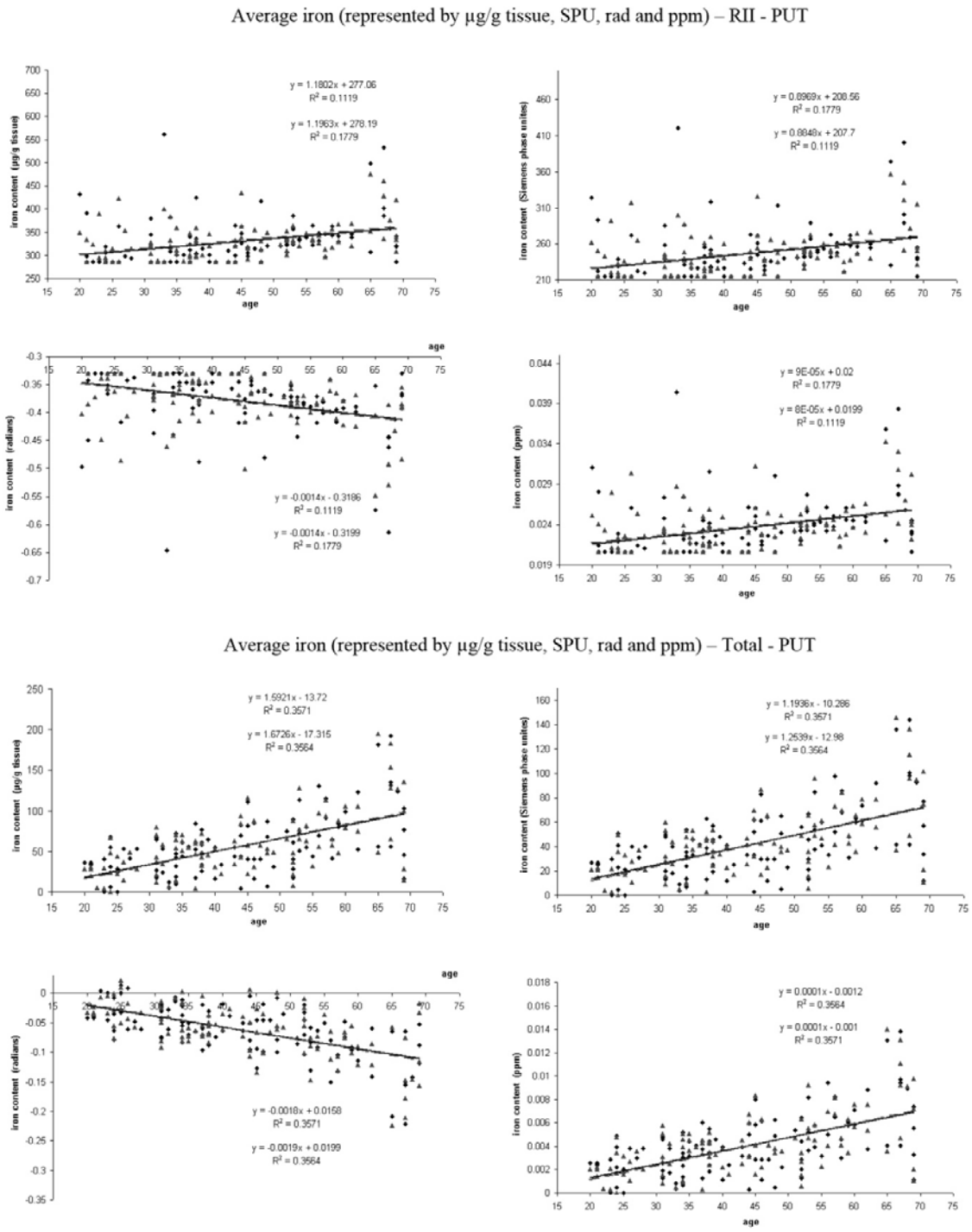

Figure 4.14: Expressing average iron content (iron density) in the PUT for RII and the whole region with different units: µg Fe/g tissue, Siemens phase units (SPU), radians and ppm. The solid triangles and squires are for the left and right side PUT for normal subjects. The dashed line and solid line are the fits of the left and right PUT for normal subjects.

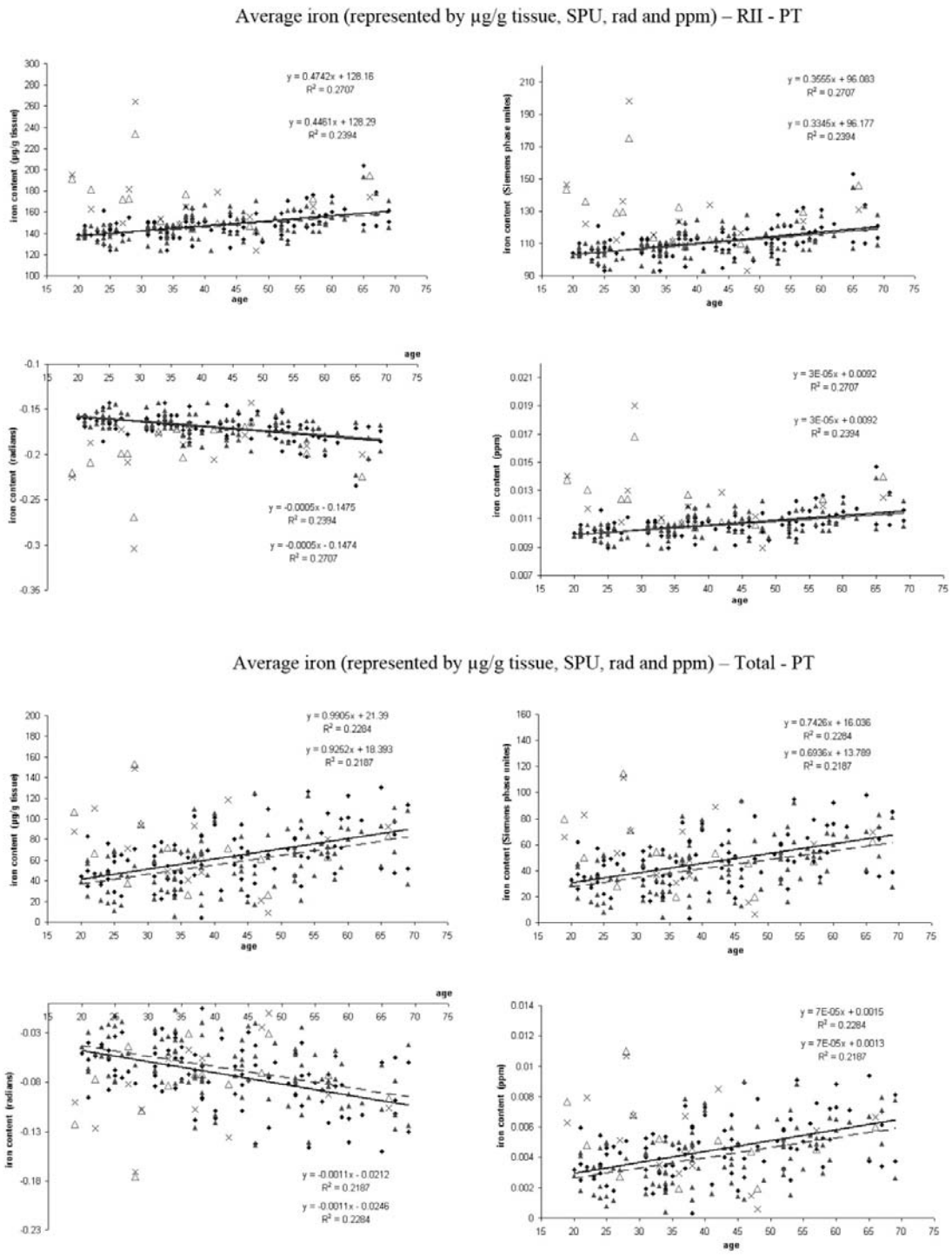

Figure 4.15: Expressing average iron content (iron density) in the PT for RII and the whole region with different units: µg Fe/g tissue, Siemens phase units (SPU), radians and ppm. The solid triangles and squires are for the left and right side PUT for normal subjects. The dashed line and solid line are the fits of the left and right PUT for normal subjects.

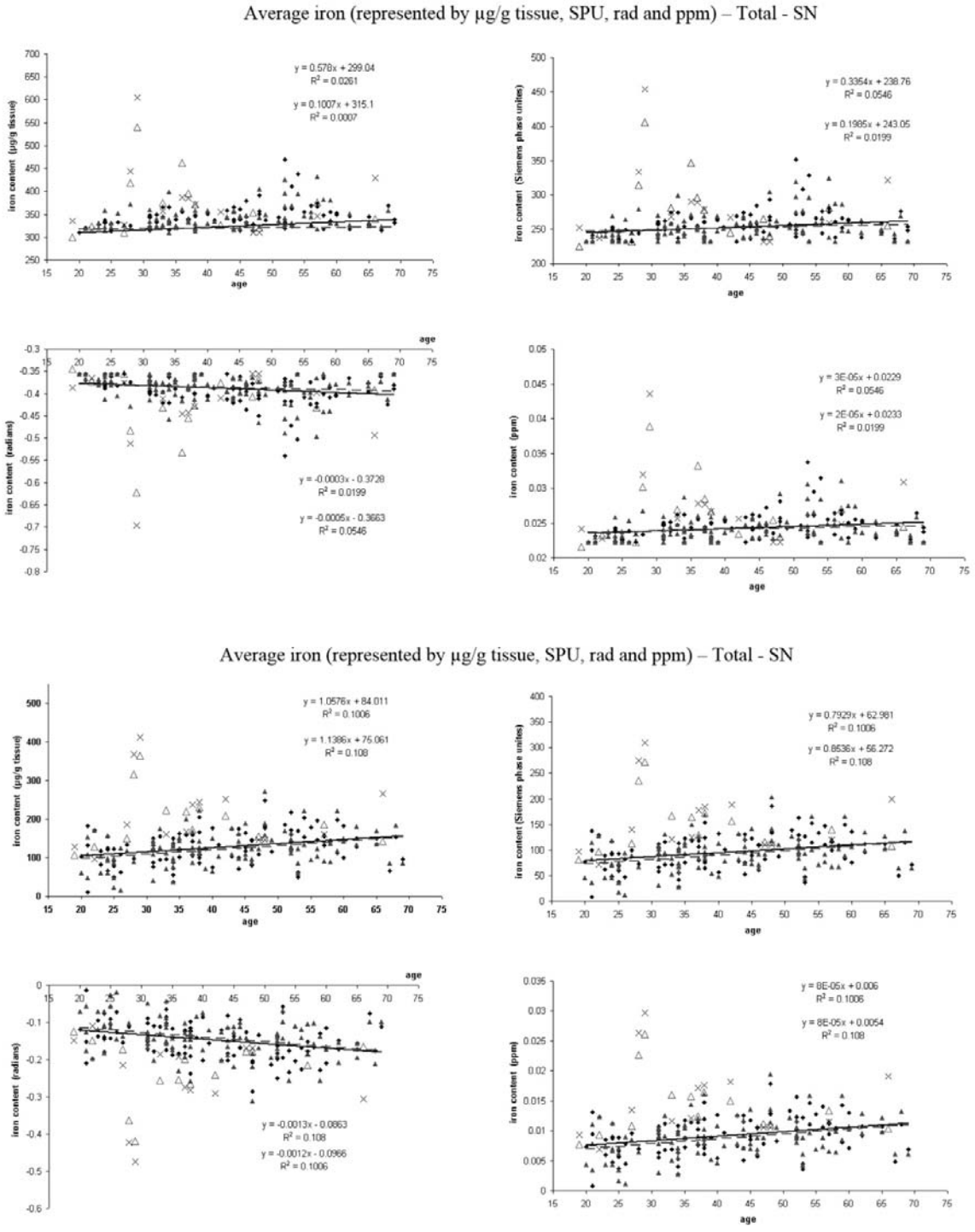

Figure 4.16: Expressing average iron content (iron density) in the SN for RII and the whole region with different units: µg Fe/g tissue, Siemens phase units (SPU), radians and ppm. The solid triangles and squires are for the left and right side PUT for normal subjects. The dashed line and solid line are the fits of the left and right PUT for normal subjects.

Table 4.4: Comparison between the two hemispheres of phase related iron measures

	Iron-Phase-RII				Average iron-Phase-RII				Iron-Phase-Total				Average iron-Phase-Total				Area-Phase-RII			
	Mean ($rad \times mm^3$)	SD	Number of L>R, L=R, L<R	P value	Mean (10^{-3} rad)	SD	Number of L>R, L=R, L<R	P value	Mean ($rad \times mm^3$)	SD	Number of L>R, L=R, L<R	P value	Mean (10^{-3} rad)	SD	Number of L>R, L=R, L<R	P value	Mean (10^{-3}%)	SD	Number of L>R, L=R, L<R	P value
PUT	-3.18	19.14	40/14/46	0.09	2.11	44.43	49/16/35	0.64	-2.59	27.25	44/0/56	0.33	0.76	20.12	50/0/50	0.70	-0.77%	4.98%	41/14/45	0.12
CN	3.54	13.71	61/0/39	0.01	0.66	26.39	51/0/49	0.8	7.28	14.84	70/0/30	<0.01	7.19	19.26	59/5/36	<0.01	1.28%	6.56%	60/0/40	0.05
GP	0.87	26.76	54/0/46	0.75	-5.68	52.52	47/6/47	0.29	4.81	26.24	58/0/42	0.07	4.83	26.78	57/3/40	0.07	0.68%	5.99%	55/0/45	0.26
RN	1.13	3.19	60/18/22	<0.01	6.58	19.34	51/22/27	<0.01	0.73	5.18	55/0/45	0.16	5.56	25.95	59/1/40	0.03	1.67%	4.86%	56/20/24	<0.01
PT	-1.36	4.34	34/0/66	<0.01	-1.20	10.57	42/3/55	0.27	-1.06	5.90	40/0/60	0.08	-6.58	15.56	31/3/66	<0.01	-2.68%	6.60%	35/0/65	<0.01
SN	-0.89	5.76	35/10/55	0.12	-2.54	28.24	37/13/50	0.32	-3.24	10.13	40/0/60	<0.01	-6.21	33.18	45/1/54	0.07	-0.49%	3.82%	36/10/54	0.19
THA	0.65	12.20	53/0/47	0.61	0.13	6.76	40/8/52	0.86	-0.72	14.40	48/0/52	0.63	-0.44	7.06	39/8/53	0.55	-0.17%	4.04%	46/0/54	0.68

PUT: Putamen. CN: Caudate Nucleus. GP: Globus Pallidus. RN: Red Nucleus. PT: Pulvinar Thalamus. SN: Substantia Nigra. THA: Thalamus

Mean: mean of the two hemispheres difference from left minus right hand side.

SD: standard deviation.

L>R: the amount of patients that show larger value in the left hemisphere. L=R: the amount of patients that show equal values in both hemispheres. L<R: the amount of patients that show larger value in the right hemisphere.

Table 4.5: Comparison between the two hemispheres of magnitude related iron measures

	Iron-Magnitude-RII				Average iron-Magnitude-RII				Iron-Magnitude-Total				Average iron-Magnitude-Total			
	Mean ($sec^{-1} \times mm^3$)	SD	Number of L>R, L=R, L<R	P value	Mean ($10^{-3} ms^{-1}$)	SD	Number of L>R, L=R, L<R	P value	Mean ($sec^{-1} \times mm^3$)	SD	Number of L>R, L=R, L<R	P value	Mean ($10^{-3} ms^{-1}$)	SD	Number of L>R, L=R, L<R	P value
PUT	0.42	1.02	70/0/30	<0.01	0.07	0.68	50/14/36	0.3	0.51	1.23	70/0/30	<0.01	0.65	0.83	76/7/17	<0.01
CN	0.46	0.82	80/2/18	<0.01	0.17	0.48	55/20/25	<0.01	0.66	0.80	85/100	<0.01	0.81	0.93	83/100	<0.01
GP	0.29	1.13	60/5/35	0.01	0.04	1.60	51/16/33	0.81	0.57	1.41	70/0/30	<0.01	0.55	1.20	66/5/29	<0.01
RN	0.02	0.25	58/3/39	0.43	0.11	0.62	49/21/30	0.08	0.00	0.21	54/0/46	0.97	0.17	1.01	59/7/34	0.09
PT	0.04	0.30	47/4/49	0.23	-0.03	0.53	41/17/42	0.6	0.05	0.36	55/0/45	0.17	-0.03	0.79	44/9/47	0.76
SN	0.08	0.31	55/0/45	<0.01	0.18	0.83	48/19/33	0.03	0.20	0.54	68/0/32	<0.01	0.67	1.53	62/10/28	<0.01
THA	0.20	1.47	50/0/50	0.08	0.06	0.45	43/28/29	0.12	0.20	1.30	52/0/48	0.13	0.07	0.57	43/13/44	0.3

PUT: Putamen. CN: Caudate Nucleus. GP: Globus Pallidus. RN: Red Nucleus. PT: Pulvinar Thalamus. SN: Substantia Nigra. THA: Thalamus

Mean: mean of the two hemispheres difference from left minus right hand side.

SD: standard deviation.

L>R: the amount of patients that show larger value in the left hemisphere. L=R: the amount of patients that show equal values in both hemispheres. L<R: the amount of patients that show larger value in the right hemisphere.

This study has a number of limitations. First, besides iron, there are also some other elements that can contribute to phase changes such as calcium, magnesium, copper, and zinc. However, they would tend to reduce the effects of iron. Also, we cannot separate these effects from those of iron especially if these other elements are randomly mixed with the iron. Second, since there was only a single gradient echo acquired, it was not possible to calculate an R2* map or to create directly a $\Delta R2^*$ map. Therefore, we had to assume that we could use the original signal from a younger population as a means to normalize the data and create an effective $\Delta R2^*$ map. These variations might account for some of the spread of $\Delta R2^*$ as a function of age. Although this appears to have worked reasonably well, there can be problems associated with confounding factors such rf coil loading, T1 values, and water content from person to person. Third, the limitation on drawing further conclusions regarding the effects of iron changes with age comes from the fact that the age range was only from 20 to 69 years. Including younger and older subjects would have been of interest as well.

Chapter Five Assessing the changes of susceptibility in the human brain nuclei over lifespan and investigating the correlation between susceptibility and in vivo iron content

Introduction

Iron is the most abundant transition metal in the brain, and plays a key role in a number of brain cellular processes including oxygen transport, electron transfer, neurotransmitter synthesis, myelin production and mitochondrial function [2, 38]. However, the useful redox cycling between ferrous (Fe^{2+}) and ferric (Fe^{3+}) iron can also make iron toxic when it is not safely bound in ferritin, because free or poorly liganded Fe(II) can react with H_2O_2 to generate highly reactive hydroxyl ions [96]. Both conditions of iron overload and iron deficiency (Hare et al., 2013) are associated with human brain diseases. Elevated iron is often a feature of neurodegenerative diseases such as multiple sclerosis (MS) [97], Alzheimer's disease [98], Parkinson's disease [99], Huntington's disease [100], and ferritinopathies [101]. Histological *in vitro* analysis has demonstrated iron accumulation rates in different gray matter (GM) structures are different throughout an individual's lifetime [7]. To further elucidate the involvement of iron in neurodegenerative disorders, a robust *in vivo* quantitative non-invasive assessment of normal brain iron deposition over time is essential. In this paper, we will attempt to provide such a baseline that can be used to differentiate normal from abnormal iron levels in patients with potential increases in iron content.

A variety of magnetic resonance imaging (MRI) methods have been used to quantify brain iron including FDRI (field-dependent relaxation rate increase), R2, R2*, phase and quantitative susceptibility mapping (QSM) [6, 55, 67, 82]. FDRI is a specific indicator for iron content, but it

yields nosier data, longer scan times and lower spatial resolution. Although R2 has a linear correlation with iron concentration [55], parameters generated from gradient echo sequences (GRE) are more sensitive to the local susceptibility induced magnetic field inhomogeneity caused by the presence of iron [102]. Magnetic susceptibility differences in brain tissues can come from a variety of sources such as paramagnetic ferritin iron, blood, diamagnetic myelin content, chemical exchange and fiber orientation [103]. Since the amount of myelin content is negligible, it is currently assumed that the magnetic susceptibility of gray matter is dominated by ferritin iron [7]. R2* has been shown to be a sensitive MRI parameter to estimate iron content in deep gray matter [55]. However, besides iron, R2* is also affected by water content. For example, in edema, signal from iron will be canceled out due to water's low R2* property. Also R2* increases proportionally to the concentration of myelin. In contrast, iron and myelin content manifest in opposite phase (field) behavior because the former is paramagnetic while the latter is diamagnetic. This makes gray-white matter (GM-WM) contrast in phase and QSM superior than that in R2*.

Phase has been used to represent iron content in the past [6, 90]. However, phase mapping suffers from non-locality of the magnetic field distribution, so it does not provide accurate local anatomical information [104]. This makes the estimation of iron content in 3D structures impossible using phase images. In the last few years, QSM has been introduced to overcome the non-local effects of phase and to provide the susceptibility maps [35, 105-107]. QSM is a post-processing method which reconstructs source images directly from the phase images [33, 34]. Both *post mortem* [67, 108] and *in vivo* [82, 106, 107, 109] experiments have demonstrated strong correlations between magnetic susceptibility assessed by QSM and known iron concentrations of different structures in the brain [82]. However, the reported correlations were

not consistent between the *in vivo* and *in vitro* results, and these *in vivo* studies had limited sample size and age range.

To provide a measure of iron over a broad age range, we studied a group of 180 normal subjects *in vivo* ranging in age from 20 years old to 69 years old by measuring the 3D structural magnetic susceptibility of seven sub-cortical gray matter nuclei. Our goal is to produce a quantitative magnetic susceptibility baseline as a function of age for each structure. These values will be used to compare with the regional iron concentrations taken from the histochemical post mortem study published by Hallgren and Sourander [7] to establish an *in vivo* quantitative conversion factor between magnetic susceptibility and iron concentration.

Materials and Methods

Subjects

A total of 188 healthy subjects were enrolled and scanned at Dalian First Affiliated Hospital, China. They were recruited from university staff, students and their relatives. Exclusion criteria were history of neurological or psychiatric conditions, head trauma with loss of consciousness for more than 5 min, drug and alcohol abuse, and brain surgery. These participants did not show any focal parenchymal loss, infarction, resection, or large hyperintensities in their brain on T2-weighted images. Seven subjects were excluded because of motion during scans. Two subjects didn't have their age recorded. Another four subjects weren't included because certain interested gray matter nuclei were lost after QSM processing. By excluding those cases, we included 175 normal subjects in this study (age, 45.1±14.2 years; range, 20-69 years; 86 females, 89 males). A consent form approved by the hospital's research ethics committee was provided for all volunteers to read, understand, and sign.

MR imaging

MR imaging of the brain was performed using a 1.5-Tesla (T) MR scanner (HD, General Electric Co., Milwaukee, WI, USA) equipped with an eight-channel phased array head coil by using identical protocols. The imaging plane was oriented parallel to the anterior-posterior commissural (AC-PC) line. A three-dimensional gradient-echo sequence was applied to acquire images for QSM reconstruction. The imaging parameters included: TR/TE = 53 ms/40 ms, flip angle = 20°, slice thickness = 3 mm, bandwidth = 31.25 Hz/pixel, field-of-view (FOV) = 24 cm and matrix size (Nx x Ny) = 384 x 320, yielding an in-plane resolution of 0.60 mm by 0.75 mm. The total scan time was 6 minutes 28 seconds.

Image processing and Analysis

QSM images were reconstructed by using our in-house Matlab based toolbox SMART 2.0 (MRI Institute for Biomedical Research, Detroit, MI, USA). Four steps were applied to generate the resulting QSM images: : brain extraction (BET [110]), phase unwrapping (3D-SRNCP [111]), background field removal (SHARP [106]) and an iterative QSM approach [34, 35]. The magnitude images were used to extract the brain tissue. The original susceptibility maps were derived by the following equation (for a right handed system) [35]:

$$\chi(r) = FT^{-1}\left[\frac{1}{\frac{1}{3} - \frac{{k_z}^2}{{k_x}^2 + {k_y}^2 + {k_z}^2}} \times FT\left[\frac{\phi(r)}{-\gamma B_0 T_E}\right]\right]$$

where φ(r) is the phase distribution, T_E is the echo time, B_0 is the main magnetic field strength, γ is the gyromagnetic ratio for hydrogen protons, k_x, k_y and k_z are coordinates in k-space. The ill-posed nature from the denominator term, which is the Green's function, was overcome by an

iterative approach to obtain artifact free susceptibility maps [34]. An example resulting QSM image and images from intermediate processing steps are shown in Figure 5.1.

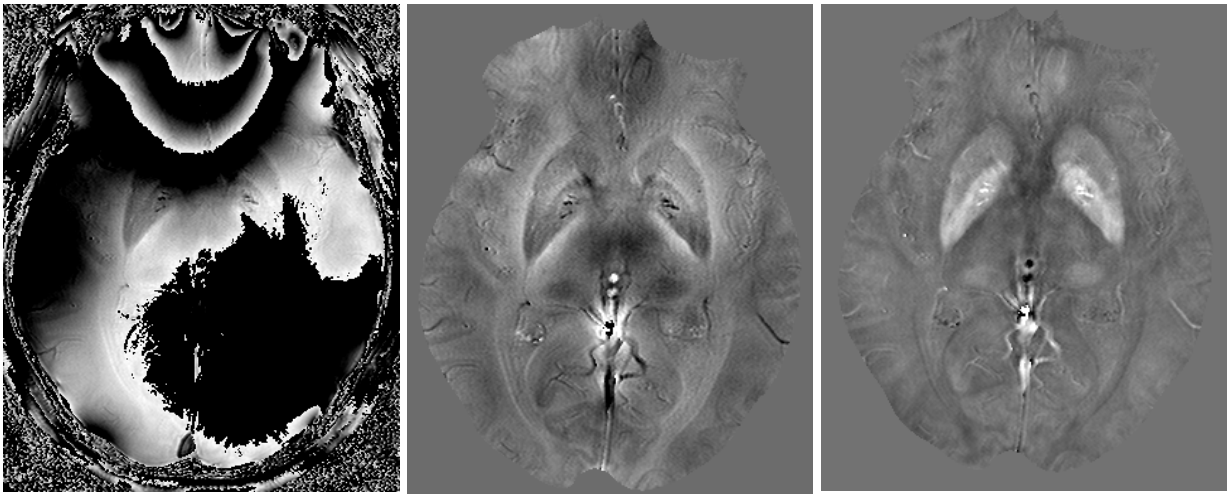

Figure 5.1: Left: Original phase image. **Middle:** Phase image after performing brain extraction, phase unwrapping and background removal. **Right:** Magnetic susceptibility map (iterative QSM map). The three images are the same slice from the same case. In the susceptibility map, bright signal intensities in the grey matter nuclei represent high magnetic susceptibility which relates to high iron content.

Magnetic susceptibility values are relative, therefore the susceptibility measurements need to be referenced to a particular region. The cerebrospinal fluid (CSF) is usually chosen as the reference region [62, 112]. However, due to the fact that the CSF shows a large range of susceptibility values [113], we quoted the values measured directly from the susceptibility maps in this study to avoid the errors caused by reference selection. If white matter dominates the signal then these will be susceptibility changes relative to white matter.

The susceptibility values in the regions of interest (ROIs) were assessed by segmenting these structures manually based on their anatomical features in the susceptibility maps. To evaluate the magnetic susceptibility of each nucleus in 3D, multiple slices were outlined to cover each entire structure (Figure 5.2). The 3D ROIs were traced and analyzed using an in-house developed

software SPIN (Signal Processing in NMR, MRI Institute for Biomedical Research, Detroit, MI, USA). The gray matter nuclei assessed in this study included: Caudate Nucleus (CN), Globus Pallidus (GP), Putamen (PUT), Thalamus (THA), Pulvinar Thalamus (PT), Red Nucleus (RN) and Substantia Nigra (SN). Large blood vessels and the dark rims around the structures were excluded when drawing the ROIs. Bilateral structures were traced on the same slices. The criteria for defining these structures are as follows:

CN: The head of the CN will be included. The most superior slide is the one first shows the head of CN. We omit the thin body part of CN because that part is vascularized, so it's hard to distinguish whether the signal is from veins or iron. Also which 3mm thickness, the susceptibility value of the thin body of CN is not trustable. The ROIs of the left and right CN were drawn on 6-7 continuous slices until the structure vanished into the sinus.

PUT: Five to six continuous slices were outlined. PUT starts one slice lower than the CN.

GP: GP starts from 1-2 slices lower than the PUT and usually presents on 4 to 5 continuous slices. It ends on the same level or one slice lower than the PUT. The slices with striations were avoided.

RN: The circular shaped RN appears on 2 continuous slices, which is easy to identify.

SN: The contours of the SN were delineated on 3 continuous slices, which included the same slices where the RN was drawn and the slice below RN.

THA: The THA was traced from inferior to superior. It starts from the 2nd slice above the SN and continues for 4 slices.

PT: The ROI for the pulvinar thalamus was drawn on the same slices as the THA.

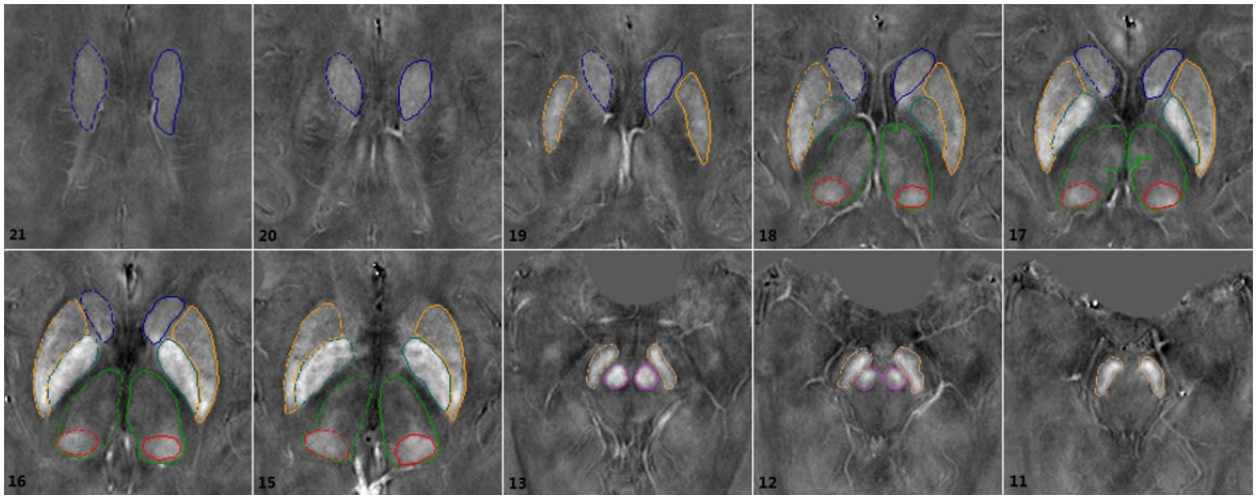

Figure 5.2. Multi-slice 3D ROIs drawn on the QSM maps. Structures include: CN: caudate nucleus (blue), GP: globus pallidus (green blue), PUT: putamen (orange), SN: substantia nigra (yellow orange), RN: red nucleus (violet), PT: pulvinar thalamus (red), THA: thalamus (green). Numbers on the images are the slice number of the data set. Each data set contain 40 slices.

To correlate the magnetic susceptibility with the iron concentration reported by Hallgren & Sourander, the scatter plots of non-heam iron versus age in GP, PUT and THA were duplicated electronically from a scanned version of Hallgren & Sourander's paper by using WebPlotDigitizer v2.6 (developed by Ankit Rohatgi). The reason to duplicate their data was to match the subject age range when doing the comparisons.

Statistical analysis

The statistical analysis was performed using Microsoft Excel 2013 and Matlab R2012a (Mathworks, Natick, MA). A p value of less than 0.05 was considered to be significant. The susceptibility differences between left and right hemispheres in different structures of interest were tested by paired t tests. Pearson correlation analysis was applied to investigate the relation between susceptibility and age in each structure. A Pearson correlation coefficient larger than 0.5 was considered to be a strong relationship. Linear regression models were used to fit the data. In

some structures, the susceptibility variance is not always homogeneous across age. The normal subjects were separate into 5 groups on the basis of their age (each decade as a group). The susceptibility means and standard deviations (SDs) were calculated.

To study the relationship between magnetic susceptibility and iron concentration, two methods were used in our study. First, the iron concentrations published by Hallgren & Sourander in scatter plots (GP, PUT and THA) were grouped into 5 bins (each decade as a group for subjects from 21 to 70 years old) as we did for the susceptibility data. With those averages from matched age groups, linear regression models were used to test the correlation between the iron concentrations assessed with postmortem samples and the magnetic susceptibility. Another method was by estimating the iron concentration in the PUT for each subject on the basis of age by using the equation published in Hallgren & Sourander's paper because the PUT shows the best age dependency, and then linear regression was used to find the correlation between susceptibility and the calculated iron concentration.

Results

Difference between two hemispheres and comparison between different gray matter nuclei

According to the paired t-tests, significant differences between the left and right hemispheres were found in SN and THA for all the 5 decades. For other gray matter nuclei studied in this paper, several age bins showed statistically differences ($p<0.05$). Table 5.1 shows the detailed statistics of the hemisphere comparisons. The average magnetic susceptibility values of different decades in the gray matter nuclei are as shown in Figure 5.3. The mean values and the SDs plotted in Figure 5.3 were calculated by including all the left and right hand side measurements.

Overall, the GP had the highest susceptibility, followed in decreasing iron content by the SN, RN, PUT, CN, PT and THA.

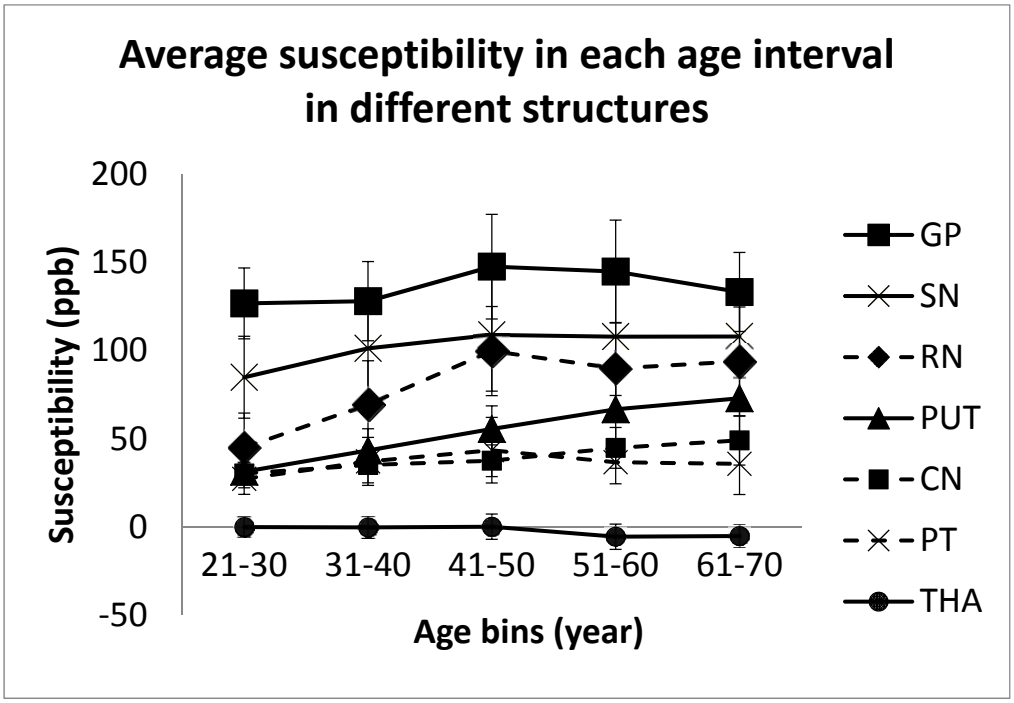

Figure 5.3: The average susceptibility for each of the 5 age intervals in different iron rich grey matter nuclei. The error bars represent plus/minus 2xSD. Values were calculated by including both of the left and right hemispheres. CN: caudate nucleus. GP: globus pallidus. PUT: putamen. SN: substantia nigra. RN: red nucleus. PT: pulvinar thalamus. THA: thalamus.

Table 5.1. Statistics table of the susceptibility comparisons between the left and right hemispheres in difference intervals.

Decade		CN	GP	PUT	SN	RN	PT	THA
	Left (ppb)	29.69±5.97	129.34±21.47	30.91±8.87	90.08±24.74	46.34±20.01	29.51±8.16	3.19±4.87
21-30 yr	**Right (ppb)**	31.09±7.06	124.42±18.57	31.90±9.38	79.91±20.84	43.90±19.42	25.25±9.02	-3.14±4.79
	p	0.1532	0.0085	0.3358	0.0000	0.0445	0.0009	0.0000
	Left (ppb)	35.37±10.37	129.03±23.60	42.76±12.65	107.85±27.45	70.40±25.60	38.83±13.84	2.38±5.72
31-40 yr	**Right (ppb)**	35.17±10.00	127.21±21.05	44.21±11.99	94.81±24.67	68.63±24.36	35.70±13.38	-3.09±5.58
	p	0.901563	0.3228	0.1402	0.0000	0.3844	0.0040	0.0000
	Left (ppb)	35.73±9.72	147.66±29.20	54.89±12.67	113.5±32.16	99.99±22.40	43.37±18.14	2.9±6.61
41-50 yr	**Right (ppb)**	39.59±7.83	147.71±30.61	56.44±13.70	104.45±31.47	99.70±28.23	43.82±19.32	-2.41±7.23
	p	0.0090	0.9816	0.3084	0.0013	0.9126	0.8014	0.0002
	Left (ppb)	41.77±10.49	143.62±29.83	63.82±17.40	114.01±32.81	94.67±26.02	39.39±12.42	-2.35±5.92
51-60 yr	**Right (ppb)**	48.12±11.86	146.23±28.75	69.75±19.19	101.93±33.09	85.36±25.42	34.19±11.58	-8.48±5.44
	p	0.0002	0.2753	0.0000	0.0000	0.0000	0.0001	0.0000
	Left (ppb)	49.27±13.32	133.56±23.92	75.43±24.28	114.32±21.99	96.28±34.03	37.43±15.13	-1.97±6.66
61-70 yr	**Right (ppb)**	49.13±14.83	133.07±21.20	70.72±22.22	101.84±22.69	91.50±27.88	34.39±19.44	-8.07±7.89
	p	0.943329	0.854003	0.0039	0.0000	0.1113	0.1186	0.0006

Susceptibility values were quoted as Mean ± Standard deviation for each decade. Left: left hemisphere. Right: right hemisphere. *p*: p value of the paired t tests. CN: caudate nucleus. GP: globus pallidus. PUT: putamen. SN: substantia nigra. RN: red nucleus. PT: pulvinar thalamus. THA: thalamus.

Linear relationship between susceptibility and age in iron rich deep gray matter nuclei

Figure 5.4 shows the susceptibility changes as a function of age in the gray matter nuclei analyzed in this study. Except for the SN and THA, all other nuclei including the CN, GP, PUT, RN and PT are plotted by combining the values from both hemispheres. The measurements of the right SN and right THA are presented in Figure 5.4 because all 5 decades show statistical difference between the two hemispheres in those two structures. The slopes and intercepts of the fitted linear equations are summarized in Table 5.2. The Pearson correlation coefficients for each relation are also listed in Table 5.2.

Table 5.2: The parameters of the linear fitting equations for Susceptibility vs. Age

		$\chi = A \times age + B$		
		A (ppb/year)	**B (ppb)**	**Pearson's Correlation Coefficient**
CN	Left	0.44±0.05	18.20±2.54	0.53±0.06
	Right	0.50±0.06	18.24±2.65	0.56±0.06
	Both	0.47±0.04	18.23±1.84	0.54±0.05
GP	Left	0.24±0.14	126.10±6.76	0.13±0.08
	Right	0.38±0.14	118.99±6.55	0.20±0.07
	Both	0.26±0.08	122.45±3.92	0.17±0.05
PUT	Left	1.01±0.08	7.18±3.74	0.70±0.05
	Right	1.14±0.08	3.94±3.95	0.72±0.05
	Both	1.08±0.06	5.56±2.73	0.71±0.04
SN	Left	0.52±0.16	84.71±7.34	0.25±0.08

	Right	0.47±0.15	75.31±7.07	0.24±0.08
	Both	0.50±0.11	80.01±5.18	0.24±0.05
RN	Left	1.25±0.15	25.11±6.91	0.55±0.06
	Right	1.12±0.15	26.90±6.88	0.51±0.07
	Both	1.19±0.10	26.00±4.88	0.53±0.05
PT	Left	0.19±0.08	29.56±3.58	0.18±0.07
	Right	0.18±0.08	26.67±3.92	0.16±008
	Both	0.18±0.06	28.11±2.66	0.17±0.05
THA	Left	-0.15±0.03	7.42±1.53	-0.33±0.07
	Right	-0.16±0.03	2.31±1.57	-0.35±0.07
	Both	-0.16±0.03	4.90±1.21	-0.31±0.05
RN (20-50 yr)	Both	2.42±0.17	-13.84±6.31	0.70±0.05
SN (20-50 yr)	Right	0.98±0.28	58.80±10.27	0.33±0.10
PT (20-50 yr)	Both	0.72±0.11	10.61±3.88	0.43±0.06

Left: left hemisphere. Right: right hemisphere. Both: left and right hemisphere together. For RN, SN and PT, data are also fitted for subjects between 20 and 50 years old.

In the PUT, CN and RN, the magnetic susceptibility appears to be linearly correlated with age ($R>0.5$, $p<0.05$). The susceptibility distributions across ages are quite scattered in the GP, SN, PT and THA with limited age dependency ($R<0.3$). According to the slopes, the susceptibility of the RN shows the most rapid increase as a function of age with a changing rate of 1.19±0.10 ppb/year, and then followed by the PUT (1.08±0.06 ppb/year), SN (0.50±0.11 ppb/year), CN

(0.47±0.04 ppb/year), GP (0.26±0.08 ppb/year) and PT (0.18±0.06 ppb/year). The THA shows decreased susceptibility with age and with 0.16±0.03 ppb/year. Overall, it appears as if the susceptibility values increase with an almost constant rate till around 50 years old and then level off. By only fitting the data between 20 to 50 years, we found steeper slopes and better correlations as shown in Table 5.2. Fittings of the data between 20 to 50 years for the RN and SN are shown in Figure 5.4.

Correlation between susceptibility and iron concentration

For the data extracted from the scatter plots in Hallgren & Sourander's paper, after excluding the subjects younger than 20 years old and older than 70 years old, 47 subjects remained with an age of 43.6 ± 14.2 years old. There is no age difference between our normal controls and those 47 subjects. Figure 5.5 shows the correlation between susceptibility measured by MRI *in vivo* and iron concentration. The correlation slope is determined by linear regression. Two approaches served to predict iron concentration as explained in the Methods section. By using the group average approach (Figure 5.5 Left), we found $\chi = 0.89(\pm 0.03) * \mathrm{Fe} - 48.51(\pm 4.09)$. By using the equation based approach (Figure 5.5 Right), we found $\chi = 0.93(\pm 0.05) * \mathrm{Fe} - 59.49(\pm 6.43)$. The correlation slopes investigated by the two methods are very close. The method we applied for reconstructing susceptibility maps need to be corrected by a factor of 1.16 [67]. After correcting for this underestimate, the correlation slopes become 1.03±0.03 ppb per μg iron/g wet tissue and 1.08±0.06 ppb per μg iron/g wet tissue for the two approaches, respectively.

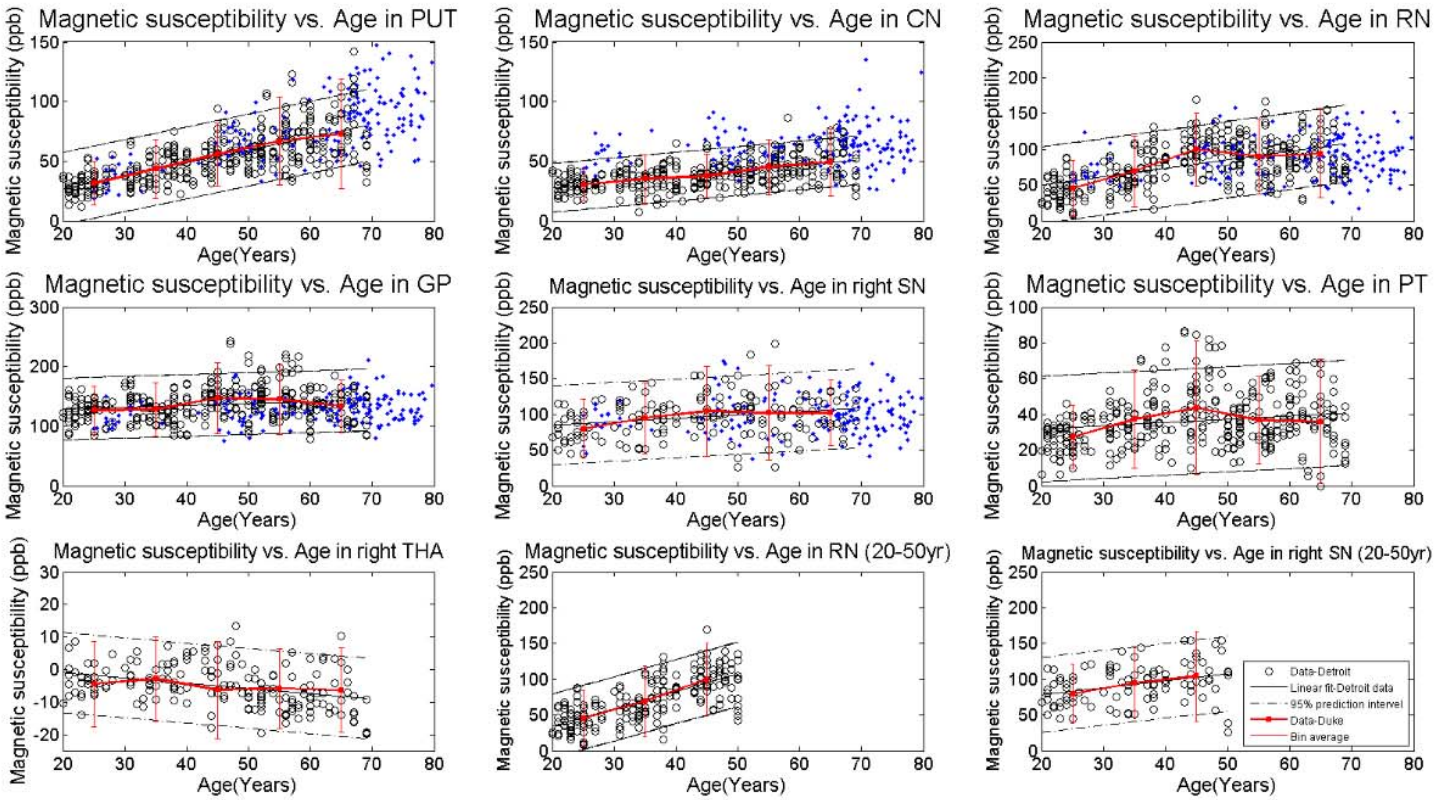

Figure 5.4: Magnetic susceptibility changes with age in different grey matter nuclei. The susceptibility values reported in this study are highly consistent with Li *et al.*'s study [77]. Strong positive linear correlations are found in PUT, CN and RN. Mild positive linear correlations are shown in GP, SN and PT and good negative linear correlation in THA. In RN, SN and PT, the linear correlations are better if only looking at the data between 20 to 50 years old. PUT: putamen. CN: caudate nucleus. RN: red nucleus. GP: globus pallidus. SN: substantia nigra. PT: pulvinar thalamus. THA: thalamus. Black circles: current study data. Blue dots: values published by Li *et al.* from Duck University. Black line: linear regression fitting for the current study data. Red squares: average susceptibility of each decade for current study. Vertical error bars: two standard deviations.

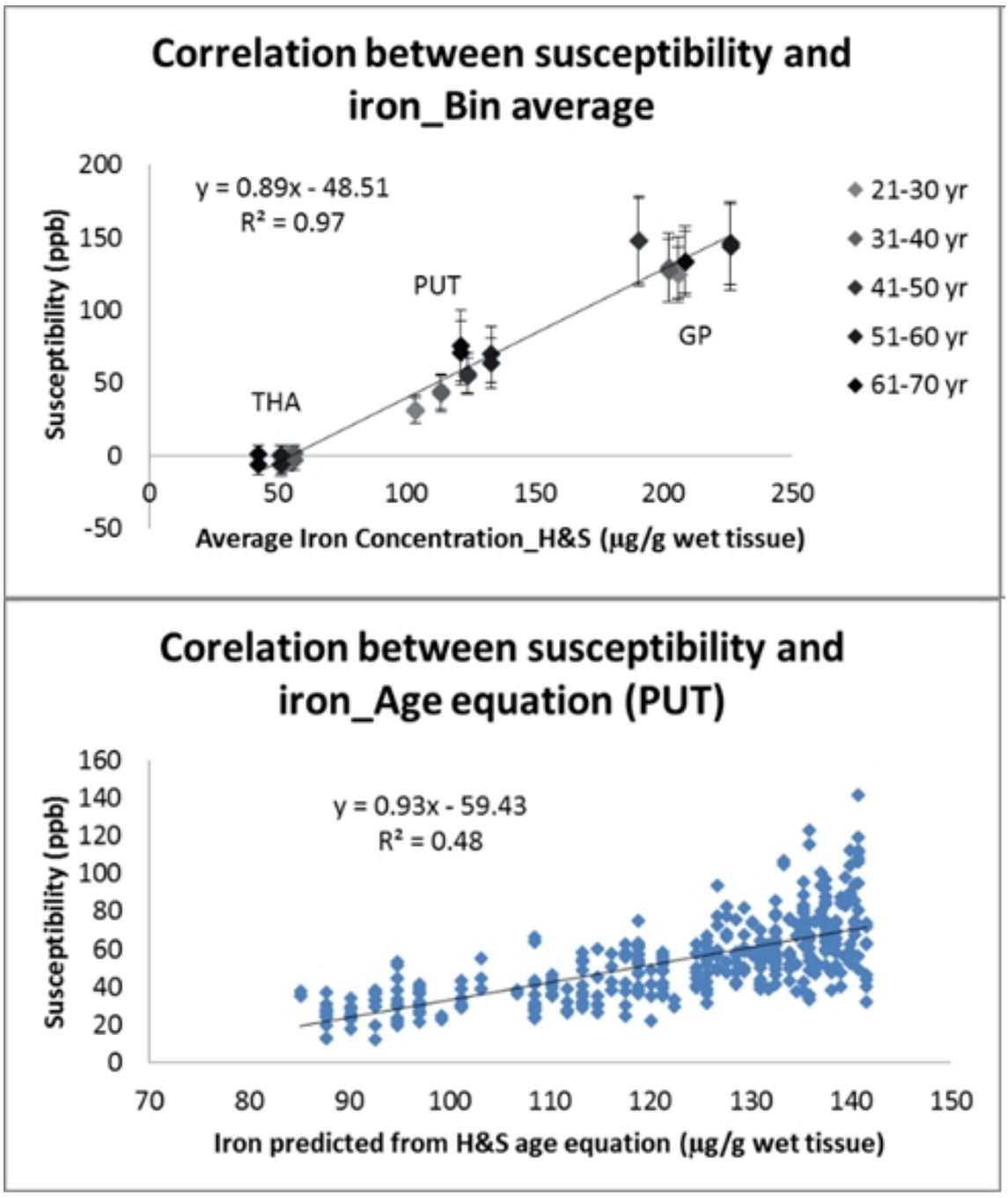

Figure 5.5: Relationship between magnetic susceptibility and iron concentration determined with linear regressions. **Upper:** It is estimated by correlating the bin averages of susceptibility with matched bin averages of iron concentrations extracted from Hallgren & Sourander's scatter plots. The structures included in this plot are GP, PUT and THA because Hallgren & Sourander only provided the scatter plots of those three structures which we also analyzed in our study. **Lower:** It is estimated by correlating susceptibility with iron concentration calculated from iron-age equation [7] in PUT, which shows the best age dependency. The correlations found with the two methods are similar.

Discussion

Linear correlations between magnetic susceptibility and age were revealed in almost all the gray matter nuclei studied in this manuscript (Figure 5.4). Some were strong such as in PUT, CN, RN and THA, and some were weak such as in GP, SN, and PT. The strength of the correlation also depended on what age range was used. Brain gray matter nuclei iron quantification with age has been investigated with a number of methods such as R2* [61, 92, 114], phase [6, 66], and histopathology [7]. Since our data included normal subjects from 20 to 70 years old, we examined the susceptibility by comparing the same age range with other studies. R2* studies by Aquino *et al.* (for PUT, CN, GP and SN) [92] and Li *et al.* (for PUT, CN, GP, SN and RN) [77] reported exponential growth in R2* with age, which is consistent with the cadaveric study by Hallgren & Sourander. However, after eliminating the young subjects (younger than 20 years old) in those three studies, all correlations turn linear. The linear correlation between phase and age is also found in some previous publications [6, 66]. The best linear age dependency is shown in the PUT [6, 7, 61, 66, 77, 92, 114] and sometimes in the CN [6, 61, 77, 114] with R2*/phase/iron growing well into the 80s. This is consistent with our susceptibility trends. Linear regression curves in the GP [6, 7, 77, 92] and SN [6, 77, 92] are flat for R2*/phase/iron for subjects with ages of 20 years and up; this is consistent with our findings. A detailed comparison between studies is shown in Table 5.3.

Table 5.3: Reported linear correlation between iron related parameters and age.

Structures	Authors/Method	Linear correlation (20 yr and up)	Field (Tesla)	Subject age range	Sample size
PUT	**Susceptibility**/This study	Strong	1.5	20-69	175
	R2*/Aquino et al. (2009)	Strong	1.5	1-80	80
	R2*/Cherubini et al. (2009)	Strong	3	20-70	100
	R2*/Peran et al. (2009)	Strong	3	20-41	30
	Δ**R2***/Haacke et al. (2010)	Strong	1.5	20-69	100
	R2*/Li et al. (2013)	Strong	3	7-83	174
	Phase/Xu et al. (2008)	Strong	1.5	22-78	78
	Phase/Haacke et al. (2010)	Strong	1.5	20-69	100
	Susceptibility/Li et al(2013)	Strong	3	1-83	181
	Cadaveric/Hallgren& Sourander (1958)	Strong			81
CN	**Susceptibility**/This study	Strong	1.5	20-69	175
	R2*/Aquino et al. (2009)	Weak	1.5	1-80	80
	R2*/Cherubini et al. (2009)	Good	3	20-70	100
	R2*/Peran et al. (2009)	Strong	3	20-41	30
	Δ**R2***/Haacke et al. (2010)	Strong	1.5	20-69	100
	R2*/Li et al. (2013)	Strong	3	7-83	174
	Phase/Xu et al. (2008)	Weak	1.5	22-78	78
	Phase/Haacke et al. (2010)	Good	1.5	20-69	100
	Susceptibility/Li et al(2013)	Weak	3	1-83	181

RN	**Susceptibility**/This study	Strong	1.5	20-69	175
	Δ**R2***/Haacke et al. (2010)	Strong	1.5	20-69	100
	R2*/Li et al. (2013)	Weak	3	7-83	174
	Phase/Xu et al. (2008)	Weak	1.5	22-78	78
	Phase/Haacke et al. (2010)	Strong	1.5	20-69	100
	Susceptibility/Li et al(2013)	No	3	1-83	181
GP	**Susceptibility**/This study	No	1.5	20-69	175
	R2*/Aquino et al. (2009)	Weak	1.5	1-80	80
	R2*/Peran et al. (2009)	No	3	20-41	30
	Δ**R2***/Haacke et al. (2010)	Good	1.5	20-69	100
	R2*/Li et al. (2013)	Weak	3	7-83	174
	Phase/Xu et al. (2008)	Weak	1.5	22-78	78
	Phase/Haacke et al. (2010)	No	1.5	20-69	100
	Susceptibility/Li et al(2013)	Weak	3	1-83	181
	Cadaveric/Hallgren& Sourander (1958)	No			81
SN	**Susceptibility**/This study	Weak	1.5	20-69	175
	R2*/Aquino et al. (2009)	No	1.5	1-80	80
	Δ**R2***/Haacke et al. (2010)	Good	1.5	20-69	100
	R2*/Li et al. (2013)	No	3	7-83	174
	Phase/Xu et al. (2008)	No	1.5	22-78	78
	Phase/Haacke et al. (2010)	Good	1.5	20-69	100
	Susceptibility/Li et al(2013)	No	3	1-83	181

PT	**Susceptibility**/This study	No	1.5	20-69	175
	Δ**R2***/Haacke et al. (2010)	Strong	1.5	20-69	100
	Phase/Haacke et al. (2010)	Good	1.5	20-69	100
THA	**Susceptibility**/This study	Week	1.5	20-69	175
	R2*/Cherubini et al. (2009)	No	3	20-70	100
	R2*/Peran et al. (2009)	No	3	20-41	30
	Δ**R2***/Haacke et al. (2010)	Strong	1.5	20-69	100
	Phase/Xu et al. (2008)	No	1.5	22-78	78
	Phase/Haacke et al. (2010)	Week	1.5	20-69	100
	Cadaveric/Hallgren& Sourander (1958)	Good Negative			81

Strong: R>0.5; Good: 0.3<R<0.5; Weak: 0.2<R<0.3; No: R<0.2.
R is the correlation coefficient.

To examine the stability and consistency characteristics of susceptibility mapping, we plotted the susceptibility measurements from Li *et al.*'s study [77] on top of ours for subjects 20 years and older (Figure 5.4). The plots clearly show consistency between the two studies. Although our imaging parameters are different, it is encouraging to note that both approaches yield similar results. This suggests that comparisons across different QSM algorithms, different types of magnets and different centers is viable.

A negative relationship between the susceptibility with age was found in the thalamus in this study. This is consistent with what Hallgren & Sourander reported in their postmortem work. They claimed a rise in the iron content up to about 35 years old and then a decrease (although they had a limited number of cases between 20 to 30 years). This trend is consistent with Bilgic

et al.'s finding that the average susceptibility value in the thalamus was lower in the elderly relative to the young [82]. Another comment we would like to make here is that the measured susceptibility values are relative to that tissue which dominates the signal and established the main frequency in the MR experiment and in this case that is the white matter. If the iron content in the white matter goes up with age, then the downward trend we found here for the thalamus would tend to flatten out in reality. This requires further study.

The correlation between magnetic susceptibility and iron concentration found in this manuscript is 0.89±0.03 ppb/μg Fe/g wet tissue by the age bin method and 0.93±0.05 ppb/μg Fe/g wet tissue by the iron-age function method [7] in PUT. The two slopes are close to each other. After applying the correction factor (14%) due to the iterative QSM processing approach [67], the slopes become 1.03±0.03 (0.89 / (1-14%) = 1.03) and 1.08±0.06 (0.93 / (1-14%) = 1.08) ppb/μg Fe/g wet tissue, respectively. Those slopes are also very close to recent studies by Zheng *et al.* [67] and Langkammer *et al.* [108]. In their studies, the susceptibility-iron correlation was investigated by ferritin phantoms and cadaveric brains, and the iron concentrations were measured by inductively coupled plasma mass spectrometry (ICPMS) and X-ray fluorescence (XRF). The slopes reported were 1.11 ppb/μg Fe/g wet tissue (ferritin, ICPMS), 1.10 ppb/μg Fe/g wet tissue (ferritin, XRF), 0.93 ppb/μg Fe/g wet tissue (cadaveric, XRF) and 0.96 ppb/μg Fe/g wet tissue (cadaveric, ICPMS).

The consistency across sites in measuring iron with QSM suggests that this may be the best approach to do iron quantification both *in vivo* and *in vitro.* Although R2* has been shown to also correlate well with iron content, in either small or large amounts, it may not fare as well. For example, for 3T magnetic, Langkammer *et al.* [55] reported a correlation slope of 0.27Hz/μg iron/g wet tissue according to a postmortem study, while Peran *et al.* [61] and Yao *et al.* [62]

reported the slope as 0.1142Hz/μg iron/g wet tissue and 0.120Hz/μg iron/g wet tissue respectively with *in vivo* data. The differences slopes between studies may be caused by that R2* depends not only on iron content but also on the water content and tissue composition. In addition, R2* values will change as a function of field strength [62], while magnetic susceptibility will always yield the pristine susceptibility, at least in theory.

Comparing the susceptibility values with iron concentration published by Hallgren & Sourander is a popular approach to find the *in vivo* conversion factor. However, people always quote the average iron concentration calculated from all 81 subjects with the age range of 31 to 100 years for different gray matter nuclei [7]. This is not an appropriate way to find the correlation because the average susceptibility values they had were not calculated from the subjects with the same age distribution [106, 107, 109, 113] and the fact that iron deposition in gray matter nuclei changes throughout the lifespan. Also, the sample sizes in those studies were small, only a few cases were included. On the other hand, in this current manuscript, the average iron concentration for each decade was calculated on the basis of Hallgren & Sourander's scatter plots. With this method, the age distributions are matched and more data points are used for fitting (30 points), which ensures a more reliable conversion factor between the susceptibility and iron concentration.

Another method proposed in this study to find the susceptibility-iron correlation is by estimating the iron concentration from the age equations provided in Hallgren & Sourander's paper [7]. The disadvantage of this method is that there is no one to one match for each individual because the equation can only represent the mean iron concentration throughout the lifespan. Because of this we have to choose a structure which shows a strong age dependency. With the large sample size

of 175 and strong age dependent characteristic in PUT, a reasonable quantitative correlation between the magnetic susceptibility and iron content was seen.

Finally, we can make some comments about the potential susceptibility of the CSF thanks to the strong linear relationship of susceptibility with iron between tissues. The intercepts ($-48.51(\pm 4.09)$ and $-59.49(\pm 6.43)$ ppb) indicated by the linear fitting equations from the two approaches can be used as an estimate of the susceptibility of the CSF. Since CSF is pure water and doesn't contain iron, it can serve as a baseline for estimating absolute iron deposition in other brain structures. There are basically three regions that can be used to measure the CSF susceptibility from the QSM maps: the body of the lateral ventricle, the ventricle next to the CN and the CSF in the sulci in the upper brain. The body of the lateral ventricle contains choroid plexus, so finding consistent values there was difficult. Also due to the filter size chosen for SHARP processing is comparable to the sizes of gray matter nuclei and the body lateral ventricle is such a big structure, the susceptibility will be potentially modified. The size of the CSF in the sulcus is only a few pixels and sometimes veins pass through it.

Limitations

One of the limitations of this study is the lack of young subjects. However, by combining Li *et al.*'s recent study [77], promising susceptibility trends with age are revealed in gray matter nuclei.

Another limitation is the lack of multi-echo data, so we couldn't provide the comparison between magnetic susceptibility and regional R2* in this study. However, in Li *et al*.'s *in vivo* study [77], the correlation between R2* and susceptibility was suggested by a conversion slope of 0.1267Hz/ppb ($R2^* = 0.1267\chi$). As we have shown in Figure 5.4, our susceptibility

measurements are comparable with theirs, so the susceptibility we measured can be converted to R2* according to their calculations. In addition, Peran at al [61] published a correlation between R2* and iron concentration for *in vivo* data with a slope of 0.1142Hz/μg iron/g wet tissue. In Peran at el.'s work, iron concentrations were derived from published post-mortem data [7] in a function of age. By combining the two relations, we have $0.1267\chi = 0.1142 * \mathrm{Fe}$, then

$$\chi = 0.90 * \mathrm{Fe}$$

where shows by correlating our susceptibility measurements with R2* and then correlating with iron on the basis of published correlations, the susceptibility/iron correlation is 0.90 ppb/μg Fe/g wet tissue. This is very close to what we have found with our in vivo data: 0.89±0.03 ppb/μg Fe/g wet tissue by the age bin method and 0.93±0.05 ppb/μg Fe/g wet tissue by the iron-age function method (Hallgren and Sourander, 1958) in PUT.

Conclusion

The results of this study show that QSM is a reliable approach to do iron quantification and it is independent of imaging parameters. Iron is directly correlated with magnetic susceptibility, therefore, iron quantification can be done by QSM without the need for the postmortem iron study by Hallgren and Sourander anymore. The susceptibility-age correlations revealed from the 175 normal subjects studied here can serve as a basis for determining normal iron content as a function of age that can be used to help determine abnormal iron content levels in diseases that affect iron content in the brain.

Chapter Six Patterns of chronic venous insufficiency in the dural sinuses and extracranial draining veins and their relationship with white matter hyperintensities for patients with parkinson's disease

Introduction

Idiopathic Parkinson's disease (IPD) is the second most common neurodegenerative disease after Alzheimer's disease, and it affects roughly 0.1% to 0.3% of the population[14]. The main known risk factor is age. The etiology of IPD remains unknown. Generally, Parkinson's patients (PD) show a loss of dopaminergic neurons in the substantia nigra pars compacta, a reduction of dopamine levels in the striatum over time[115] and accumulation of intraneuronal inclusions called Lewy bodies and Lewy neurites[116]. Although clinically PD is a motor disorder and has a good response to dopaminergic therapy, in the advanced stages of PD most of the motor disability symptoms don't respond to dopaminergic therapy anymore[116]. There are also many non-motor problems, such as cognitive impairment, autonomic dysfunction, neuropsychiatric symptoms[117] and fatigue[118] for patients in both early and advanced stages. These findings suggest the dopaminergic system may not be the only system involved in the PD process.

It has been shown that there is an increased presence of white matter hyperintensity (WMH) in IPD patients[20]. The suggested causes for these deficits include ischemia and venous insufficiency from periventricular venular collagenosis[21-23]. WMH might cause or exacerbate motor or cognitive features of PD[119] especially in the presence of gray matter vascular lesions involving the substantia nigra or striatum[120], corticostriatal-thalamocortical loop disruption, damage to the interhemispheric connections of the corpus callosum[119], or disruption of the subcortical afferents . If typical late-onset PD patients have a history of minor stroke, ischemic

heart disease, or diabetes mellitus, they show more severe clinical features[121]. One group found that the severity of WMH at baseline was the best predictor of PD progression[24].

In the last few years, there has been an increasing interest in the role of veins in neurodegenerative diseases[12], and more attention has been paid to the extracranial veins such as the internal jugular veins (IJVs) and the azygous veins as being potential sources of venous hypertension[9, 11, 12]. Obstructed venous outflow in the extracranial veins was reported to correlate significantly with hypoperfusion in the brain parenchyma which could contribute to hypoxia and axonal damage[122, 123]. Additionally, venous hypertension in the dural sinuses inhibits the absorption of CSF through arachnoid villi. Some studies showed an association between the venous outflow disturbances with low net CSF flow in patients with MS[124, 125]. An important aspect of the venous abnormalities is that they are potentially treatable with percutaneous transluminal angioplasty (PTA)[126]. The first application of PTA in the major cerebral veins was done by Zamboni *et al* in 2009 in MS patients with CCSVI[127]. Since then, a few studies have shown improvement in neurological outcomes and/or some quality-of-life parameters in MS patients who underwent PTA[127-129].

The use of MR angiography (MRA) and phase contrast flow quantification (PCFQ) for the study of the vasculature in patients with PD is a novel concept spurred, in part, by our recent work in multiple sclerosis (MS) patients[13]. By applying flow encoding in the PC sequence, the intensity of the phase images is directly proportional to the speed[130]. The phase intensity in radians is then scaled to velocity using the relationship $v=\text{phase}(Venc/\pi)$, in which Venc stands for velocity encoding. By positioning these 2D PC-MRI flow slices roughly perpendicular to the vessels in the neck, flow in all major vessels can be quantified. Using these morphologic and

functional MRI techniques, we can not only obtain the anatomic vascular information but also the quantitative arterial and venous blood flow.

To this end, we proposed this preliminary study with a group of 23 IPD patients to see if some of these patients have abnormal structure or flow either intracranially and extracranially. The outcomes from this study have the potential to open new doors in studying the vascular etiology of IPD.

Methods

Recruitment of patients and controls

From May, 2011 to March, 2013, 40 IPD patients were recruited and scanned. Fifteen patients did not receive a complete set of scans due to motion or termination because of patient discomfort. Two IPD patients were excluded because they were scanned after taking medication. By excluding those cases, we finally included 23 IPD cases and for this reason 23 age-matched healthy subjects were included in this study. They were all recruited and imaged at Wuhan Union Hospital, China. The patients with clinically definite IPD were diagnosed by a neurologist at Wuhan Union Hospital based on the United Kingdom PD Society Brain Bank Criteria (UKPDSBB). The patients and controls were imaged under internal review board approved protocols.

Patients who fulfilled the UKPDSBB criteria were included. However, patients who had any of the following conditions were excluded from this study: any element of the exclusion criteria listed in UKPDSBB; patients with other neurological disorders such as Huntington's disease, multiple sclerosis, normal pressure hydrocephalus; drug-induced Parkinsonism; hypoxia; arteriosclerotic disease; hypertension or diabetes because excessive WMH may show in those

patients. The following conditions were excluded for normal controls: history of cardiovascular, neurological or psychiatric conditions; head trauma; hypertension; diabetes; drug or alcohol problems.

All patients and controls consented to be subjects in this study. A 3T Siemens scanner with a 16 channel head/neck coil arrangement was used for acquiring the data (Siemens TRIO). Patients underwent conventional clinical imaging as well as angiographic (arterial and venous) and flow quantification imaging. The imaging parameters for each sequence are listed in Table 6.1. The MRI images of the patients were acquired before taking medication.

Table 6.1: MR imaging parameters for different sequences.

	2D TOF-MRV	**T2-FLAIR (21 PD patients)**	**T2-FLAIR (2 PD patients, 23 normal controls)**	**SWI**	**PCFQ at C6/C7**
Orientation	Transverse	Transverse	Sagittal	Transverse	Transverse
TR (ms)	26	8500	6000	29	42.25
TE (ms)	5.02	93	396	20	4.13
Flip Angle	60°	130°	120°	15°	25°
Resolution (mm^3)	0.5x0.5x2.5	0.43x0.43x5	0.5x0.5x1	0.5x0.5x2	0.57x0.57x4
Bandwidth (Hz/pixel)	217	287	781	119	531

An arterial saturation band with a width of 40mm and a separation of 10mm from the excited slice was applied during 2D TOF-MRV acquisition. A maximum encoding velocity (VENC) of 50cm/sec was used for PCFQ.

Data processing and analysis

Data processing was done using our in-house software Signal Processing in Nuclear Magnetic Resonance (SPIN, Detroit, Michigan). WMH were evaluated from the 2D FLAIR images. The total volume of WMH was calculated semi-automatically by SPIN. As the FLAIR data were collected with different resolutions, all the data were normalized to $1x1x5mm^3$ (transverse in-plane) before doing the volume quantification. In addition, the MRI visual rating scale proposed

by Scheltens *et al.*[131] was also used for evaluating the WMH level, which takes the number, size and location of the WMH into account. The modified visual rating criteria are presented in Appendix 1. The 2D TOF data were used for evaluating the venous structures in the head and neck. A saturation band was applied to suppress the arterial flow in the 2D TOF images. The maximum intensity projection (MIP) of the whole series was generated in the coronal view from the 2D TOF coverage. The major veins of interest for the structural analysis included the transverse sinuses and the extracranial veins in the neck.

The PCFQ images were used to analyze the through-plane blood flow in the lower neck (C6/C7). Thirty time points were collected for each cardiac cycle. Cardiac gating was achieved using pulse triggering. Background muscle was used to monitor the baseline to ensure there was no bulk drift over time. We chose 50cm/sec as the Venc because this gave much better SNR for venous flow than 100cm/sec, and flow in the arteries could still be unwrapped when aliasing occurred, which was done automatically with SPIN. The vessels of interest included (Figure 6.1): the internal and external jugular veins (IJVs, EJVs), vertebral veins, deep cervical veins, common carotid arteries and vertebral arteries. The vessel lumen was segmented from the magnitude images (Figures 6.1A and 6.1C) semi-automatically thanks to the presence of sufficiently high contrast and copied onto the phase images (Figures 6.1B and 6.1D).

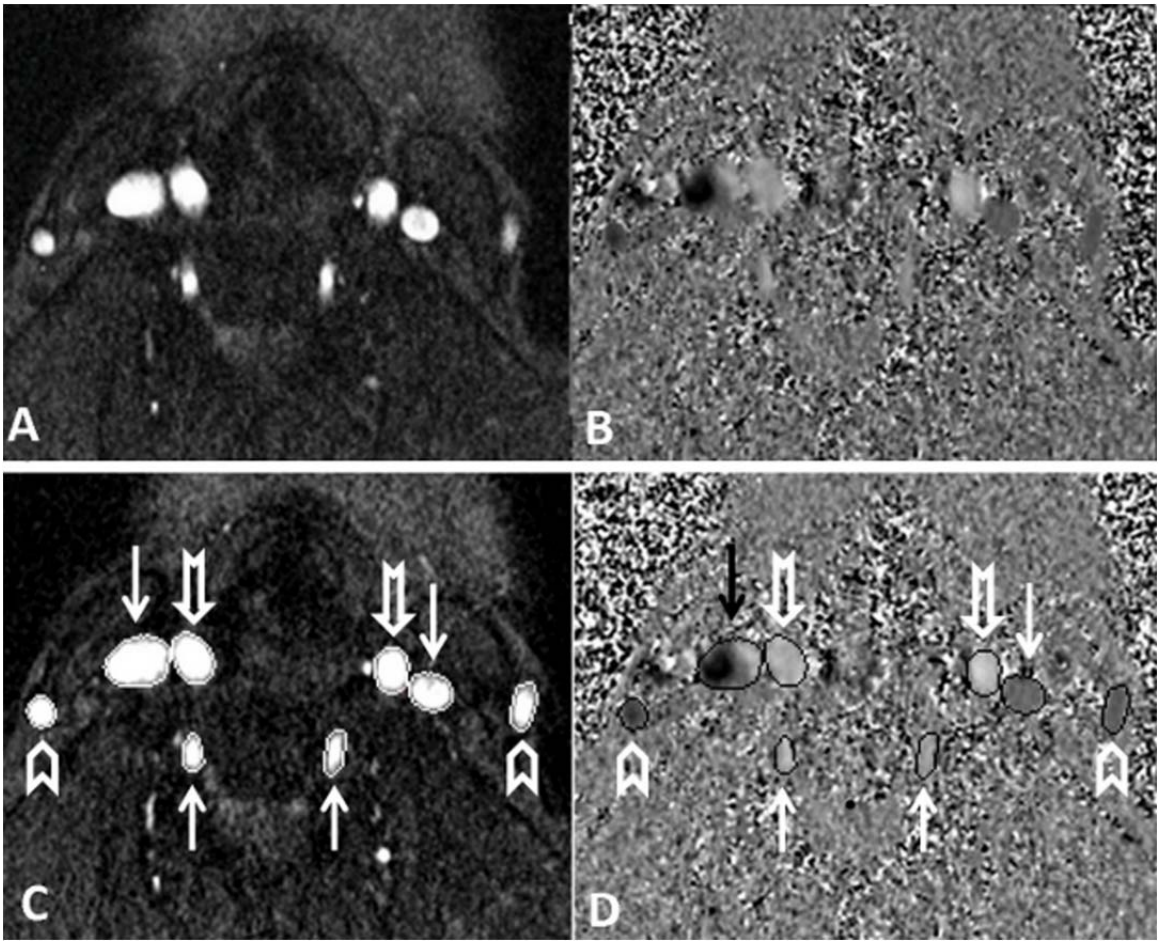

Figure 6.1: PCFQ images without (A, B) and with (C, D) vessel contours used for blood flow quantification. **A** and **C** are magnitude images. **B** and **D** are phase images. Vessels of interest for this case include: internal jugular veins (solid down arrows), external jugular veins (up chevron arrows), common carotid arteries (notched down arrows), and vertebral arteries (up solid arrows). In this case, the right IJV has circulatory flow (blood flowing toward the brain) as shown by the black arrow in the phase image.

The MR flow technique we use gives a pixel by pixel flow for each vessel. From each pixel we get flow as a function of the cardiac cycle. From this data, for all vessels, we can obtain integrated flow over the entire cardiac cycle (ml), volume flow rate (ml/sec) and both positive and negative volume flow rates (ml/sec). The positive volume flow rate in the IJVs was used to establish the criteria for circulatory flow. Circulatory flow represents the situation where there is simultaneously positive and negative flow present within a vein. On the PC phase images, the

vein with circulatory flow shows dark and bright signal areas (Figure 6.1D), and based on the positive volume flow rate plot, the vein has at least 4 time points with positive flow higher than 2ml/sec and positive flow (toward the brain) present for at least half of the cardiac circle. Example plots of the key parameters over a full cardiac cycle are shown in Figure 6.2. Figure 6.2A(3) shows the positive flow plot for an example with circulatory flow. The venous flow was normalized by the total arterial flow (tA), which was defined as the sum of the flow in the common carotid arteries and vertebral arteries. In addition, the ratio between the dominant and sub-dominant IJVs (F_d/F_{sd}) was calculated. Dominant IJV represents the IJV which carries the most outflow, and the sub-dominant IJV is the one with less outflow.

Based on the anatomic information from the 2D TOF and the quantitative IJV flow, the IPD patients and normal controls were separated into 4 categories. Examples from each of these IJV abnormalities are shown in Figure 6.3A-D. In defining the category types from a venous anatomy and flow perspective, flow thresholds and cross section thresholds were defined. An F_d/F_{sd} ratio greater than 4 was taken to be abnormal. We determined the F_d/F_{sd} threshold based on the receiver operator characteristic (ROC) curve analysis of the patients and controls, and 4 represented the optimal cutoff to distinguish between the two populations. The work of Seoane et al[132] suggested a factor of 3:1 for dominant to sub-dominant transverse sinus flow as a risk factor. IJVs are continuation of transverse sinus, so our result is not inconsistent with their findings. The threshold of normalized sub-dominant IJV flow (F_{sd}/tA) was calculated from the normal controls by subtracting the standard deviation from the mean (0.24 – 0.10 = 0.14). An IJV was called stenotic if the cross-sectional area was less than 12.5mm^2 for the upper neck or less than 25mm^2 for the lower neck[13]. Based on these quantitative data and our general observations, we considered the following four categories as representative of the data.

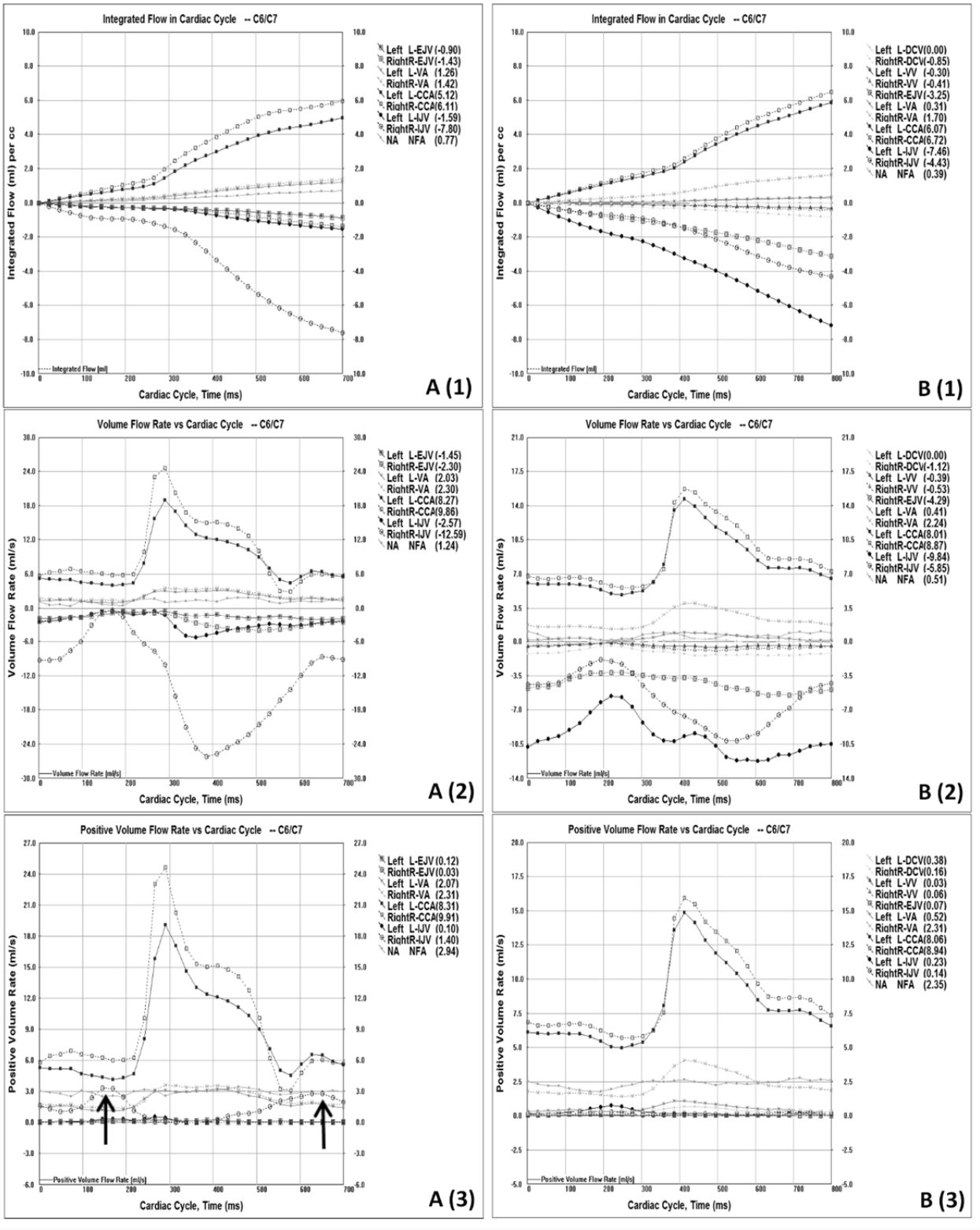

Figure 6.2: **A**: Plots of the integrated flow (A(1)), volume flow rate (A(2)) and positive volume flow rate (A(3)) of the vessels of interest over a full cardiac cycle at C6/C7 for the same case shown in Figure 6.1. **B**: The same types of plots as shown in A but for a case without circulatory

flow. Please note that comparing the positive volume flow rate between Case A and Case B, the positive flow in the right IJV with circulatory flow (arrows in A(3)) is much higher IJV without circulatory flow.

Category 1: All the following conditions must be met: 1) one or both transverse sinuses do not appear on the TOF; 2) one or both sigmoid sinuses are not shown on the TOF; 3) absence or local absence of IJVs on the TOF; 4) F_d/F_{sd} at C6/C7 is greater than 4 and F_{sd}/tA is less than 0.14, or circulatory flow in one or both of the IJVs. In the example case shown in Figure 6.3A(2), there is no left transverse sinus and no left sigmoid sinus on TOF. The upper left IJV is severely stenotic (left arrow) and the top part is absent, and some other small veins reconstitute the left IJV at the lower level. In this case, $F_d/F_{sd} = 13.85$.

Category 2: All the following conditions must be met: 1) one or both transverse sinuses do not appear on the TOF; 2) sigmoid sinuses appear on the TOF; 3) there is banding in the IJVs (this represents very slow blood flow) and/or the presence of stenosis along the IJVs; 4) same as *Category1* criteria(4). In the examples shown in Figure 6.3B(1), the left transverse sinus is missing or invisible although the left sigmoid sinus is present. A banding artifact is evident in almost the entire left IJV, which may be caused by an oscillatory or slow flow. The left sigmoid sinus and the left IJV are much narrower than the right. The presence of a transverse sinus cannot be ruled out without the use of a contrast agent, but there may be reduced flow that makes it difficult to visualize with 2D TOF. Nevertheless, this slow flow may still be manifest in the reduced flow visualized here. In this case, $F_d/F_{sd} = 21.1$.

Category 3: All the following conditions must be met: 1) sigmoid sinuses appear on the TOF; 2) same as *Category1* criteria(4). In the example case shown in Figure 6.3C, part of the left transverse sinus appears to be missing due to slow flow or just in-plane flow, the left sigmoid sinus is visible and $F_d/F_{sd} = 4.39$.

Category 4: All the following conditions must be met: 1) the transverse sinuses and sigmoid sinuses appear on the TOF; 2) the IJVs are not stenotic; and 3) F_d/F_{sd} at C6/C7 is less than 4 and and F_{sd}/tA is bigger than 0.14. The F_d/F_{sd} of the example shown in Figure 6.3D is 2.1.

Except for category 4, all the other 3 categories contain some structural or flow abnormalities. Categories 1, 2 and 3 are ranked based on the severity of the vascular structural abnormalities with the abnormality in Category 1 being the most severe.

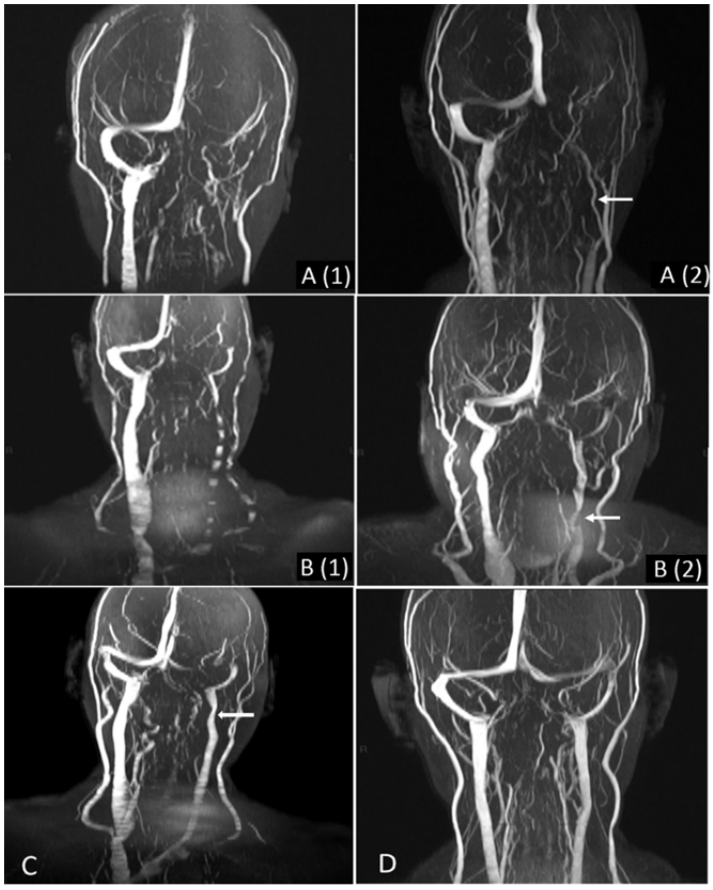

Figure 6.3: A-D: Example cases from each of four categories and different abnormal IJV conditions shown in the coronal projection of the 2D TOF images. **A**: two cases from Category 1, A(2) F_d/F_{sd} = 13.85. **B**: two cases from Category 2, B(1) F_d/F_{sd} = 21.1. **C**: A Category 3 case, F_d/F_{sd} = 4.39. **D**: A Category 4 case, F_d/F_{sd} = 2.1. **A(1)**: missing left IJV. **A(2)**: stenotic left IJV (white arrow in A(2)). **B(1):** banding artifact in the left IJV. The right IJV is big and the signal is uniform, so the banding artifact in the left IJV is caused by abnormal flow, not by swallowing or respiratory artifact. **B(2):** uneven signal contrast in the left IJV. Compared to the right IJV, the signal in the left IJV is not uniform and has a stenosis (white arrow in B(2)).

Statistical analysis

The optimal cut-off values for F_d/F_{sd}, WMH volume and WMH visual score to separate IPD patients and controls were determined using a ROC analysis. An unpaired t-test was used to test the difference between the two populations for age, tA, common carotid arterial flow, vertebral arterial flow, normalized total IJV flow (tIJV/tA), normalized left IJV flow (LIJV/tA), F_d/F_{sd}, normalized collateral venous flow, and WMH visual score. A paired t-test was applied to test the difference between LIJV and RIJV. The categorization distribution difference between IPD patients and the normal controls was analyzed by Chi-squared test. A Wilcoxon Rank-sum test was used to test the WMH volume difference between patients and controls because of outliers.

Results

The age range of the IPD patients was 43 to 74 yr with a mean age of 62.6 yr and standard deviation of 8.3 yr. For the normal subjects, the age range was 56 to 81 yr and the age mean was 64.1 yr with a standard deviation of 6.7 yr. There is no statistical age difference between the two populations (p=0.48).

Category Analysis

The categorization distribution of the IPD patients along with the normal subjects using the criteria defined above is shown in Figure 6.4A. Based on the venous anatomic characteristics and asymmetric flow in the IJVs, there were clearly 4 categories with different severity of venous vasculature. However, with a small number of subjects in some categories, the distribution comparison between the patients and controls may not be applicable. We summed up the subject number in categories 1 to 3 which represent the ones with both anatomic and/or flow abnormalities and then did the comparison. For normal controls, 30% were in categories 1 to 3,

and 70% in category 4; for the PD patients, 57% were in categories 1 to 3 and 43% belonged to category 4. According to the Chi-squared analysis, these two populations are significantly different (χ^2=7.70, $p < 0.01$).

Quantitative Flow Analysis

The tA for the IPD patients and normal subjects were 14.67±2.49 ml/sec and 16.25±2.1 ml/sec, respectively, and there was significant difference between them (p=0.04). The average flow in the common carotid arteries was 5.98±1.26ml/sec in IPD patients and 6.51±1.12ml/sec in controls. The blood flow in the common carotid artery was significantly larger (p=0.04) in the normal people than in the IPD patients. The average flow in the vertebral arteries was 1.39±0.65ml/sec and 1.57±0.76 in the IPD patients and normal subjects, respectively, and there was no significant between them. The tIJV and tIJV/tA for the normal controls was statistically higher than the patients (IPD: 10.85±3.29ml/s, normal controls: 13.54±2.14ml/s, p<0.01; IPD: 0.74±0.17, normal controls: 0.84±0.14, p=0.03).

The normalized flow of the right IJV was found to be significantly larger than the left IJV for both IPD patients (0.56±0.16 vs. 0.18±0.16, p<.0001) and the normal population (0.52±0.2 vs. 0.32±0.19, p=.01). The LIJV/tA was significantly higher in the normal controls (IPD: 0.18±0.16, normal controls: 0.32±0.19, p=0.01). Another measure of flow variation between the left and right IJVs is the ratio of the two IJVs, F_d/F_{sd}. Since F_{sd} can become quite small in some cases, we restricted the ratio to be 10:1 when performing the average values so as not to skew the data (this ratio was set to 10:1 for 8 PD patients and only 1 normal control). This ratio is significantly larger in IPD patients than in normal controls (p =.04). Figure 6.4B shows the scatterplot of dominant vs. sub-dominant IJV flow for the normal controls and IPD subjects.

According to the four vascular categories we defined, Category 1 and Category 2 contain the conditions of: IJV stenosis or missing IJVs, so we refer to patients in Category 1 and 2 as stenotic patients and patients in Category 3 and 4 as non-stenotic patients. According to Figure 6.4B, the stenotic patients showed much higher F_d/F_{sd} than the non-stenotic patients. For the tIJV and tA, there is no significant difference found between the stenotic and non-stenotic patients (tIJV: 10.2±4.4ml/s vs. 11.3±2.4ml/s, p=0.52; tA: 14.7±4.4ml/s vs. 14.6±1.7ml/s, p=0.96).

The category type appears to correlate well with F_d/F_{sd} (Figure 6.4C), which indicates that the higher the F_d/F_{sd} ratio, the more likely the patient sits in the severe abnormal structural and flow categories.

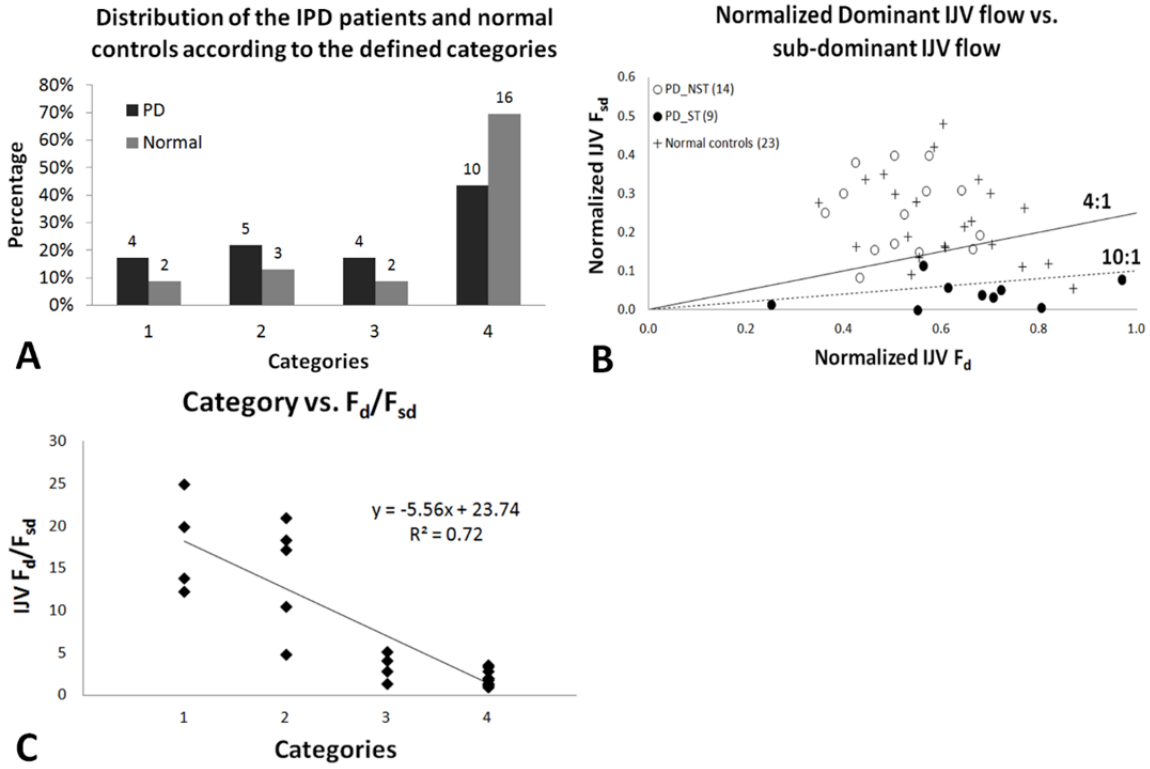

Figure 6.4: A. Distribution of the IPD patients and normal controls according to the defined categories. The normal population lies predominantly in category 4. Most IPD patients are distributed in categories 1to 3 which have venous structural or flow abnormalities.
B. Scatter plot of dominant IJV vs. sub-dominant IJV flow at C6/C7 neck level in IPD patients (circle) and normal controls (cross). The higher black line represents the F_d/F_{sd}=4:1. Comparing to the normal subjects (5 out of 23 cases lie below the 4:1 ratio line), a higher percentage of the

IPD patients (11 out of 23 cases: 48%) showed F_d/F_{sd} greater than 4:1. Moreover, all the patients with stenosis in the IJVs (solid circles) lie below the line indicating that they have more severe asymmetric flow in the IJVs. The lower black line represents F_d/F_{sd}=10:1. In this case, all but only one stenotic PD case falls below the 10:1 line and only one normal falls below this line.
C: Scatterplot of category vs. F_d/F_{sd} for the 23 patients. They have good correlation (R^2=0.72), which indicates that patients with higher F_d/F_{sd} tend to be in the category with more severe venous structural and flow problems.

Correlation between FLAIR WMH and categorization

Of the 23 IPD cases, 21 showed WMH. The mean, median and standard deviation of WMH volume in IPD patients were 5827mm^3, 502mm^3 and 10755mm^3 with a range of 0 mm^3 to 42177mm^3. The mean, median and standard deviation of the WMH volume in the normal controls were 776mm^3, 265mm^3 and 1358mm^3 with range of 0mm^3 to 6147 mm^3. There is a significant difference between the two populations according to the Wilcoxon rank-sum test (p=.04). The IPD patients and normal controls were further divided into a high WMH volume group and a low WMH volume group. The threshold for this separation was set to 500mm^3, which was determined by an ROC analysis between the normal controls and PD patients. The distribution of the patients and normal controls with high and low WMH volume along with the category type is shown in Figure 6.5A.

The WMH visual score for the IPD patients was 5.8 ± 5.3, while the score of the age-matched normal controls was 3.1 ± 3.0. There is significant difference between the two populations for the WMH visual rating (p=0.05). Moreover, all the patients in Category 1 showed a WMH visual score greater than or equal to 4. The distribution of patients with low WMH score (<=3) and high WMH score (>=4) according to their categorization is shown in Figure 6.5B. We chose a score of 3 as the threshold because it could best separate the patients′ categorization distribution.

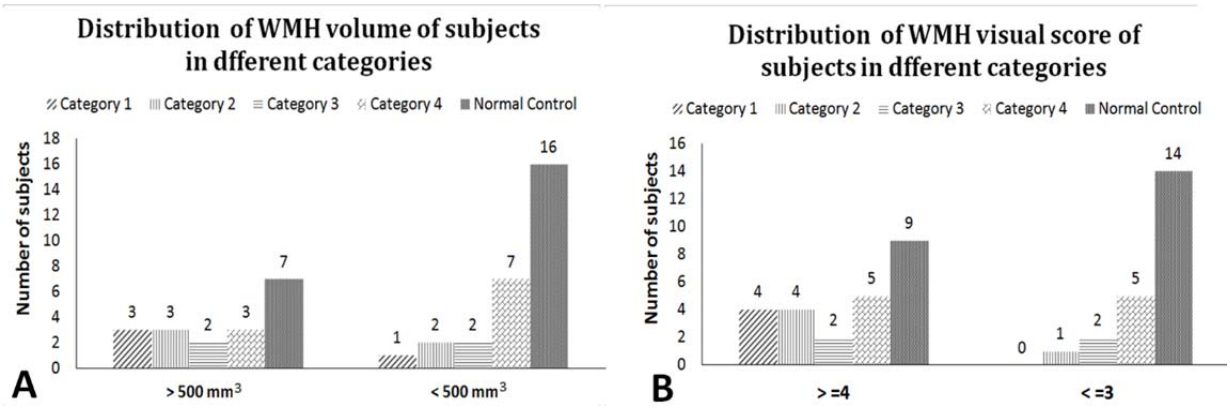

Figure 6.5: A: The distribution of IPD patients and normal controls with low WMH volume (<500mm^3) and high WMH volume (>=500mm^3) for different categories. Majority of Category 4 patients and normal controls contain low WMH volume, while more of the patients in Categories 1 to 3 show high WMH volume. **B:** The distribution of IPD patients and normal controls with low WMH visual score (<=3) and high WMH visual score (>=4) for different categories. All the patients in Category 1 have high WMH visual scores. For patients in Categories 2 and 3, more of the patients show high WMH scores.

Discussion

This paper is the first to study venous abnormalities on patients with IPD. The categorization defined in this work could help distinguish IPD patients from normal controls: 70% of the normal controls appeared in Category 4, while 57% of the IPD patients belonged to Category 1 through 3 (those containing venous structural and/or venous flow abnormalities). In addition, those patients with higher WMH scores tended to be in Category 1 through 3, which indicates a likely correlation between the vascular abnormalities and brain WMH. Moreover, 3 cases with F_d/F_{sd} less than 4 and a WMH score higher than 4 showed circulatory flow in at least one of the IJVs. The combination of structural abnormalities, asymmetric IJV flow, and abnormal hemodynamics such as circulatory flow could together be a major risk factor for developing WMH and perhaps even the disease itself.

Not all PD patients showed these flow abnormalities. However, PD is not a disease but a syndrome and there may be many sources for its development. In this light, one may consider

CCSVI to be just a co-morbidity associated with PD. As for the normal controls, there is definitely an overlap with categories 1 through 3. If one used this to determine who might get PD or neurodegenerative disease, normal controls seen these three categories would be incorrectly assessed. But we have no way of telling today where they will sit 20 or 30 years from now.

Our finding of the asymmetric pattern of the IJV flow is consistent with many other research publications since a majority of individuals are right dominant[133]. However, the flow ratio between the two IJVs (F_d/F_{sd}) of IPD patients is significantly higher than the normal controls. Moreover, patients with vascular stenosis have significantly higher F_d/F_{sd} than the non-stenotic patients.

Recently, more attention has been paid to venous collaterals[134, 135]. By developing a model to calculate the venous collateral flow, which is normalized to the tA, a collateral flow index (CFI) has been compared between normal controls and MS patients with CCSVI. In the supine position, the patient's CFI was reported to be significantly higher than the normal controls (61%, $p<0.0002$)[134]. As our data was also collected in the supine position with quantitative flow in the common carotids, vertebral arteries, IJVs and vertebral veins, a similar type of comparison can be made between the IPD patients and the normal controls. In fact, we too found that the normalized collateral flow in the IPD patients was statistically higher than in the normal controls (0.26 ± 0.17 vs. 0.16 ± 0.14, $p=0.03$). One might well ask, “If the flow in the stenotic IJV and/or transverse sinus can be recovered, could PTA be a potential therapy for some of these patients?”[136, 137]

The observation of the original criteria established by Zamboni et al. [10] are not directly observable by the methods which we have employed. While the original five CCSVI criteria mainly concern flow and stenosis patterns at the lower neck level in the IJV and vertebral veins

as well as the azygous vein, the observations which we have made constitute a new criteria which has only been shown in MRI thus far[133]. Whether or not similar findings could be made on ultrasound is unclear and needs further study, however given that a lack of venous outflow and structural abnormalities have been observed using MRI in the transverse sinus and IJV in our group of PD subjects the authors would expect that a similar observation would be possible with ultrasound.

There are several different MRI visual rating scales for WMHs[131]. We chose Scheltens *et al*. for this study because it is quite commonly used[138]. In addition, according to Pantoni *et al*'s study[139], the four MRI rating scales referenced in their paper are well correlated. Although having WMH is not a standard clinical diagnostic criterion for IPD, in this study cohort, 21 patients showed WMH, 5 had very high WMH volume (more than 10,000mm^3) and of these 4 had a high visual score (greater than 9). A study did by Piccini *et al.*[20] found a positive relationship between the WMH volume and PD symptom severity.

According to many *in vivo* imaging studies, 30% to 55% of PD patients show WMHs[140], and some studies have suggested that WMH are more frequently present in patients with PD than in normal elderly individuals and hypertension patients[20, 141]. Our finding that IPD patients have higher WMH volume and visual score than normal controls is consistent with those studies. WMHs may represent either lacunar infarcts or other tissue damage in the thalamocortial motor system, a key area in the pathogenesis of Parkinsonian symptoms[115]. WMH are thought to relate to cardiovascular disease[22]. Young *et al.*[23] reported the association between WMH and loss of vascular integrity in a neuropathological study, which suggested a vascular origin for these lesions. An MRI-pathological correlation study by Gao et al.[21] demonstrated that focal and periventricular hyperintensities (PVH) often relate to venules and can increase or decrease

over time. They proposed that venous collagenosis dilates the veins, making them macroscopic and causing venous insufficiency with consequent vessel leakage and vasogenic edema[21]. These data support our findings where patients with venous structural and/or venous flow problems are more likely to have more WMHs. Other factors could affect the WMH scores besides venous abnormalities. However, it is believed that WMH especially in aging can be caused by reductions in perfusion to the brain[142].

Limitations and future directions

There are a number of limitations to this study. First, the sample size is small. Nevertheless, even with this small number, we found clear abnormal venous vascular characteristics in IPD patients with significant differences from the normal subjects. This suggests that there is a prevalence of vascular abnormalities in patients with IPD. With a larger number of patients, it would be possible to study the correlation between the vascular problems with IPD sub-types. The second limitation is the lack of 3D time-resolved contrast-enhanced arteriovenography (3D CE MRAV) scans which could offer the advantage of acquiring separate arterial and venous phases and better delineate the dural sinuses. Even though 2D TOF causes reduced signal from in-plane flow, for patients with fast enough flow in the transverse sinuses (such as seen in many cases on the right hand side), we still expect some signal representing the anatomy of the vessels. Third, collecting flow in the transverse sinuses would also be useful to understand the fluid dynamics of the evidently abnormal venous flow on the left side.

Conclusions

In this paper, we have shown several key findings. First, that WMH correlate with venous jugular flow. And second, there are venous vascular abnormalities in patients with IPD that tend

not to be present in the normal population. More specifically, we found that 90% of the patients showed WMHs and that 57% of the patients had structural and/or venous flow abnormalities in the transverse sinus, sigmoid sinus and IJVs. Nevertheless, this is a preliminary work and further studies are required to confirm these conclusions. These findings may prove to be an important imaging means to sub-classify IPD patients, to enhance our understanding of the etiology of IPD and, perhaps, even lead to the development of new treatment regimens.

Acknowledgements

This work was supported, in part, by National Natural Science Foundation of China (grant number: 81171386 and 30770623) and the National Heart, Lung, And Blood Institute of the National Institutes of Health (award number R42HL112580). We would like to thank Jing Jiang, Ying Wang and Wei Feng for their software development supports; Yanwei Miao and Jie Yang for the data analysis discussion; Hong Li, Chenjun Zhu and Xin Sun for helping collect MRI data and data processing.

Chapter Seven Conclusions and future directions

In this thesis, two topics were covered: one was quantifying brain iron and the other one was imaging the vasculature characteristics in Parkinson's patients using MRI. Two major projects were included for the first topic (Chapter 4 and Chapter 5) and one major project (Chapter 6) was done for the second topic. Three approaches were used for measuring iron: $\Delta R2^*$ (Chapter 4), phase (Chapter 4) and magnetic susceptibility (Chapter 5), which were all based on the SWI sequence.

We investigated three MRI parameters' (phase, $\Delta R2^*$ and magnetic susceptibility) trajectories over the lifespan in seven brain gray matter nuclei: caudate nucleus (CN), putamen (PUT), globus pallidus (GP), red nucleus (RN), substantia nigra (SN), pulvinar thalamus (PT) and thalamus (THA). Phase, $\Delta R2^*$ and magnetic susceptibility increased as a function of age in most of those structures, which suggested iron were accumulated in these structures as people getting old since there is direct correlation between these three MRI parameters and iron concentration. All the three parameters showed strong correlations with age in CN, PUT and RN. In GP, SN, PT and THA, the correlations were relatively mild. One exception was the THA. Susceptibility of THA decreased as a function of age. This was consistent with several previous studies [7, 82], however, further studies are needed to warrant the correlation. The phase-age, $\Delta R2^*$-age and the susceptibility-age correlations revealed from the normal subjects in Chapter 4 and Chapter 5 can serve as a basis for determining the normal iron content as a function of age. The findings can help determine abnormal iron content levels in diseases that affect iron content in the brain.

Besides the total ROIs, a more sensitive technique called two-region analysis was used to evaluate iron content change over time in the phase and $\Delta R2^*$ study. The high iron content

region revealed two pieces of new information: both the average iron content per pixel and the area of high iron (RII) increased with age. Furthermore, in the high iron region of PUT, significant increase in iron uptake as a function of age was found for older adults past the age of 40.

QSM is a reliable approach to do iron quantification. It is independent of field strength, echo time, the object's geometry and the relative orientation to the main field. Although different centers may use different approaches to reconstruct susceptibility maps, the results are similar according (Chapter 5). The stability and consistency characteristics of QSM makes it possible to compare the quantification results across different types of magnets and different centers. According to the susceptibility measurements shown in Chapter 5, the highest iron deposition presents in the GP and then followed by the SN, RN, PUT, CN, PT and THA. The correlation between magnetic susceptibility and in vivo iron concentration found in this chapter was 1.03±0.03 ppb/μg Fe/g wet tissue by the age bin method and 1.08±0.06 ppb/μg Fe/g wet tissue by the iron-age function method in PUT. The two slopes were close to each other and also comparable to other studies [67, 108].

Finally, we studied the patterns of chronic venous insufficiency in the dural sinuses and extracranial draining veins and their relationship with white matter hyperintensities for patients with Parkinson's disease. The IPD and normal subjects were classified using both the MR TOF and PC images into four categories: 1) complete or local missing transverse sinus and internal jugular veins (IJVs) on the TOF images; 2) low flow in the transverse sinus and stenotic IJVs; 3) reduced flow in the IJVs; and 4) normal flow and no stenosis. When broken into the above 4 categories with categories 1 through 3 combined, a significant difference in the distribution of the IPD patients and normal controls was observed. In IPD subjects, category type correlated

with both flow abnormalities and WMH. From this preliminary study, we conclude that a major fraction of IPD patients appear to have abnormal venous anatomy and flow on the left side of the brain and neck and that the flow abnormalities appear to correlate with WMH volume.

Future directions:

High iron content region in the normal brain

Measuring iron using magnetic susceptibility is a continuation of using phase since the object susceptibility is the source of phase signal, and it is free from the non-local geometry effect. As a result, with QSM, it becomes possible to quantify iron in the 3D structures. In Chapter 5, we analyzed iron in the whole structures which can serve as a baseline for determining normal iron content as a function of age. However, to better understand the iron deposition pattern and to evaluate iron in a more sensitive manner, we need to apply the two-region analysis technique to the QSM data. This will be the next step of quantifying iron using magnetic susceptibility.

Magnetic susceptibility thresholds for separating the low iron (RI) and high iron (RII) regions will be determined for each structure respectively, and for each structure, the thresholds are calculated separately for each decade. The reason to do this is different structures contain variable levels of iron content and iron deposition is age dependent. For each structure, a uniform area will be selected on multiple slices, and the average susceptibility per pixel and the standard deviation will be recorded. Then, a mean susceptibility value (Mean) will be calculated by averaging the mean susceptibility of all the subjects in that decade. A mean standard deviation (mSD) will be calculated by averaging the standard deviation of all the subjects in that decade. The threshold of a given decade for a given structure is determined by Mean minus two times of

the mSD ($Th = Mean - 2 \times mSD$). The pixels with susceptibility higher than this threshold is defined as RII, which is the high iron content region since high susceptibility correlates with high iron concentration.

The average susceptibility in RII and the normalized volume (normalized to the total volume of the structure) of RII will be plotted as a function of age for each structure of interest. Those plots can serve as a basis of determining abnormal RII iron deposition. The two-region analysis is more sensitive to subtle iron changes comparing to the total ROI analysis which would average out the local high iron deposition. Together with the total ROI baseline reported in Chapter 5, RII iron baselines will provide valuable clinical information for the detection of abnormal brain iron deposition in neurodegenerative diseases such as Parkinson's disease, Alzheimer's disease, multiple sclerosis and so forth.

Dural sinuses abnormalities in PD patents

In Chapter 6, we studied the anatomical abnormalities in the dural sinuses of PD patients. Based on the preliminary TOF data, we found that a fraction of PD patients show absence or partial absence of transverse sinuses. This may be caused by the structural abnormalities or slow flow in the transverse sinuses. Without CE-MRAV and PCFQ at the dural sinuses (including transverse sinuses, sigmoid sinuses, straight sinus, superior sagittal sinus), it's impossible to determine the real causes. As a result, we are planning to preform CE-MRA and PCFQ to 50 IPD patients and 50 age and gender matched normal controls. For the anatomical MRAV analysis, arterial and venous phases of the 3D CE MRAV will be identified. Images will be subtracted to separate veins from arteries in order to identify any possible normal variants along the venous drainage system or the presence of stenosis. The 3D data will be Mipped over many slices to get a better overview of the drainage system. For the dural sinuses flow quantification, through-plane PCFQ

will be performed for the superior sagittal sinus (SSS), the straight sinus and the both left and right transverse sinus and sigmoid sinus. The anatomical features and the quantitative flow will be compared between the IPD patients and the normal controls to verify our preliminary findings in Chapter 6.

APPENDIX A: MODIFIED VISUAL RATING SCALE FOR WMH PROPOSED BY SCHELTENS ET AL *[131, 139]*

WMH in periventricular and deep white matter are scored separately as are the scores for different lobes (the basal ganglia are also included in this assessment). The maximum score for the former is 6 and the latter is 30 as outlined below. Note that the latter has five separate regions, the frontal lobe, parietal lobe, occipital lobe, temporal lobe and basal ganglia.

Periventricular Hyperintensities (Minimum, 0; Maximum 6)

- No caps in the occipital lobe ---- 0
- Caps in the occipital lobe less or equal than 5mm ---- 1
- Caps in the occipital lobe greater or equal than 6mm and less than 10mm ---- 2
- No caps in the frontal lobe ---- 0
- Caps in the frontal lobe less or equal than 5mm ---- 1
- Caps in the frontal lobe greater or equal than 6mm and less than 10mm ---- 2
- No bands at the lateral ventricles ---- 0
- Bands at the lateral ventricles less or equal than 5mm ---- 1
- Bands at the lateral ventricles greater or equal than 6mm and less than 10mm ---- 2

The same criteria is applied for the frontal lobe, parietal lobe, occipital lobe, temporal lobe and basal ganglia

Deep White Matter Hyperintensities (Minimum, 0; Maximum, 30)

- No lesion in the region being studied ---- 0
- Number of the lesions less/equal than 5, size of the lesions less/equal than 3mm ---- 1
- Number of the lesions more/equal than 6, size of the lesions less/equal than 3mm ---- 2

- Number of the lesions less/equal than 5, size of the lesions greater/equal than 4mm and less/equal than 10mm ---- 3
- Number of the lesions more/equal than 6, size of the lesions greater/equal than 4mm and less/equal than 10mm ---- 4
- At least one lesion larger than 11mm ---- 5
- Lesions are confluent ---- 6

REFERENCES

1. Quintana, C., et al., *Study of the localization of iron, ferritin, and hemosiderin in Alzheimer's disease hippocampus by analytical microscopy at the subcellular level.* J Struct Biol, 2006. **153**(1): p. 42-54.
2. Stankiewicz, J., et al., *Iron in chronic brain disorders: imaging and neurotherapeutic implications.* Neurotherapeutics, 2007. **4**(3): p. 371-86.
3. Haacke, E.M., et al., *Iron stores and cerebral veins in MS studied by susceptibility weighted imaging.* Int Angiol, 2010. **29**(2): p. 149-57.
4. Langkammer, C., et al., *MRI for Iron Mapping in Alzheimer's Disease.* Neurodegener Dis, 2013.
5. Wang, Y., et al., *Different iron-deposition patterns of multiple system atrophy with predominant parkinsonism and idiopathetic Parkinson diseases demonstrated by phase-corrected susceptibility-weighted imaging.* AJNR Am J Neuroradiol, 2012. **33**(2): p. 266-73.
6. Haacke, E.M., et al., *Correlation of putative iron content as represented by changes in R2* and phase with age in deep gray matter of healthy adults.* J Magn Reson Imaging, 2010. **32**(3): p. 561-76.
7. Hallgren, B. and P. Sourander, *The effect of age on the non-haemin iron in the human brain.* J Neurochem, 1958. **3**(1): p. 41-51.
8. Haacke, E.M., et al., *Imaging iron stores in the brain using magnetic resonance imaging.* Magn Reson Imaging, 2005. **23**(1): p. 1-25.
9. Haacke, E.M., C.B. Beggs, and C. Habib, *The role of venous abnormalities in neurological disease.* Rev Recent Clin Trials, 2012. **7**(2): p. 100-16.

10. Zamboni, P., et al., *Chronic cerebrospinal venous insufficiency in patients with multiple sclerosis.* J Neurol Neurosurg Psychiatry, 2009. **80**(4): p. 392-9.

11. Haacke, E.M., *Chronic cerebral spinal venous insufficiency in multiple sclerosis.* Expert Rev Neurother, 2011. **11**(1): p. 5-9.

12. Zamboni, P. and R. Galeotti, *The chronic cerebrospinal venous insufficiency syndrome.* Phlebology, 2010. **25**(6): p. 269-79.

13. Haacke, E.M., et al., *Patients with multiple sclerosis with structural venous abnormalities on MR imaging exhibit an abnormal flow distribution of the internal jugular veins.* J Vasc Interv Radiol, 2012. **23**(1): p. 60-8 e1-3.

14. Shulman, J.M. and P.L. De Jager, *Evidence for a common pathway linking neurodegenerative diseases.* Nat Genet, 2009. **41**(12): p. 1261-2.

15. Fernandez-Seara, M.A., et al., *Cortical hypoperfusion in Parkinson's disease assessed using arterial spin labeled perfusion MRI.* Neuroimage, 2012. **59**(3): p. 2743-50.

16. Law, M., et al., *Microvascular abnormality in relapsing-remitting multiple sclerosis: perfusion MR imaging findings in normal-appearing white matter.* Radiology, 2004. **231**(3): p. 645-52.

17. Friedman, A., J. Galazka-Friedman, and E.R. Bauminger, *Iron as a trigger of neurodegeneration in Parkinson's disease.* Handb Clin Neurol, 2007. **83**: p. 493-505.

18. Habib, C.A., et al., *Assessing abnormal iron content in the deep gray matter of patients with multiple sclerosis versus healthy controls.* AJNR Am J Neuroradiol, 2012. **33**(2): p. 252-8.

19. Patel, M., C. Coutinho, and H.C. Emsley, *Prevalence of radiological and clinical cerebrovascular disease in idiopathic Parkinson's disease.* Clin Neurol Neurosurg, 2011. **113**(10): p. 830-4.

20. Piccini, P., et al., *White matter hyperintensities in Parkinson's disease. Clinical correlations.* Arch Neurol, 1995. **52**(2): p. 191-4.

21. Gao, F., et al., *Does variable progression of incidental white matter hyperintensities in Alzheimer's disease relate to venous insufficiency?* Alzheimer's & Dementia, 2008. **4**(4): p. T368-T369.

22. Pantoni, L. and J.H. Garcia, *Pathogenesis of leukoaraiosis: a review.* Stroke, 1997. **28**(3): p. 652-9.

23. Young, V.G., G.M. Halliday, and J.J. Kril, *Neuropathologic correlates of white matter hyperintensities.* Neurology, 2008. **71**(11): p. 804-11.

24. Burton, E.J., et al., *Progression of white matter hyperintensities in Alzheimer disease, dementia with lewy bodies, and Parkinson disease dementia: a comparison with normal aging.* Am J Geriatr Psychiatry, 2006. **14**(10): p. 842-9.

25. Haacke, E. and J. Reichenbach, *Susceptibility Weighted Imaging in MRI: Basic Concepts and Clinical Applications*. 2011: Wiley-Blackwell.

26. Hornak, J.P., *The Basics of MRI*. 1996-2010, Henietta, NY: Interactive Learning Software, Henietta, NY.

27. Haacke, E., et al., *Magnetic Resonance Imaging - Physical Principles and Sequence Design*. 1999: Wiley-Liss.

28. Brown, M.A. and R.C. Semelka, *MRI: Basic Principles and Applications*. 4 ed. 2011: John Wiley & Sons.

29. Liu, S., *Technical Improvements in Quantitative Susceptibility Mapping*, in *School of Biomedical Engineering*. 2014, McMaster University.

30. BUCH, S., *A BRAIN MODEL FOR THE STUDY OF MR SUSCEPTIBILITY INDUCED PHASE BEHAVIOR*, in *Biomedical Engineering* 2013, Master of Applied Science.

31. Haacke, E.M., et al., *Susceptibility-weighted imaging: technical aspects and clinical applications, part 1.* AJNR Am J Neuroradiol, 2009. **30**(1): p. 19-30.

32. Haacke, E.M., et al., *Susceptibility weighted imaging (SWI).* Magn Reson Med, 2004. **52**(3): p. 612-8.

33. Deville, G., M. Bernier, and J.M. Delrieux, *NMR multiple echoes observed in solid 3He.* Physical Review B, 1979. **19**(11): p. 5666-5688.

34. Tang, J., et al., *Improving susceptibility mapping using a threshold-based K-space/image domain iterative reconstruction approach.* Magn Reson Med, 2013. **69**(5): p. 1396-407.

35. Haacke, E.M., et al., *Susceptibility mapping as a means to visualize veins and quantify oxygen saturation.* J Magn Reson Imaging, 2010. **32**(3): p. 663-76.

36. Schweser, F., et al., *Toward online reconstruction of quantitative susceptibility maps: superfast dipole inversion.* Magn Reson Med, 2013. **69**(6): p. 1582-94.

37. Liu, J., et al., *Morphology enabled dipole inversion for quantitative susceptibility mapping using structural consistency between the magnitude image and the susceptibility map.* Neuroimage, 2012. **59**(3): p. 2560-8.

38. Hare, D., et al., *A delicate balance: Iron metabolism and diseases of the brain.* Front Aging Neurosci, 2013. **5**: p. 34.

39. Berg, D. and M.B. Youdim, *Role of iron in neurodegenerative disorders.* Top Magn Reson Imaging, 2006. **17**(1): p. 5-17.

40. Loef, M. and H. Walach, *Copper and iron in Alzheimer's disease: a systematic review and its dietary implications.* Br J Nutr, 2012. **107**(1): p. 7-19.

41. Ayton, S., et al., *Ceruloplasmin dysfunction and therapeutic potential for Parkinson disease.* Ann Neurol, 2013. **73**(4): p. 554-9.

42. Hurtado, E.K., A.H. Claussen, and K.G. Scott, *Early childhood anemia and mild or moderate mental retardation.* Am J Clin Nutr, 1999. **69**(1): p. 115-9.

43. Cortese, S., et al., *Sleep disturbances and serum ferritin levels in children with attention-deficit/hyperactivity disorder.* Eur Child Adolesc Psychiatry, 2009. **18**(7): p. 393-9.

44. Connor, J.R., et al., *Neuropathological examination suggests impaired brain iron acquisition in restless legs syndrome.* Neurology, 2003. **61**(3): p. 304-9.

45. Jeong, S.Y., et al., *Iron insufficiency compromises motor neurons and their mitochondrial function in Irp2-null mice.* PLoS One, 2011. **6**(10): p. e25404.

46. HABIB, C.A., *IMAGING IRON CONTENT IN PATIENTS WITH MULTIPLE SCLEROSIS USING MAGNETIC RESONANCE IMAGING*, in *BIOMEDICAL ENGINEERING*. 2013.

47. Schenck, J.F. and E.A. Zimmerman, *High-field magnetic resonance imaging of brain iron: birth of a biomarker?* NMR Biomed, 2004. **17**(7): p. 433-45.

48. Ke, Y. and Z.M. Qian, *Brain iron metabolism: neurobiology and neurochemistry.* Prog Neurobiol, 2007. **83**(3): p. 149-73.

49. Burdo, J.R., et al., *Mechanisms and regulation of transferrin and iron transport in a model blood-brain barrier system.* Neuroscience, 2003. **121**(4): p. 883-90.

50. Rouault, T.A. and S. Cooperman, *Brain iron metabolism.* Semin Pediatr Neurol, 2006. **13**(3): p. 142-8.

51. Brass, S.D., et al., *Magnetic resonance imaging of iron deposition in neurological disorders.* Top Magn Reson Imaging, 2006. **17**(1): p. 31-40.

52. Wycliffe, N.D., et al., *Reliability in detection of hemorrhage in acute stroke by a new three-dimensional gradient recalled echo susceptibility-weighted imaging technique compared to computed tomography: a retrospective study.* J Magn Reson Imaging, 2004. **20**(3): p. 372-7.

53. Ayaz, M., et al., *Imaging cerebral microbleeds using susceptibility weighted imaging: one step toward detecting vascular dementia.* J Magn Reson Imaging, 2010. **31**(1): p. 142-8.

54. Habib, C.A., et al., *Assessing Abnormal Iron Content in the Deep Gray Matter of Patients with Multiple Sclerosis versus Healthy Controls.* AJNR Am J Neuroradiol, 2011.

55. Langkammer, C., et al., *Quantitative MR imaging of brain iron: a postmortem validation study.* Radiology, 2010. **257**(2): p. 455-62.

56. House, M.J., et al., *Correlation of proton transverse relaxation rates (R2) with iron concentrations in postmortem brain tissue from alzheimer's disease patients.* Magn Reson Med, 2007. **57**(1): p. 172-80.

57. Vymazal, J., et al., *The relation between brain iron and NMR relaxation times: an in vitro study.* Magn Reson Med, 1996. **35**(1): p. 56-61.

58. Mitsumori, F., H. Watanabe, and N. Takaya, *Estimation of brain iron concentration in vivo using a linear relationship between regional iron and apparent transverse relaxation rate of the tissue water at 4.7T.* Magn Reson Med, 2009. **62**(5): p. 1326-30.

59. Dawe, R.J., et al., *Postmortem MRI of human brain hemispheres: T2 relaxation times during formaldehyde fixation.* Magn Reson Med, 2009. **61**(4): p. 810-8.

60. Gelman, N., et al., *MR imaging of human brain at 3.0 T: preliminary report on transverse relaxation rates and relation to estimated iron content.* Radiology, 1999. **210**(3): p. 759-67.

61. Peran, P., et al., *Volume and iron content in basal ganglia and thalamus.* Hum Brain Mapp, 2009. **30**(8): p. 2667-75.

62. Yao, B., et al., *Susceptibility contrast in high field MRI of human brain as a function of tissue iron content.* Neuroimage, 2009. **44**(4): p. 1259-66.

63. Yablonskiy, D.A. and E.M. Haacke, *An MRI method for measuring T2 in the presence of static and RF magnetic field inhomogeneities.* Magn Reson Med, 1997. **37**(6): p. 872-6.

64. An, H. and W. Lin, *Cerebral venous and arterial blood volumes can be estimated separately in humans using magnetic resonance imaging.* Magn Reson Med, 2002. **48**(4): p. 583-8.

65. Ropele, S., et al., *MRI assessment of iron deposition in multiple sclerosis.* J Magn Reson Imaging, 2011. **34**(1): p. 13-21.

66. Xu, X., Q. Wang, and M. Zhang, *Age, gender, and hemispheric differences in iron deposition in the human brain: an in vivo MRI study.* Neuroimage, 2008. **40**(1): p. 35-42.

67. Zheng, W., et al., *Measuring iron in the brain using quantitative susceptibility mapping and X-ray fluorescence imaging.* Neuroimage, 2013. **78**: p. 68-74.

68. Jensen, J.H., et al., *Magnetic field correlation as a measure of iron-generated magnetic field inhomogeneities in the brain.* Magn Reson Med, 2009. **61**(2): p. 481-5.

69. Smith, S.A., J.W. Bulte, and P.C. van Zijl, *Direct saturation MRI: theory and application to imaging brain iron.* Magn Reson Med, 2009. **62**(2): p. 384-93.

70. Connor, J.R., et al., *A quantitative analysis of isoferritins in select regions of aged, parkinsonian, and Alzheimer's diseased brains.* J Neurochem, 1995. **65**(2): p. 717-24.

71. Haacke, E.M., et al., *Characterizing iron deposition in multiple sclerosis lesions using susceptibility weighted imaging.* J Magn Reson Imaging, 2009. **29**(3): p. 537-44.

72. Ke, Y. and Z. Ming Qian, *Iron misregulation in the brain: a primary cause of neurodegenerative disorders.* Lancet Neurol, 2003. **2**(4): p. 246-53.

73. Beard, J.L., J.R. Connor, and B.C. Jones, *Iron in the brain.* Nutr Rev, 1993. **51**(6): p. 157-70.

74. Connor, J.R. and S.L. Menzies, *Cellular management of iron in the brain.* J Neurol Sci, 1995. **134 Suppl**: p. 33-44.

75. Koeppen, A.H., *The history of iron in the brain.* J Neurol Sci, 1995. **134 Suppl**: p. 1-9.

76. Ogg, R.J. and R.G. Steen, *Age-related changes in brain T1 are correlated with iron concentration.* Magn Reson Med, 1998. **40**(5): p. 749-53.

77. Li, W., et al., *Differential developmental trajectories of magnetic susceptibility in human brain gray and white matter over the lifespan.* Hum Brain Mapp, 2013.

78. Morris, C.M., et al., *Histochemical distribution of non-haem iron in the human brain.* Acta Anat (Basel), 1992. **144**(3): p. 235-57.

79. Morris, C.M., J.M. Kerwin, and J.A. Edwardson, *Non-haem iron histochemistry of the normal and Alzheimer's disease hippocampus.* Neurodegeneration, 1994. **3**(4): p. 267-75.

80. Ordidge, R.J., et al., *Assessment of relative brain iron concentrations using T2-weighted and T2*-weighted MRI at 3 Tesla.* Magn Reson Med, 1994. **32**(3): p. 335-41.

81. Pfefferbaum, A., et al., *MRI estimates of brain iron concentration in normal aging: comparison of field-dependent (FDRI) and phase (SWI) methods.* Neuroimage, 2009. **47**(2): p. 493-500.

82. Bilgic, B., et al., *MRI estimates of brain iron concentration in normal aging using quantitative susceptibility mapping.* Neuroimage, 2012. **59**(3): p. 2625-35.

83. Schenker, C., et al., *Age distribution and iron dependency of the T2 relaxation time in the globus pallidus and putamen.* Neuroradiology, 1993. **35**(2): p. 119-24.

84. Siemonsen, S., et al., *Age-dependent normal values of T2* and T2' in brain parenchyma.* AJNR Am J Neuroradiol, 2008. **29**(5): p. 950-5.

85. Reichenbach, J.R., et al., *Small vessels in the human brain: MR venography with deoxyhemoglobin as an intrinsic contrast agent.* Radiology, 1997. **204**(1): p. 272-7.

86. McCrea, R.P., et al., *A comparison of rapid-scanning X-ray fluorescence mapping and magnetic resonance imaging to localize brain iron distribution.* Eur J Radiol, 2008. **68**(3 Suppl): p. S109-13.

87. Harder, S.L., et al., *Mineralization of the deep gray matter with age: a retrospective review with susceptibility-weighted MR imaging.* AJNR Am J Neuroradiol, 2008. **29**(1): p. 176-83.

88. Ogg, R.J., et al., *The correlation between phase shifts in gradient-echo MR images and regional brain iron concentration.* Magn Reson Imaging, 1999. **17**(8): p. 1141-8.

89. Wang, Y., et al., *Artery and vein separation using susceptibility-dependent phase in contrast-enhanced MRA.* J Magn Reson Imaging, 2000. **12**(5): p. 661-70.

90. Haacke, E.M., et al., *Establishing a baseline phase behavior in magnetic resonance imaging to determine normal vs. abnormal iron content in the brain.* J Magn Reson Imaging, 2007. **26**(2): p. 256-64.

91. Vymazal, J., et al., *T1 and T2 of ferritin solutions: effect of loading factor.* Magn Reson Med, 1996. **36**(1): p. 61-5.

92. Aquino, D., et al., *Age-related iron deposition in the basal ganglia: quantitative analysis in healthy subjects.* Radiology, 2009. **252**(1): p. 165-72.

93. Bartzokis, G., et al., *In vivo MR evaluation of age-related increases in brain iron.* AJNR Am J Neuroradiol, 1994. **15**(6): p. 1129-38.

94. Goodman, L., *Alzheimer's disease; a clinico-pathologic analysis of twenty-three cases with a theory on pathogenesis.* J Nerv Ment Dis, 1953. **118**(2): p. 97-130.

95. Wismer, G.L., et al., *Susceptibility induced MR line broadening: applications to brain iron mapping.* J Comput Assist Tomogr, 1988. **12**(2): p. 259-65.

96. Udipi, S., P. Ghugre, and C. Gokhale, *Iron, Oxidative Stress and Health*, in *Oxidative Stress - Molecular Mechanisms and Biological Effects*, V. Lushchak, Editor. 2012, InTech. p. 73-108.

97. Khalil, M., et al., *Determinants of brain iron in multiple sclerosis: a quantitative 3T MRI study.* Neurology, 2011. **77**(18): p. 1691-7.

98. Antharam, V., et al., *High field magnetic resonance microscopy of the human hippocampus in Alzheimer's disease: quantitative imaging and correlation with iron.* Neuroimage, 2012. **59**(2): p. 1249-60.

99. Popescu, B.F., et al., *Mapping metals in Parkinson's and normal brain using rapid-scanning x-ray fluorescence.* Phys Med Biol, 2009. **54**(3): p. 651-63.

100. Rosas, H.D., et al., *Alterations in brain transition metals in Huntington disease: an evolving and intricate story.* Arch Neurol, 2012. **69**(7): p. 887-93.

101. Baraibar, M.A., et al., *Iron-mediated aggregation and a localized structural change characterize ferritin from a mutant light chain polypeptide that causes neurodegeneration.* J Biol Chem, 2008. **283**(46): p. 31679-89.

102. Reichenbach, J.R., et al., *Theory and application of static field inhomogeneity effects in gradient-echo imaging.* J Magn Reson Imaging, 1997. **7**(2): p. 266-79.

103. Langkammer, C., et al., *Susceptibility induced gray-white matter MRI contrast in the human brain.* Neuroimage, 2012. **59**(2): p. 1413-9.

104. Deistung, A., et al., *Toward in vivo histology: a comparison of quantitative susceptibility mapping (QSM) with magnitude-, phase-, and R2*-imaging at ultra-high magnetic field strength.* Neuroimage, 2013. **65**: p. 299-314.

105. Liu, T., et al., *Calculation of susceptibility through multiple orientation sampling (COSMOS): a method for conditioning the inverse problem from measured magnetic field map to susceptibility source image in MRI.* Magn Reson Med, 2009. **61**(1): p. 196-204.

106. Schweser, F., et al., *Quantitative imaging of intrinsic magnetic tissue properties using MRI signal phase: an approach to in vivo brain iron metabolism?* Neuroimage, 2011. **54**(4): p. 2789-807.

107. Wharton, S. and R. Bowtell, *Whole-brain susceptibility mapping at high field: a comparison of multiple- and single-orientation methods.* Neuroimage, 2010. **53**(2): p. 515-25.

108. Langkammer, C., et al., *Quantitative susceptibility mapping (QSM) as a means to measure brain iron? A post mortem validation study.* Neuroimage, 2012. **62**(3): p. 1593-9.

109. Shmueli, K., et al., *Magnetic susceptibility mapping of brain tissue in vivo using MRI phase data.* Magn Reson Med, 2009. **62**(6): p. 1510-22.

110. Smith, S.M., *Fast robust automated brain extraction.* Hum Brain Mapp, 2002. **17**(3): p. 143-55.

111. Abdul-Rahman, H.S., et al., *Fast and robust three-dimensional best path phase unwrapping algorithm.* Appl Opt, 2007. **46**(26): p. 6623-35.

112. Li, W., B. Wu, and C. Liu, *Quantitative susceptibility mapping of human brain reflects spatial variation in tissue composition.* Neuroimage, 2011. **55**(4): p. 1645-56.

113. Lim, I.A., et al., *Human brain atlas for automated region of interest selection in quantitative susceptibility mapping: application to determine iron content in deep gray matter structures.* Neuroimage, 2013. **82**: p. 449-69.

114. Cherubini, A., et al., *Aging of subcortical nuclei: microstructural, mineralization and atrophy modifications measured in vivo using MRI.* Neuroimage, 2009. **48**(1): p. 29-36.

115. Balash, Y. and A.D. Korczyn, *Vascular parkinsonism.* Handb Clin Neurol, 2007. **84**: p. 417-25.

116. Calabresi, P., et al., *New experimental and clinical links between the hippocampus and the dopaminergic system in Parkinson's disease.* Lancet Neurol, 2013. **12**(8): p. 811-21.

117. Poletti, M., M. Emre, and U. Bonuccelli, *Mild cognitive impairment and cognitive reserve in Parkinson's disease.* Parkinsonism Relat Disord, 2011. **17**(8): p. 579-86.

118. Pavese, N., et al., *Fatigue in Parkinson's disease is linked to striatal and limbic serotonergic dysfunction.* Brain, 2010. **133**(11): p. 3434-43.

119. Bohnen, N.I. and R.L. Albin, *White matter lesions in Parkinson disease.* Nat Rev Neurol, 2011. **7**(4): p. 229-36.

120. Thanvi, B., N. Lo, and T. Robinson, *Vascular parkinsonism--an important cause of parkinsonism in older people.* Age Ageing, 2005. **34**(2): p. 114-9.

121. Papapetropoulos, S., et al., *The effect of vascular disease on late onset Parkinson's disease.* Eur J Neurol, 2004. **11**(4): p. 231-5.

122. Zamboni, P., et al., *Hypoperfusion of brain parenchyma is associated with the severity of chronic cerebrospinal venous insufficiency in patients with multiple sclerosis: a cross-sectional preliminary report.* BMC Med, 2011. **9**: p. 22.

123. Utriainen, D., et al., *Magnetic resonance imaging signatures of vascular pathology in multiple sclerosis.* Neurol Res, 2012. **34**(8): p. 780-92.

124. Zamboni, P., et al., *The severity of chronic cerebrospinal venous insufficiency in patients with multiple sclerosis is related to altered cerebrospinal fluid dynamics.* Funct Neurol, 2009. **24**(3): p. 133-8.

125. Beggs, C.B., *Venous hemodynamics in neurological disorders: an analytical review with hydrodynamic analysis.* BMC Med, 2013. **11**: p. 142.

126. Zivadinov, R., et al., *Changes of cine cerebrospinal fluid dynamics in patients with multiple sclerosis treated with percutaneous transluminal angioplasty: a case-control study.* J Vasc Interv Radiol, 2013. **24**(6): p. 829-38.

127. Zamboni, P., et al., *A prospective open-label study of endovascular treatment of chronic cerebrospinal venous insufficiency.* J Vasc Surg, 2009. **50**(6): p. 1348-58 e1-3.

128. Kipshidze, N., et al., *Endovascular treatment of patients with chronic cerebrospinal venous insufficiency and multiple sclerosis.* Georgian Med News, 2011(199): p. 29-34.

129. Kostecki, J., et al., *An endovascular treatment of Chronic Cerebro-Spinal Venous Insufficiency in multiple sclerosis patients - 6 month follow-up results.* Neuro Endocrinol Lett, 2011. **32**(4): p. 557-62.

130. Haacke, E.M., et al., *MR Angiography and Flow Quantification*, in *Magnetic resonance Imaging-physical Principles and Sequence Design*, E.M. Haacke, et al., Editors. 1999, Wiley-Liss.

131. Scheltens, P., et al., *A semiquantative rating scale for the assessment of signal hyperintensities on magnetic resonance imaging.* J Neurol Sci, 1993. **114**(1): p. 7-12.

132. Seoane, E. and A.L. Rhoton, Jr., *Compression of the internal jugular vein by the transverse process of the atlas as the cause of cerebellar hemorrhage after supratentorial craniotomy.* Surg Neurol, 1999. **51**(5): p. 500-5.

133. Feng, W., et al., *Quantitative flow measurements in the internal jugular veins of multiple sclerosis patients using magnetic resonance imaging.* Rev Recent Clin Trials, 2012. **7**(2): p. 117-26.

134. Zamboni, P., et al., *An ultrasound model to calculate the brain blood outflow through collateral vessels: a pilot study.* BMC Neurol, 2013. **13**: p. 81.

135. Zamboni, P., et al., *Venous collateral circulation of the extracranial cerebrospinal outflow routes.* Curr Neurovasc Res, 2009. **6**(3): p. 204-12.

136. Huang, P., et al., *Successful treatment of cerebral venous thrombosis associated with bilateral internal jugular vein stenosis using direct thrombolysis and stenting: a case report.* Kaohsiung J Med Sci, 2005. **21**(11): p. 527-31.

137. Formaglio, M., et al., *Stenting of a cerebral venous thrombosis.* J Neuroradiol, 2010. **37**(3): p. 182-4.

138. Beyer, M.K., et al., *Visual rating of white matter hyperintensities in Parkinson's disease.* Mov Disord, 2006. **21**(2): p. 223-9.

139. Pantoni, L., et al., *Visual rating scales for age-related white matter changes (leukoaraiosis): can the heterogeneity be reduced?* Stroke, 2002. **33**(12): p. 2827-33.

140. Lee, S.J., et al., *The severity of leukoaraiosis correlates with the clinical phenotype of Parkinson's disease.* Arch Gerontol Geriatr, 2009. **49**(2): p. 255-9.

141. Stern, M.B., et al., *Magnetic resonance imaging in Parkinson's disease and parkinsonian syndromes.* Neurology, 1989. **39**(11): p. 1524-6.

142. Alosco, M.L., et al., *Cerebral perfusion is associated with white matter hyperintensities in older adults with heart failure.* Congest Heart Fail, 2013. **19**(4): p. E29-34.

ABSTRACT

MEASURING BRAIN IRON IN HEALTHY CONTROLS AND ASSESSING VENOUS ABNORMALITIES IN PARKINSON'S DISEASE USING MRI

by

MANJU LIU

August 2014

Advisor: Dr. E. Mark Haacke

Major: Biomedical Engineering

Degree: Doctor of Philosophy

Iron plays a key role in a number of brain cellular processes. However, abnormal brain iron regulation correlates with a number of neurodegenerative diseases such as Parkinson's disease, multiple sclerosis and so forth. To further elucidate the involvement of iron in neurodegenerative disorders, a robust in vivo quantitative non-invasive assessment of normal brain iron deposition over time is essential. A variety of magnetic resonance imaging (MRI) methods have been used to quantify iron both in vivo and in vitro non-invasively. We first created the baseline of phase value and $\Delta R2^*$ as a function of age in seven gray matter nuclei. We also studied how the high iron region in the structures change over time, which is a more sensitive way to study the brain iron deposition. Quantitative susceptibility mapping (QSM) is another approch we used to study normal brain iron deposition as a further step since susceptibility is a tissue property that is free from geometry effect and imaging parameters. Except in the thalamus, iron increases over time in the gray matter nuclei. We found iron content decreases as a function of age in thalamus according to the susceptibility measurements. These measured susceptibility values are also

compared with the regional iron concentrations taken from the histochemical post mortem study published by Hallgren and Sourander to establish an in vivo quantitative conversion factor between magnetic susceptibility and iron concentration. The correlation between the magnetic susceptibility and iron concentration found in this thesis is 1.03±0.03 ppb per μg iron/g wet tissue.

Idiopathic Parkinson's disease (IPD) remains one of those neurodegenerative diseases where the cause remains unknown. Many clinically diagnosed cases of IPD are associated with cerebrovascular disease and white matter hyperintensities (WMH). In this thesis, we also include a study to investigate the presence of transverse sinus and extracranial venous abnormalities in IPD patients and their relationship with brain WMH. As a result of this preliminary study, we conclude that a major fraction of IPD patients appear to have abnormal venous anatomy and flow on the left side of the brain and neck and that the flow abnormalities appear to correlate with WMH volume.

AUTOBIOGRAPHICAL STATEMENT

Manju Liu 2568 Locksley Ct., Troy, MI 48083 ea4411@wayne.edu 313.506.1861

Education

WAYNE STATE UNIVERSITY **Detroit, MI**
College of Engineering **GPA 3.80/4.0**
PhD of Science in Biomedical Engineering (Magnetic Resonance Imaging) 2010 – Present

WAYNE STATE UNIVERSITY **Detroit, MI**
College of Engineering **GPA 3.82/4.0**
Master of Science in Biomedical Engineering (Medical Imaging) December 2010

GUANGXI UNIVERSITY **Nanning, China**
School of Physics Sciences and Technology **GPA: 3.4/4.0**
Bachelor of Engineering in Electronic Science and Technology June 2007

Publications (2009-Present) **Detroit, MI**

Journal Articles and book section

- **Liu M**, Xu H, Wang Y, Zhong Y, Xia S, Utriainen D, et al. Patterns of Chronic Venous Insufficiency in major cerebral veins of patients with Parkinson's disease. Journal of Vascular Surgery. 2013. Tentatively Accepted.
- **Liu M**, Habib C, Liu S, Dicicco D, Miao Y, Haacke EM. Establishing a reference of magnetic susceptibility in healthy human brain gray nuclei as a function of age. 2013. Paper in Progress.
- Wang Y, Butros SR, Shuai X, Dai Y, Chen C, **Liu M**, et al. Different iron-deposition patterns of multiple system atrophy with predominant parkinsonism and idiopathetic Parkinson diseases demonstrated by phase-corrected susceptibility-weighted imaging. AJNR Am J Neuroradiol. 2012;33(2):266-73.
- Habib CA, **Liu M**, Bawany N, Garbern J, Krumbein I, Mentzel HJ, et al. Assessing abnormal iron content in the deep gray matter of patients with multiple sclerosis versus healthy controls. AJNR Am J Neuroradiol. 2012;33(2):252-8.
- Wen N, Glide-Hurst C, Nurushev T, Xing L, Kim J, Zhong H, Liu D, **Liu M**, Burmeister J, Movsas B, Chetty I. Evaluation of the deformation and corresponding dosimetric implacations in prostate cancer treatment. 2012;(57):5462-79.
- **Liu M**, Habib C, Miao Y, Haacke EM. Measuring Iron Content with Phase. In: Haacke EM, Reichenbach JR, editors. Susceptibility Weighted Imaging in MRI: Basic Concepts and Clinical Applications: Wiley-Blackwell; 2011. p. 369-401.
- Haacke EM, Miao Y**, Liu M**, Habib CA, Katkuri Y, Liu T, et al. Correlation of putative iron content as represented by changes in R2* and phase with age in deep gray matter of healthy adults. J Magn Reson Imaging. 2010;32(3):561-76.
- Haacke EM, Garbern J, Miao Y, Habib C, **Liu M**. Iron stores and cerebral veins in MS studied by susceptibility weighted imaging. Int Angiol. 2010;29(2):149-57.